Dissociation of ^{8}He

Yoshiyuki Iwata

A DISSERTATION

Submitted to
Rikkyo University
in partial fulfillment of the requirements
for the Degree of

Doctor of Philosophy

Department of Physics

1999

Abstract

Kinematically complete measurements of Coulomb dissociation of 24 MeV/A ^{8}He into ^{6}He and two neutrons have been performed. Momenta of incident beam particles and outgoing decay products from the ^{8}He dissociation were measured in coincidence.

The two neutron removal cross sections were extracted from inclusive (^{6}He+n+X) and exclusive (^{6}He+2n) data sets. The cross sections from the two data sets differ by a factor of two. This discrepancy can be understood with an assumption of the sequential decay mechanism via the ^{7}He resonance.

Evidence of the mechanism is found in relative energy distributions between ^{6}He and neutron E_{6-n}. A prominent peak observed at $E_{6-n} \sim 0.4$ MeV is well reproduced with a Monte Carlo simulation assuming the sequential decay mechanism. Furthermore, the neutron momentum distributions were reproduced well with those calculated with the simulation and the cluster orbital shell model approximation (COSMA) wave function assuming the sequential decay mechanism.

The momentum distributions of ^{6}He and neutrons in the ^{8}He rest frame were reconstructed. The distributions were fitted with gaussian functions, and the obtained width parameters of the function were compared with those of recent measurements.

With the kinematically complete measurements, the excitation energy distribution of ^{8}He can be reconstructed. The measured excitation energy distributions for lighter targets show a prominent peak which is consistent with the known excited state of ^{8}He (E_x=3.57 MeV, Γ=0.50 MeV and $J^\pi=2^+$). The distribution for Pb target were found to have broad structure, indicating the $E1$ continuum state, as observed in measurements of other halo nuclei. With the measured excitation energy distribution, the photonuclear cross section σ_{E1} and the dipole strength function $dB(E1)/dE_d$ were deduced for the first time.

Contents

List of Figures

List of Tables

Chapter 1

Introduction

Recent development of the radioactive nuclear beam (RNB), produced through high energy fragmentation reactions of heavy ions, has led us to explore structures and reactions of nuclei far from stability. In studies of nuclear structure using the RNB, intriguing features were first found in measurements of interaction cross sections of light neutron-rich nuclei at the Bevalac in the Lawrence Berkley Laboratory (LBL)[1]. Secondary beams of light neutron-rich nuclei with energies of 800 MeV/A were produced, and the interaction cross sections for those nuclei with Be, C and Al targets were measured. With the measured cross sections, root mean square radii were deduced and found to be remarkably larger, particular for the ^{11}Li nucleus, than in neighbouring nuclei. These data provide important information on nuclear sizes and present questions about the existence of a so-called neutron halo or neutron skin[2].

Furthermore, evidence of the neutron halo structure has been found in measurements of momentum distributions from projectile fragmentation reactions of the halo nuclei at 800 MeV/A[3]. The measured transverse momentum distributions of ^{9}Li from projectile fragmentations of ^{11}Li showed a much narrower width than that expected from the Goldhaber model, which considers the Fermi motion of nucleons[4]. The narrow width was interpreted as a large spatial extent of two valence neutrons surrounding a ^{9}Li core. Such a halo property of the ^{11}Li has been also confirmed in subsequent measurements of a quadrupole moment relative to that of ^{9}Li $|Q(^{11}\text{Li})/Q(^{9}\text{Li})|$ [5], of neutron angular distributions from fragmentation reactions[6] and of β-delayed particle emissions[7]. To clarify the detailed

11

8C	9C	10C	11C	12C	13C	14C	15C	16C	17C	18C	19C
7B	8B	9B	10B	11B	12B	13B	14B	15B	16B	17B	
6Be	7Be	8Be	9Be	10Be	11Be	12Be	13Be	14Be			
4Li	5Li	6Li	7Li	8Li	9Li	10Li	11Li				
3He	4He	5He	6He	7He	8He	9He					
1H	2H	3H	4H								
n											

particle stable

one−neutron halo

multi−neutron halo

Figure 1.1: Overview of ascertained neutron-rich halo nuclei.

structure of ^{11}Li, several exclusive measurements have been performed[8, 9, 10].

The halo structure has also been ascertained for ^{6}He, ^{8}He[2, 11] and other heavier isotopes (see Fig. 1.1). Since the structure of ^{6}He, described as a ^{4}He core and two neutrons, is relatively simple, intensive studies have been made both experimentally and theoretically. On the other hand, only little attention has been paid to ^{8}He because the structure is considered to be more complicated. Owing to the weak binding of the ^{6}He nucleus, ^{8}He cannot be regarded as having the ^{6}He core surrounded by two valence neutrons. On the other hand, the ^{4}He nucleus still exists as a core without large modification of its wave function. Therefore, ^{8}He rather has a structure of ^{4}He+4n. A large two-neutron separation energy of ^{8}He (S_{-2n}=2.14 MeV) as compared to that of ^{6}He (S_{-2n}=0.975 MeV), owing to a completely filled $1p_{3/2}$ shell with the four valence neutrons, is also suggestive of this structure.

Evidence of the ^{4}He+4n structure was also found from the measurements of interaction cross sections[2, 12]. According to the Glauber model, the two-neutron removal cross section σ_{-2n} and the interaction cross section σ_I would satisfy a relation

$$\sigma_{-2n}(^8\text{He}) = \sigma_I(^8\text{He}) - \sigma_I(^6\text{He}) \tag{1.1}$$

for 2n-halo nuclei. However, the experimental cross sections do not satisfy this relation, but instead satisfy a relation

$$\sigma_{-2n}(^8\text{He}) + \sigma_{-4n}(^8\text{He}) = \sigma_I(^8\text{He}) - \sigma_I(^4\text{He}) \tag{1.2}$$

indicating 4n-halo structure.

The ^{8}He nucleus is intriguing, because its neutron-to-proton ratio is the largest among known bound nuclei. The ground state ($J^\pi=0^+$) has a dominant configuration of the ^{4}He core ($J^\pi=0^+$) and four valence neutrons in the $1p_{3/2}$ shell. Recently, several experiments have been performed to search for excited states of ^{8}He. In measurements of ^{8}He+p elastic and inelastic scattering, a first excited state was observed at E_x=3.57±0.12 MeV with Γ=0.50±0.35 MeV[13]. With measured angular distributions, spin-parity of the state is assigned as $J^\pi=2^+$, which is in good agreement with shell-model calculations[14, 15, 16]. A measurement made by proton pick-up reactions yielded E_x=3.59 MeV with Γ=0.80 MeV[17]. The configuration of the first excited state is understood to be $(1p_{3/2})^{-1} (1p_{1/2})^1$, just as for the 2^+ state in ^{12}C. In addition to this state, three additional excited states have been reported in measurements of two-proton pick-up.[18]. The measured excited states are presented in Fig. 1.2.

An interesting property of some halo nuclei is the existence of a low-lying, unbound excitation. While most of the dipole strength for stable nuclei is known to be exhausted by a giant dipole resonance (GDR) with excitation energies $E_x \sim 78A^{-1/3}$, an enhancement of the dipole strength at $E_x \sim 1$ MeV was first observed in ^{11}Li[8, 9, 10]. In addition, the low-lying excitation is observed in the halo nuclei ^{11}Be[19] and ^{6}He[20]. To explain such an excitation, a new collective mode, a so-called a soft dipole resonance (SDR), was proposed[23]. The model assumes that the low-lying excitation is an oscillation of the

7.14(4) ‾ ‾ ‾ ‾ ‾ ‾ ‾ ‾ ‾

6.03(10) ‾ ‾ ‾ ‾ ‾ ‾ ‾ ‾

4.54(15) ‾ ‾ ‾ ‾ ‾ ‾ ‾ ‾

3.57   (2+)

2.14 ▬▬▬▬▬▬

^{6}He+2n

0   0+

^{8}He
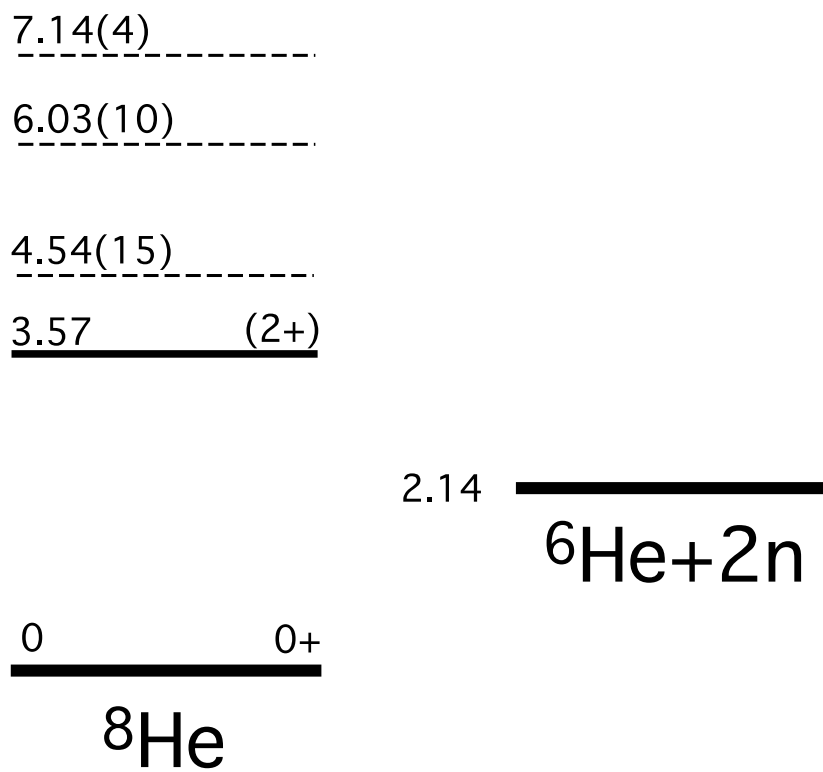
Figure 1.2: A level scheme of ^{8}He. Level energies of ^{8}He excited states are taken from references(see text).

core nucleus against the halo neutrons. Thus, the excitation energy of the SDR, for which the restoring force on the core comes only from the halo neutrons, is lower than that of the GDR. However, the existence of the SDR has not been confirmed so far.

Measurements of the low-lying excitation are important to clarify the collective structure in halo nuclei. However, no experimental study has yet been dedicated to the ^{8}He nucleus. Recently, measurements of breakup reactions of ^{8}He at 240 MeV/A on C and Pb targets have been performed[21, 22]. Momentum distributions of ^{6}He and neutrons revealed that a dominant reaction mechanism is a sequential decay via a ^{7}He resonance. Although the excitation energy distribution of ^{8}He was reconstructed, no crucial information on the low-lying excitation was presented.

In order to clarify the interpretation of the low-lying excitation and the reaction mechanism of ^{8}He, a kinematically complete measurement of Coulomb dissociation of 24 MeV/A ^{8}He on a Pb target was performed. In addition, measurements on Sn and Al targets were performed to evaluate contributions of nuclear dissociation. Momenta of outgoing decay products, ^{6}He and two neutrons, from the dissociation of ^{8}He on the targets were measured in coincidence. The kinematically complete measurements allowed us to reconstruct an excitation energy distribution of ^{8}He and momentum distributions of ^{6}He and neutrons in the ^{8}He rest frame. With the measured excitation energy distributions, a photonuclear cross section and a dipole strength function were deduced for the first time.

Recently, the Coulomb dissociation reaction has been widely used as a probe in studies of the nuclear structure since the electromagnetic interaction is well known as compared to the strong interaction. In measurements of the Coulomb dissociation reaction, a projectile is excited by the Coulomb field of a high-Z target nucleus. If the excitation energy is above a particle emission threshold, the excited projectile may break up by emission of that particle. By measuring the Coulomb dissociation cross section, the photonuclear cross section and the dipole strength function can be determined as follows.

The double differential cross section $d^2\sigma_c/dE_\gamma d\Omega$ for an electromagnetic excitation

with electric multipole order λ is expressed in a first order perturbation theory as[24]

$$\frac{d^2\sigma_c}{dE_\gamma d\Omega} = \left(\frac{Z_T e}{\hbar v}\right)^2 a^{-2\lambda+2} \frac{df_{E\lambda}(\theta,\xi)}{d\Omega} B(E\lambda, I_i \to I_f)\rho_f(E_\gamma) \qquad (1.3)$$

where v is the relative velocity, $Z_T e$ is the target charge, a is half the distance of closest approach in a head-on collision, ρ_f is the density of final states and $\xi = E_\gamma a/\hbar v$. The reduced transition probability $B(E\lambda)$ is related to the photoabsorption cross section $\sigma_{E\lambda}^{photo}$ by

$$\sigma_{E\lambda}^{photo} = \frac{(2\pi)^3(\lambda+1)}{\lambda[(2\lambda+1)!!]^2}(k_\gamma)^{2\lambda-1} B(E\lambda, I_i \to I_f)\rho_f(E_\gamma) \qquad (1.4)$$

where $k_\gamma = E_\gamma/\hbar c$. With the above two relations, the Coulomb excitation cross section can be rewritten as

$$\frac{d^2\sigma_c}{dE_\gamma d\Omega} = \frac{1}{E_\gamma}\frac{dn_{E\lambda}}{d\Omega}\sigma_{E\lambda}^{photo} \qquad (1.5)$$

where

$$\frac{dn_{E\lambda}}{d\Omega} = Z_T^2\alpha\frac{\lambda[(2\lambda+1)!!]^2}{(2\pi)^3(\lambda+1)}\xi^{-2\lambda+2}\left(\frac{c}{v}\right)^{2\lambda}\frac{df_{E\lambda}(\theta,\xi)}{d\Omega} \qquad (1.6)$$

with the fine structure constant $\alpha = e^2/\hbar c$. The function $dn_{E\lambda}/d\Omega$ represents the virtual photon number per unit solid angle. Note that the function only depends on the projectile energy and the excitation energy and does not depend on the internal structure of the projectile.

Chapter 2

Experiment

The experimental aim is to determine the excitation energy of the ^{6}He+2n system in the Coulomb dissociation of ^{8}He. The determination requires kinematically complete measurements of outgoing decay products from the dissociation of the photoexcited ^{8}He. In this chapter, descriptions of the experimental setup are provided.

The experiment was performed at the National Superconducting Cyclotron Laboratory (NSCL) in the Michigan State University. A schematic drawing of the experimental setup is shown in Fig. 2.1. To measure all momenta of the outgoing decay products, the detector system is composed of fragment detectors for the detection of ^{6}He and the *Neutron Wall Array* for the detection of neutrons. Details of the each detector are described in following sections.

2.1 ^{8}He beam

The ^{8}He beam was produced by utilizing projectile fragmentation reactions. A 1.9 g/cm^2 ^{9}Be target was bombarded with an 80 MeV/A ^{18}O^{6+} primary beam produced by the K1200 superconducting cyclotron at the NSCL. Then, a secondary beam of ^{8}He was analyzed and separated by two dipole and several quadrupole magnets of the A1200 Fragment Separator[25] and degraded to 25 MeV/A before reaching the experimental area. Momentum slits of the Fragment Separator were set to $(\Delta p/p) = 1$ %, so that the energy spread of the ^{8}He beam was ± 0.5 MeV/A. A summary of the beam energies is
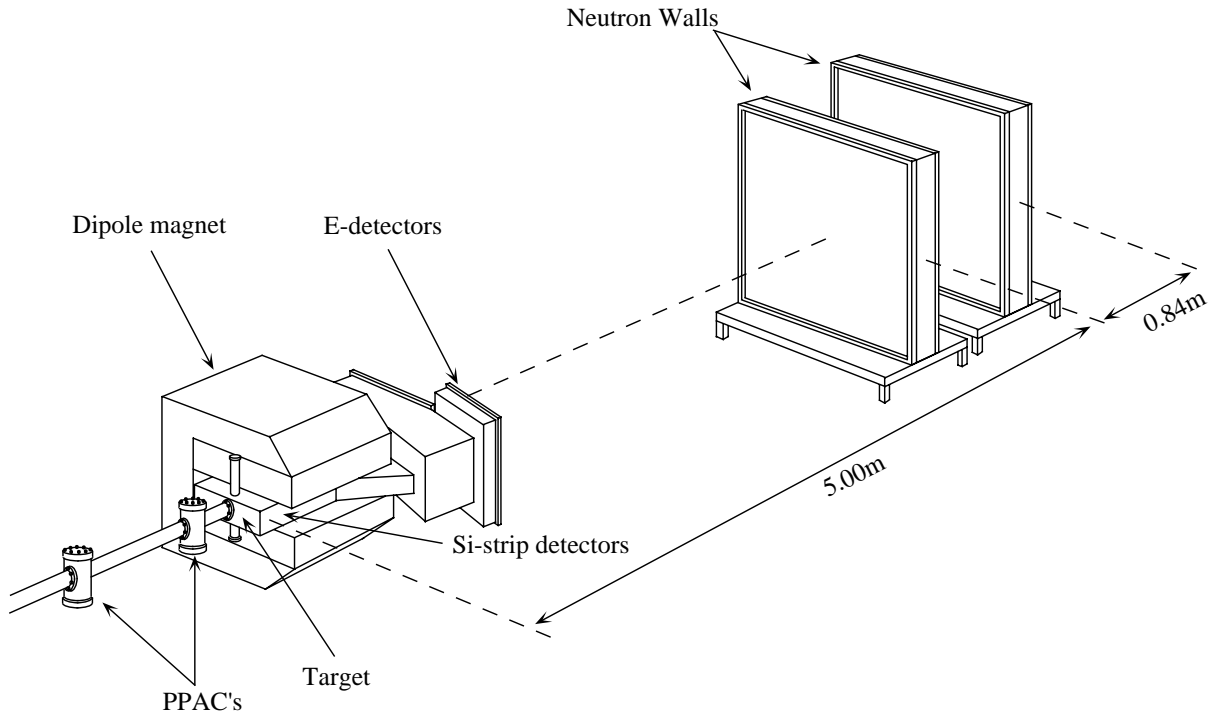
Figure 2.1: A schematic drawing of the detector setup. The fragment detectors consisting of Si-strip ΔE detectors and plastic E-detectors are installed in a vacuum chamber. The *Neutron Wall Array* are centered on zero degrees from the beam axis.

listed in Table 2.1.

An average intensity of the ^{8}He beam was a few $\times$ 10^2 particle/sec corresponding to 15 % of the total number of beam particles. A major impurity of the beam was 85 % 44 MeV/A ^{12}Be, whose events were distinguishable from the ^{8}He beam with the fragment detectors.

Since the size of the beam spot was rather large, about 2.5 cm (horizontal) $\times$ 1.2 cm (vertical) in full width at half maximum (FWHM), the incident angle and the target position had to be measured to determine the emission angle of the outgoing ^{6}He from the

Beam kind	Bρ (Tm)	Incident (MeV/A)	Center of the Pb target (MeV/A)
^{8}He	2.8930	24.902	23.979
(^{12}Be)	2.8930	43.831	42.162

Table 2.1: Rigidities and energies of beam particles used in the experiment.

dissociation of ^{8}He precisely. Hence, the incident angle of each beam particle was measured with two position-sensitive parallel plate avalanche counters (PPAC's)[26]. A schematic drawing of the counter layout is shown in Fig. 2.2. The two PPAC's were located upstream of the target and separated by 91.4 cm. The angle and the position of the incident beam particles at the target were calculated from two-dimensional position information of the counters over its sensitive area 5×10 cm^2. With the position information of the two PPAC's, a two-dimensional spectrum for a beam profile on the target could be calculated. An example of beam profile spectra for the ^{8}He beam at the target is shown in Fig. 2.3.

The PPAC's were filled with iso-octane gas at a pressure of 5 Torr, and a negative bias of approximately 720 V was applied to a central electrode foil. A signal created by passage of an ion was resistively divided into four signals at up, down, left and right electrodes. With the four signals, two-dimensional position of the incident ions was obtained. The efficiency of the PPAC's for ^{8}He was found to be better than 98.4 %.

Si-strip detectors

Target

15.2 cm

PPAC's

38.6 cm

91.4 cm
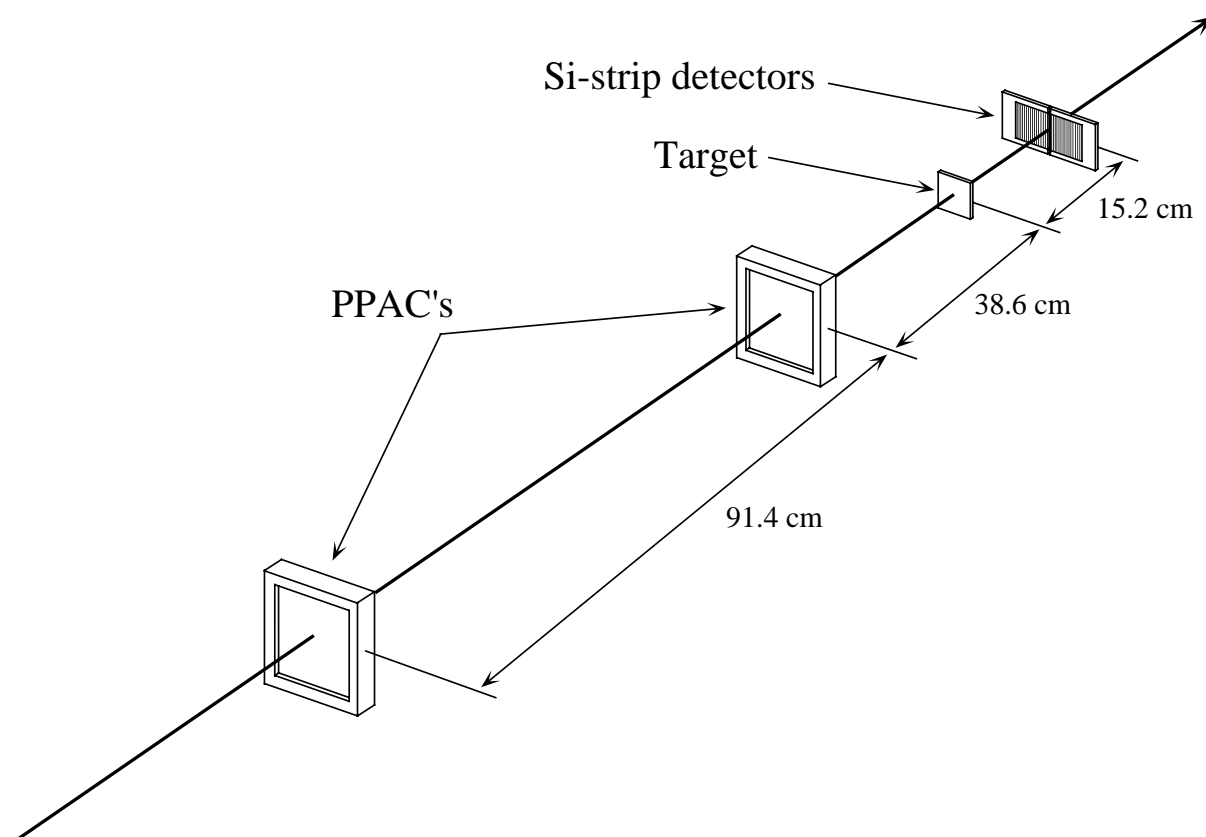
Figure 2.2: A layout of beam detectors consisting of two position-sensitive parallel plate avalanche counters (PPAC's), a target, and two Si-strip detectors. An angle and a target position of incident ions are determined by position information of the two PPAC's.
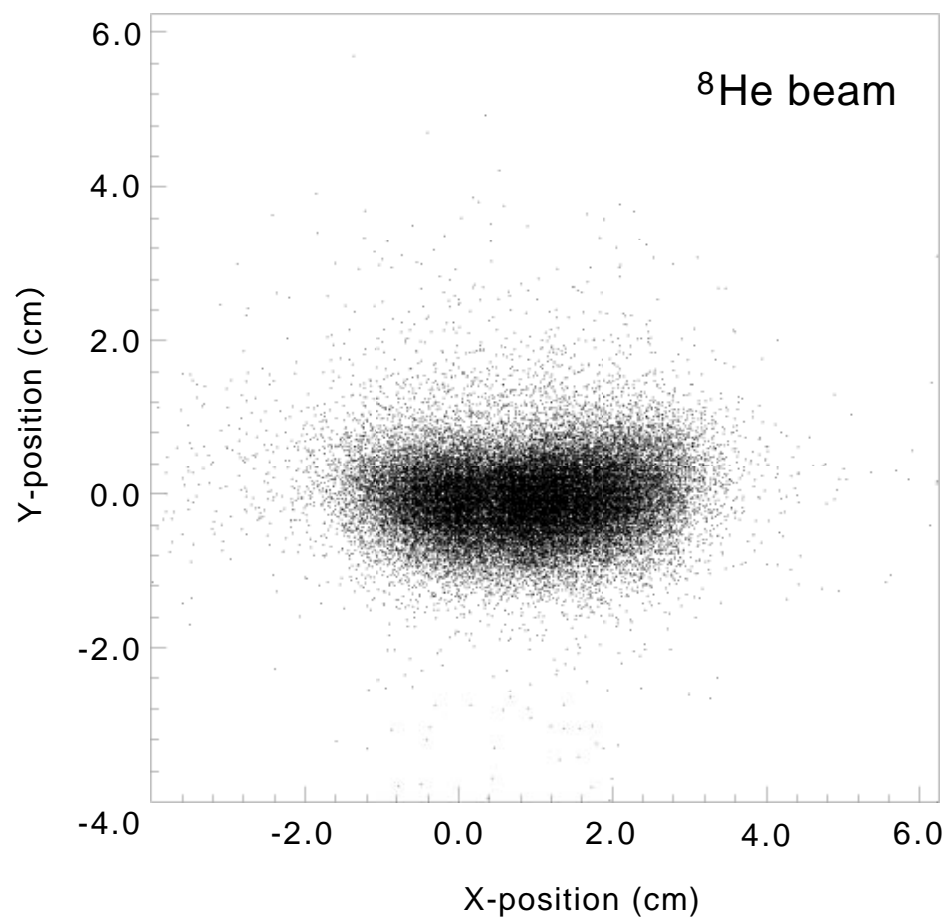
Figure 2.3: A ^{8}He beam profile at the target position. The incident positions of ^{8}He ions are calculated with two-dimensional position information of the two PPAC's. The size of the beam spot is about 2.5 cm (horizontal) × 1.2 cm (vertical) in FWHM.

2.2 Targets

The experimental task was to measure the Coulomb dissociation reaction cross sections induced by absorption of photons from the Coulomb field of a high-Z target nucleus. However, the dissociation reaction consists of two components, Coulomb dissociation and nuclear dissociation. Hence, it was necessary to evaluate a contribution of the nuclear dissociation reactions. To evaluate each contribution, three different targets were used. In addition, measurements without a target (target-out runs) were also performed to subtract background events which are mainly caused by reactions in the fragment detectors. For the target-out runs, the energy of the ^{8}He beam was degraded to 23.1 MeV/A, so that the energy of the beam particles was the same at the entrance of the Si-strip detectors between the target-in and the target-out runs. A list of the targets is summarized in Table 2.2.

The choice of thickness was determined by constraint of two effects, reaction rate and energy resolution. The former favors a thick target. On the other hand, an increase of energy loss in the target and a sizable multiple Coulomb scattering would cause ambiguities in an energy determination of the decay products. As a compromise, a thickness of about a 400 mg/cm^2 for the Pb target was chosen. For the other targets, the thickness was selected so that the energy loss in them was almost the same as that in the Pb target.

Target	thickness	Energy loss (Total)
^{208}Pb	397 mg/cm^2	1.87 MeV/A (15.0 MeV)
^{120}Sn	364 mg/cm^2	2.13 MeV/A (17.0 MeV)
^{27}Al	247 mg/cm^2	2.11 MeV/A (16.9 MeV)

Table 2.2: Summary of targets used in the experiment. Energy losses are calculated for ^{8}He ions.

2.3 Fragment detectors

The fragment detectors were designed to measure charged fragments and were composed of Si-strip ΔE detectors and plastic E-detectors. The detectors were installed in a vacuum chamber whose pressure was kept at a few $\times$ 10^{-5} Torr. Downstream from the Si-strip detectors, a dipole magnet was placed to deflect charged fragments. A schematic drawing of the detector layout is provided in Fig. 2.4. Detailed descriptions of the Si-strip detectors, the E-detectors and the dipole magnet are found in sections 2.3.1, 2.3.2 and 2.3.3, respectively.

After ^{8}He dissociates into ^{6}He+2n at the target, the emission angle and energy loss
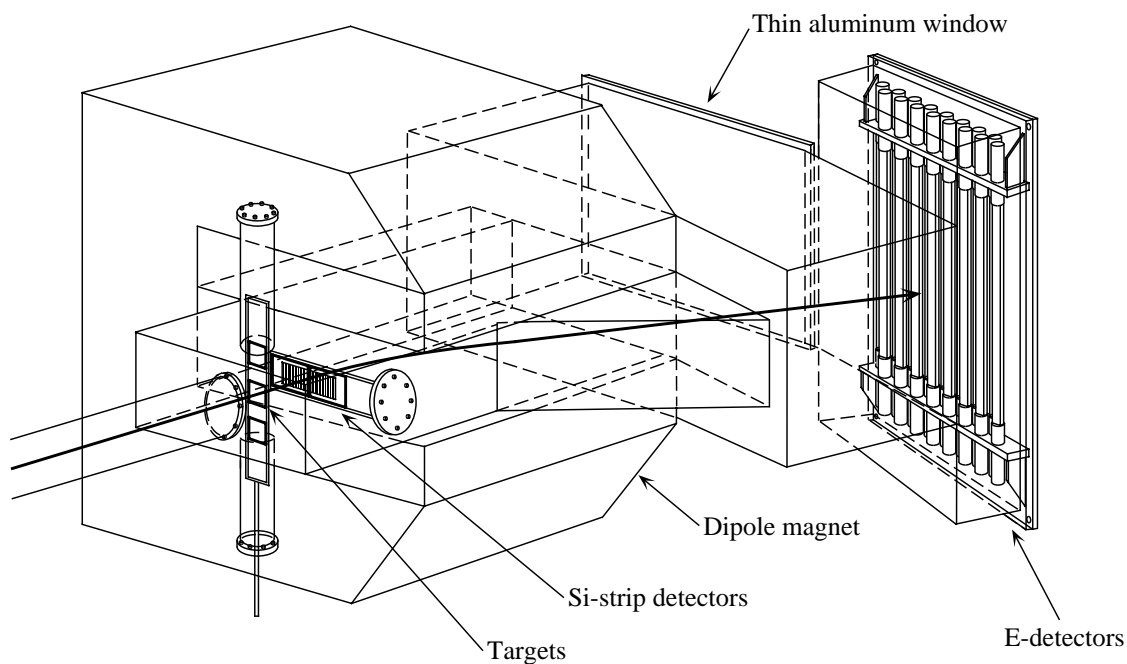
Figure 2.4: A schematic drawing of fragment detectors consisting of Si-strip detectors and E-detectors. The emission angle and the energy loss of the decay product ^{6}He are determined by the Si-strip detectors. Then, the ^{6}He is deflected by the field of the dipole magnet and is stopped in the E-detectors. All of the fragment detectors are installed in a vacuum chamber.

ΔE of ^{6}He are measured with the Si-strip detectors located downstream from the target. Then, ^{6}He is deflected by the field of the dipole magnet and is stopped in the E-detectors, giving a remnant energy E. Particle identification is made with the $\Delta E - E$ information, and a momentum vector of the ^{6}He ($\mathbf{p}_6$) is determined by the angle and the energy information.

Since beam particles also stop in the E-detectors, they may react with C and H in the E-detectors producing neutrons, γ-rays and high energy protons, which may be detected by the *Neutron Wall Array*. As the timing signals are the same as those of real events, those background events appear as coincidence events which are difficult to distinguish from real events by software and hardware means. Although ^{8}He beam (A/Z=4, 24.9 MeV/A) is deflected by 18.7 degrees by the dipole magnet, which is out of coverage of the *Neutron Wall Array* ($\pm$11.3 degree), those backgrounds are still not negligible. To further reduce the background events, sizable shielding materials consisting of copper and brass were placed behind the E-detectors. Hence, the backgrounds were effectively reduced by the shield.

The neutrons from ^{8}He dissociation at the target go straight through the vacuum chamber and are detected by the *Neutron Wall Array*. At the end of the chamber, a thin aluminum window supported with a honeycomb structure was used. The effective thickness of the window was about 2 mm, which produces almost negligible scattering and attenuation of the neutrons at the present energy.

2.3.1   Si-strip detectors

The Si-strip detectors are composed of two MICRON position-sensitive silicon double strip detectors (5 cm $\times$ 5 cm $\times$250 μm thick). Each detector has 16 horizontal strips on one side and 16 vertical strips on the other. The width of each strip is 3.125 mm. The two detectors are located at 15.2 cm downstream from the target and placed side by side. A schematic drawing of the detector layout is provided in Fig. 2.5.

Two detectors give 32 (horizontal) $\times$ 16 (vertical) square pixels. Position information
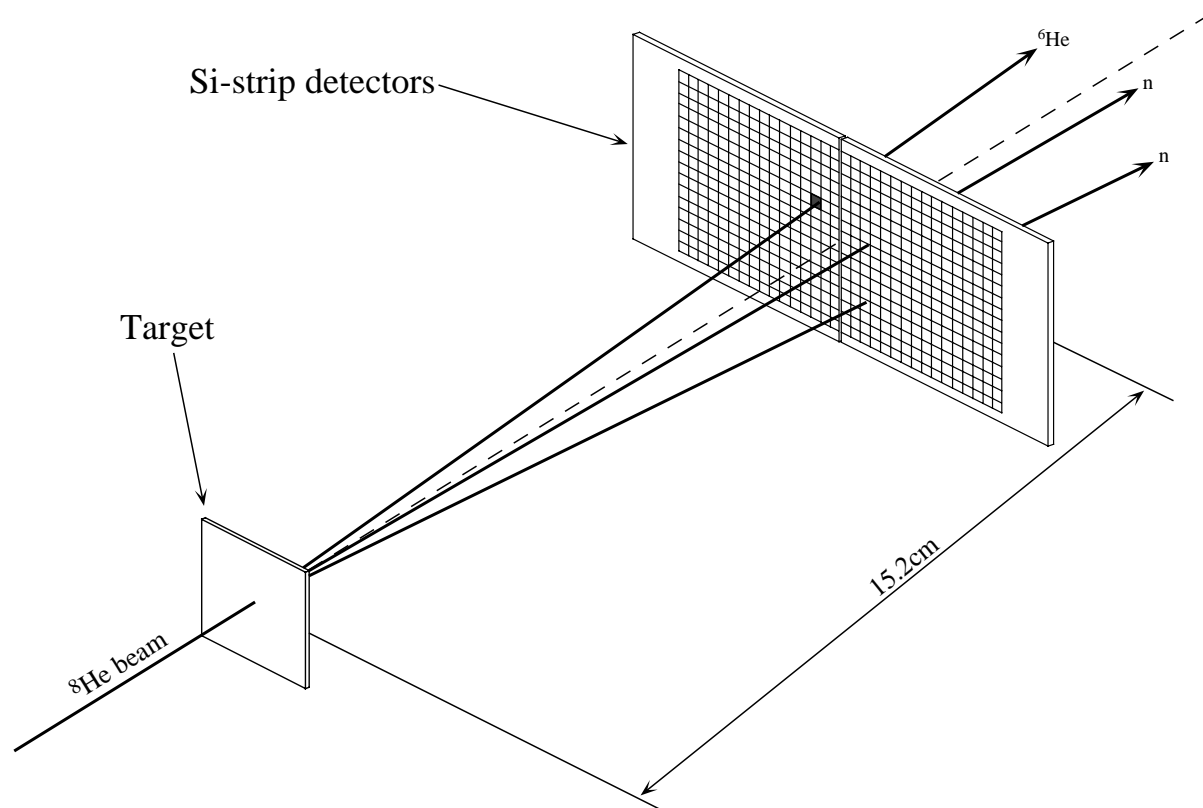
Figure 2.5: A schematic drawing of Si-strip detectors. The detectors consisting of two MICRON position-sensitive silicon double strip detectors give energy loss and emission angle information of charged fragments. Each detector has 16 horizontal strips on one side and 16 vertical strips on the other, so that two detectors can give 32 (vertical) × 16 (horizontal) square pixels position information. The emission angle is determined by the pixel which the fragment traversed. A typical energy and an angular resolution are about 8 % (FWHM) and 1.2 degree, respectively.

and the emission angle of the ^{6}He are determined by the pixel that the fragment traversed. The strip width and the distance from the target induce an ambiguity of about 1.2° × 1.2° in determination of the emission angle. Also, that distance and the overall size of the detectors define a geometrical acceptance for charged fragments of 18.2° (horizontal) × 9.3° (vertical). The corresponding ^{6}He momentum components are $|P_x| \leq 390$ MeV/c (horizontal) and $|P_y| \leq 200$ MeV/c (vertical) at the present beam energy.

An energy loss ΔE of charged particles is also obtained by the Si-strip detectors and used for particle identification. A detailed description of the particle identification is presented in section 3.1. A typical energy loss for the ^{6}He in the present beam energy was about 4.3 MeV, and the energy resolution was found to be better than 8 % FWHM.

2.3.2 E-detectors

A schematic drawing of the E-detectors is provided in Fig. 2.6. The detectors are composed of 16 Bicron BC-408 plastic scintillators, the size of each being 4 cm × 2 cm × 40.6 cm long. The 16 detectors are arranged vertically from high momentum side E1 (closer side to the beam axis) to low momentum side E16 and closely so that there is no dead space between them. The sensitive area covers 64 × 40.6 cm^2 in total.

After passing through the Si-strip detectors, ^{6}He is deflected by the magnetic field of the dipole magnet and stopped in the E-detectors. Scintillation light produced in the detector is read out by two photomultipliers (PMT's) attached to top and bottom ends. Then, signals from the PMT's are integrated with charge-sensitive analog-to-digital converters (QDC's). The light read out by the top and the bottom PMT's (Q_{top} and Q_{bottom}) depends on the vertical position where particle impinges, expressed as $Q_{top,bottom} = Q_0 e^{-(l/2 \pm x)/\lambda}$, where Q_0 is an initial luminosity, λ is an attenuation length, l is a length of the scintillator and x is a distance between center of the scintillator and the light source. Therefore, Q_0 can be deduced from

$$\sqrt{Q_{top} \cdot Q_{bottom}} = Q_0 e^{-l/(2\lambda)} \tag{2.1}$$

independent of the position.

16×Photomultipliers

16×plastic scintillators

E1

charged particles

E16

16×Photomultipliers
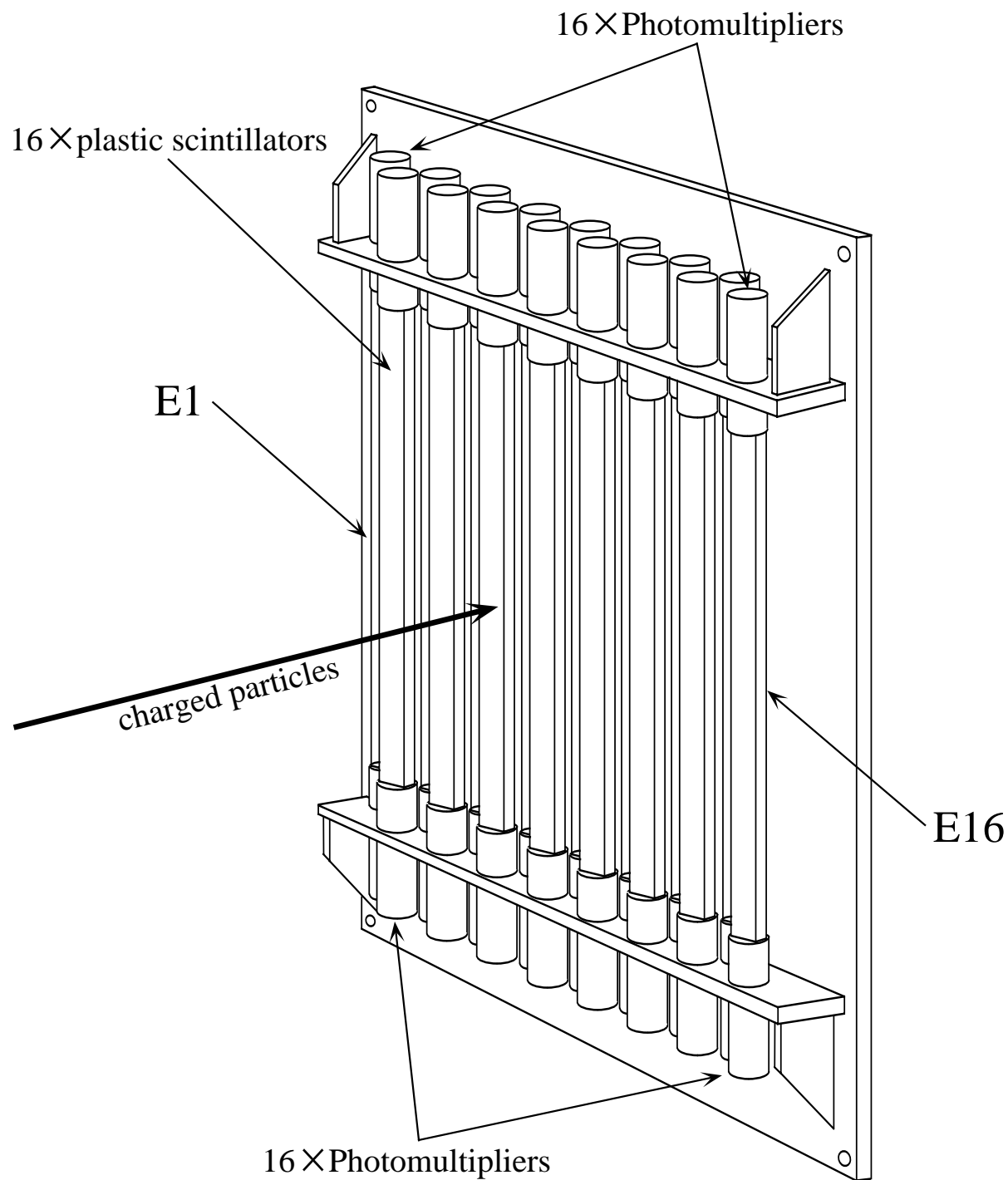
Figure 2.6: A schematic drawing of E-detectors consisting of the 16 Bicron BC-408 plastic scintillators (E1∼E16). Photomultipliers are attached to top and bottom ends of the each scintillator. Charged particles are deflected by the magnetic field of the dipole magnet and stopped in the detectors. Deposited energies of the charged particles are extracted by measurement of the light produced in the scintillator.

Since Q_0 is a nonlinear function of energy and also depends on the mass and charge of the incident particle, calibrations of the E-detectors were made for various isotopes at several energies. Details of the calibrations are described in Appendix A.2. As a result of the calibrations, a typical energy resolution for He-isotopes at the present beam energy is found to be better than 5 % FWHM.

2.3.3 Dipole magnet

The C-type dipole magnet with a pole area of 61.0×33.0 cm^2 and a gap height of 19.1 cm was installed to deflect charged particles. Prior to the experiment, the magnetic field was mapped with a Hall probe for four horizontal planes. One measurement was performed for a mid plane which was the same height as the beam axis, and the other three measurements were performed above the mid plane by 2.54, 5.08 and 7.62 cm. Below the mid plane, the field was assumed to be symmetric to that above the mid plane. The measured field in the mid plane is plotted in Fig. 2.7. In the figure, the beam axis is indicated by an arrow.

With the magnetic field mapped, trajectories of ions can be calculated. The calculated trajectories of He-isotopes at 24.9 MeV/A are shown in Fig. 2.8. In present setting, ^{8}He, ^{6}He and ^{4}He ions are typically deflected by 18.7, 23.9 and 32.5 degrees and detected with the E-detectors E2, E5 and E10, respectively. The beam particles, including the major impurity of ^{12}Be at 44 MeV/A, are mainly detected by E2, while ^{6}He is detected by E5. Hence, a clear separation between the beam particles and the ^{6}He is made.
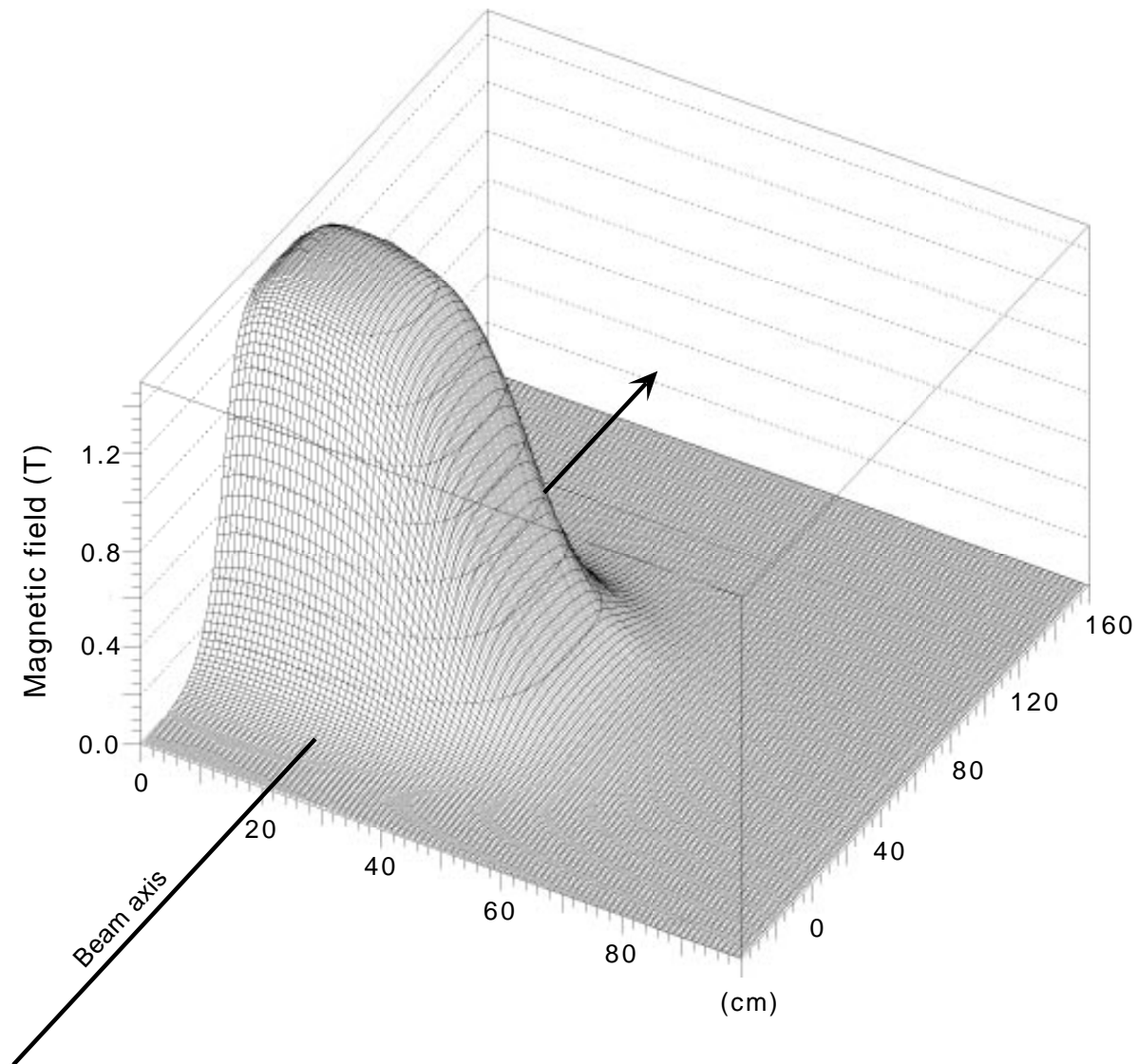
Figure 2.7: A measured magnetic field in the mid plane. The magnetic field in the central region of the pole is about 1.4 Tesla. The incident beam direction is indicated by an arrow.
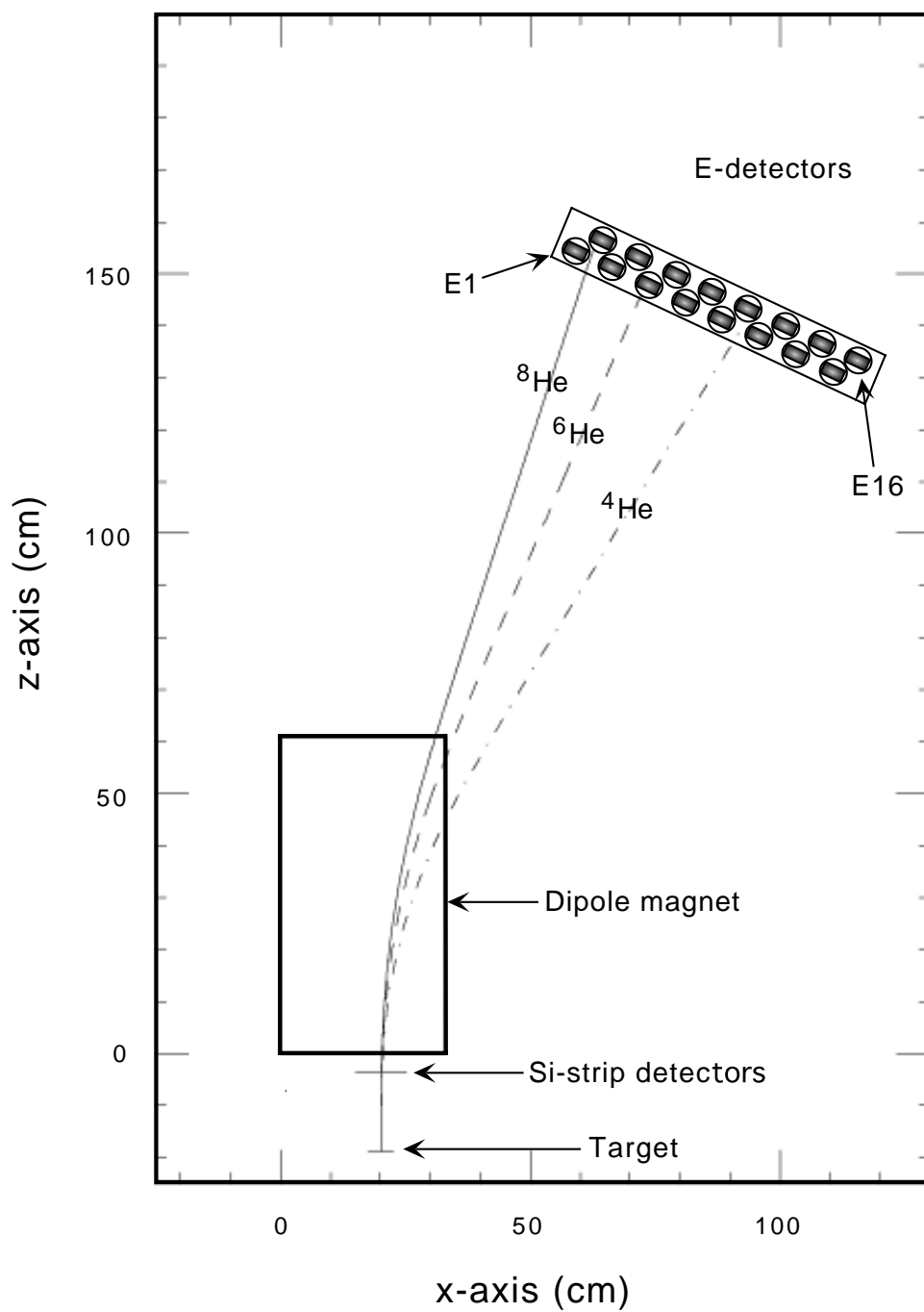
Figure 2.8: Calculated trajectories of He-isotopes at 24.9 MeV/A. In the present setting, ^{8}He, ^{6}He and ^{4}He are detected by E2, E5 and E10, respectively.

2.4   Neutron Wall Array

Large area position-sensitive neutron detectors, the *Neutron Wall Array*, was constructed
at the NSCL[27]. A picture of the *Neutron Wall Array* is presented in Fig. 2.9. The
wall consists of 25 position-sensitive neutron detectors. Each detector is made with Pyrex
rectangular glass cells with an inside size of 6.35 cm × 7.62 cm × 200 cm long filled with
NE-213 liquid scintillator. The 25 cells are horizontally mounted on an aluminum frame
so that the sensitive area is 2 m × 2 m in total. The outside of the each cell is not treated
with any reflective coating so that the scintillation light is collected only by total internal
reflection. To prevent light leak from the outside, the frame is covered by an aluminum
sheet as shown in Fig. 2.10. The thickness of the aluminum sheet is 0.8 mm which is
almost negligible for neutrons at the present energy.

The two walls consisting of the 50 cells are installed in the N4 vault of the NSCL and
arranged in two layers at 5m and 5.84m from the target position as shown in Fig. 2.1. The
two walls are centered at zero degrees because most of the neutrons from ^{8}He dissociation
are emitted at forward angles. Since the vertical opening angle of the dipole magnet,
determined by the gap height, is smaller than the acceptance of the *Neutron Wall Array*,
the 16 cells in the central region (out of the 25 cells) for the each wall were used in the
experiment.

The scintillation light produced in the cell is read out by two Philips Photonics
XP4312B/04 photomultipliers (PMT's) attached to the left and right ends. The time
difference between the two signals from the PMT's gives the horizontal position informa-
tion of the incident neutron. The time resolution is found to be better than 1 ns FWHM,
corresponding to a horizontal position resolution of 8 cm FWHM. On the other hand,
the vertical position information is obtained by the number of the cell fired. Thus, the
vertical position resolution is determined by the height of the cell (7.62 cm). With the
two-dimensional position information, a directional vector of the incident neutrons can be
determined. The energy of the neutrons can be determined by the time-of-flight (TOF)
obtained from the mean time of the PMT signals with respect to the mean time of the
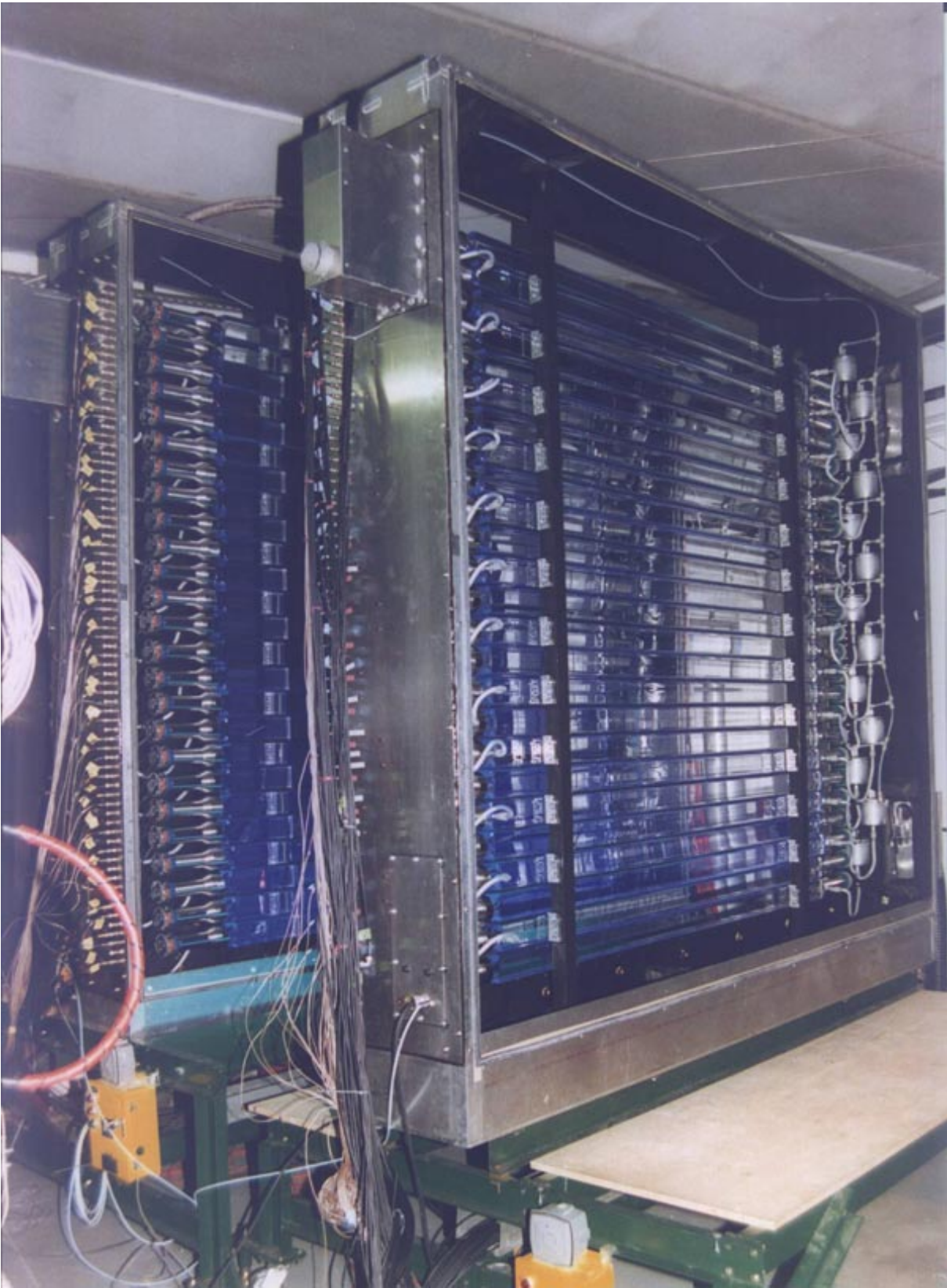
Figure 2.9: A picture of the *Neutron Wall Array*.
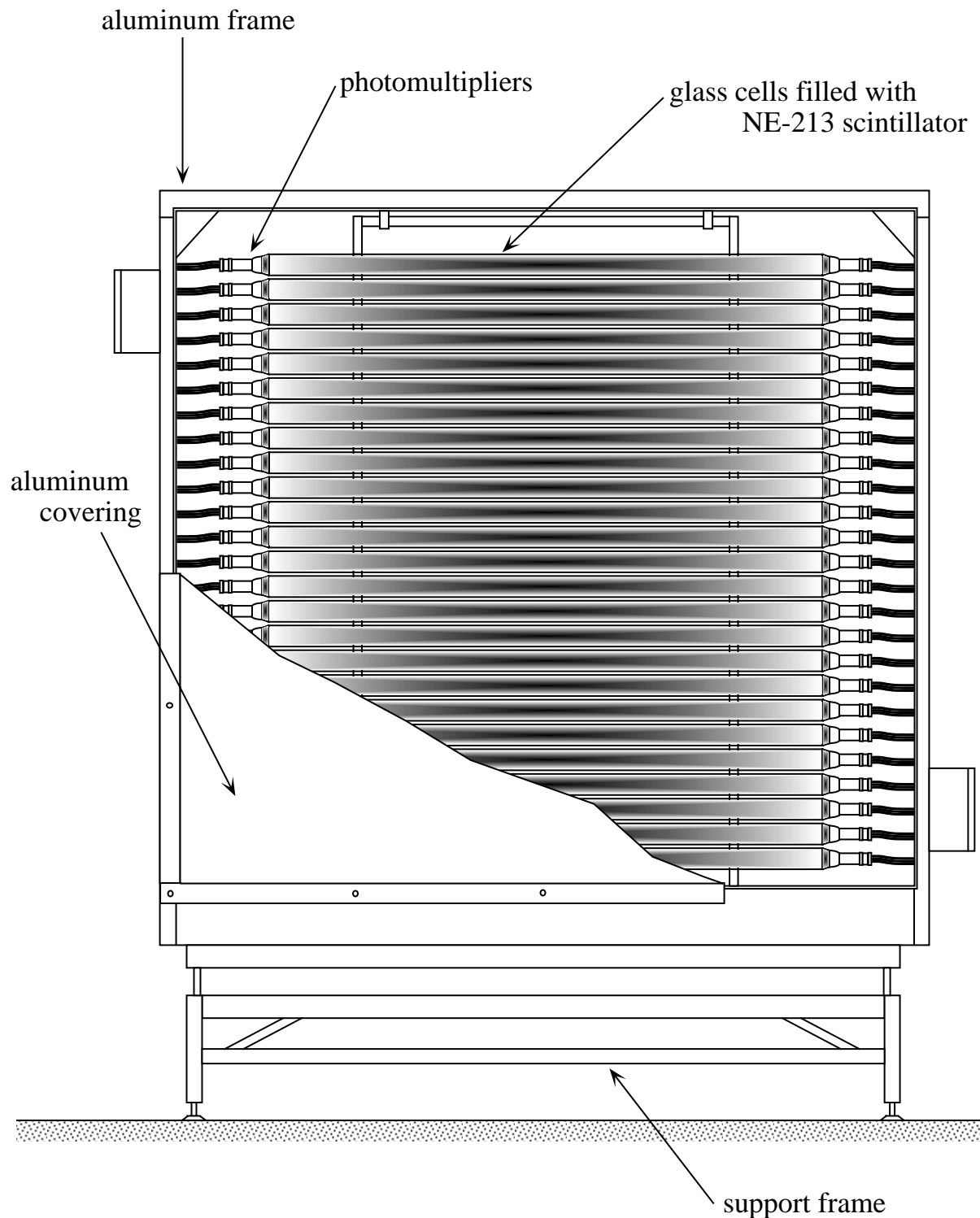
Figure 2.10: A schematic drawing of the *Neutron Wall Array*. The wall consists of 25 Pyrex rectangular glass cells filled with NE-213 liquid scintillator. The 25 cells are mounted on an aluminum frame and are covered by a thin aluminum sheet to prevent a light leak and to protect the glass. The thickness of the aluminum sheet is almost negligible for neutrons at the present energy.

fragment E-detector PMT signals. In the present setup, the resolution of the TOF measurements for 24 MeV neutrons is about 1.4 %, corresponding to an energy resolution of 2.8 %.

Since the *Neutron Wall Array* covers a large area, a large number of background γ-ray and cosmic-ray events is present during the experiment. By using the NE-213 liquid scintillator, each cell of the walls is capable of neutron/γ-ray discrimination by a pulse-shape discrimination (PSD) method. It is known that the light emitted by the NE-213 scintillator has two components, fast decay component and a slow component. The method utilizes the different ratio of the two components between neutrons and γ-rays. In the experiment, the signals from the PMT's were converted to a total and a fast component by pulse-shape circuits and integrated with charge-integrating FERA (Fast Encoding Readout ADC) units. The correlation between the charge-integrated pulse of the total (Q_{total}) pulse and the fast (Q_{fast}) component gives a clear neutron/γ-ray discrimination. A representative plot of the total pulse (Q_{total}) versus the fast component (Q_{fast}) for a cell in the *Neutron Wall Array* is provided in Fig. 2.11. The cell was irradiated with neutrons and γ-rays from a Pu-Be source. An inset of the figure shows the same plot, but for $Q_{total} \leq 2$ MeV electron equivalent (MeVee) region. A clear discrimination for $Q_{total} \leq 1$ MeVee is seen in the figure. The cosmic-ray pulses are in the same group as the γ-ray pulses.

2.5 Acceptance and resolution of the total detector system

To estimate the effect of the acceptance and the resolution of the total detection system, Monte Carlo simulations were performed. In the simulations, simple models, a sequential model or a direct model, were employed to describe the ^{8}He dissociation. The sequential decay model assumes that ^{8}He is excited by a target nucleus with a certain excitation energy and decays into the ^{7}He+n subsystem. Since ^{7}He is particle unstable with respect to neutron emission by 0.44 MeV, ^{7}He subsequently decays into ^{6}He+n (see Fig. 3.5).
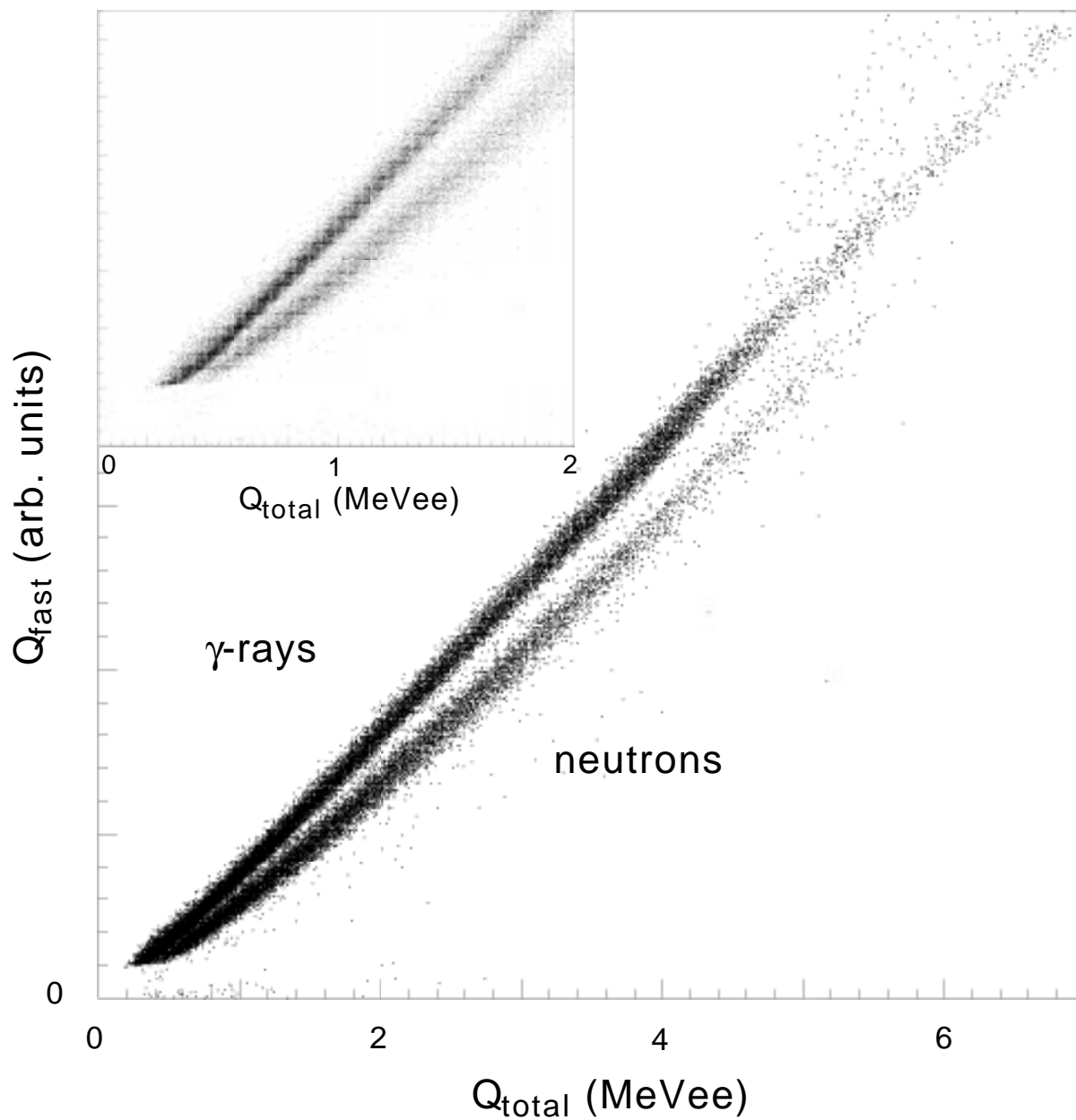
Figure 2.11: A representative plot of the total pulse (Q_{total}) versus a fast component (Q_{fast}) for a cell in the *Neutron Wall Array*. A clear discrimination between neutrons and γ-rays from a Pu-Be source is seen. An inset shows the same plot, but for $Q_{total} \leq 2$ MeVee.

On the other hand, the direct model assumes that the ^{8}He is excited and dissociates into ^{6}He+2n directly, where excitation energies are partitioned into ^{6}He and two neutrons according to the three-body phase space distribution. The simulations include all contributions of effects from the beam spreads in energy, angle, position on target, the target thickness, the multiple scattering in the target, intrinsic resolutions and acceptances of the detectors. Details of the model calculations are described in section 3.4.

The calculated acceptance according to the sequential and the direct models as a function of decay energy E_d (excitation energies above two neutron emission threshold) is shown by filled circles and open squares in Fig. 2.12(a), respectively, where the acceptance is defined as the ratio of the number of decayed particles recorded in the detector system to the total number of events. Two results are found to differ more and more as the decay energy increases, reaching a difference of 0.0032 at E_d=4.5 MeV, which is a 30 % effect. The difference over all decay energies between two models

The resolution of the decay energies is also estimated with the simulations as follows. The ^{8}He is assumed to be excited by a target nucleus to a certain excitation energy partitioned between the decay products depending on the models. Then, momenta of the decay products are calculated including the intrinsic resolutions and acceptances of each detector. With the momenta, the decay energy can be reconstructed. Ideally, the calculated decay energy distributions should be δ-functions. However, the finite acceptances and resolutions make it a finite width reflecting the resolution of the detection system for the respective decay energies. In this way, the distributions for E_d=0.5~4.5 MeV in 0.5 MeV steps were calculated according to the two models. Since the two results were almost identical, only the result assuming the sequential model is presented in Fig. 2.12(b). Consequently, the typical resolution is found to be about 0.38 MeV (FWHM) at E_d=1 MeV and roughly proportional to the square root of the decay energy.
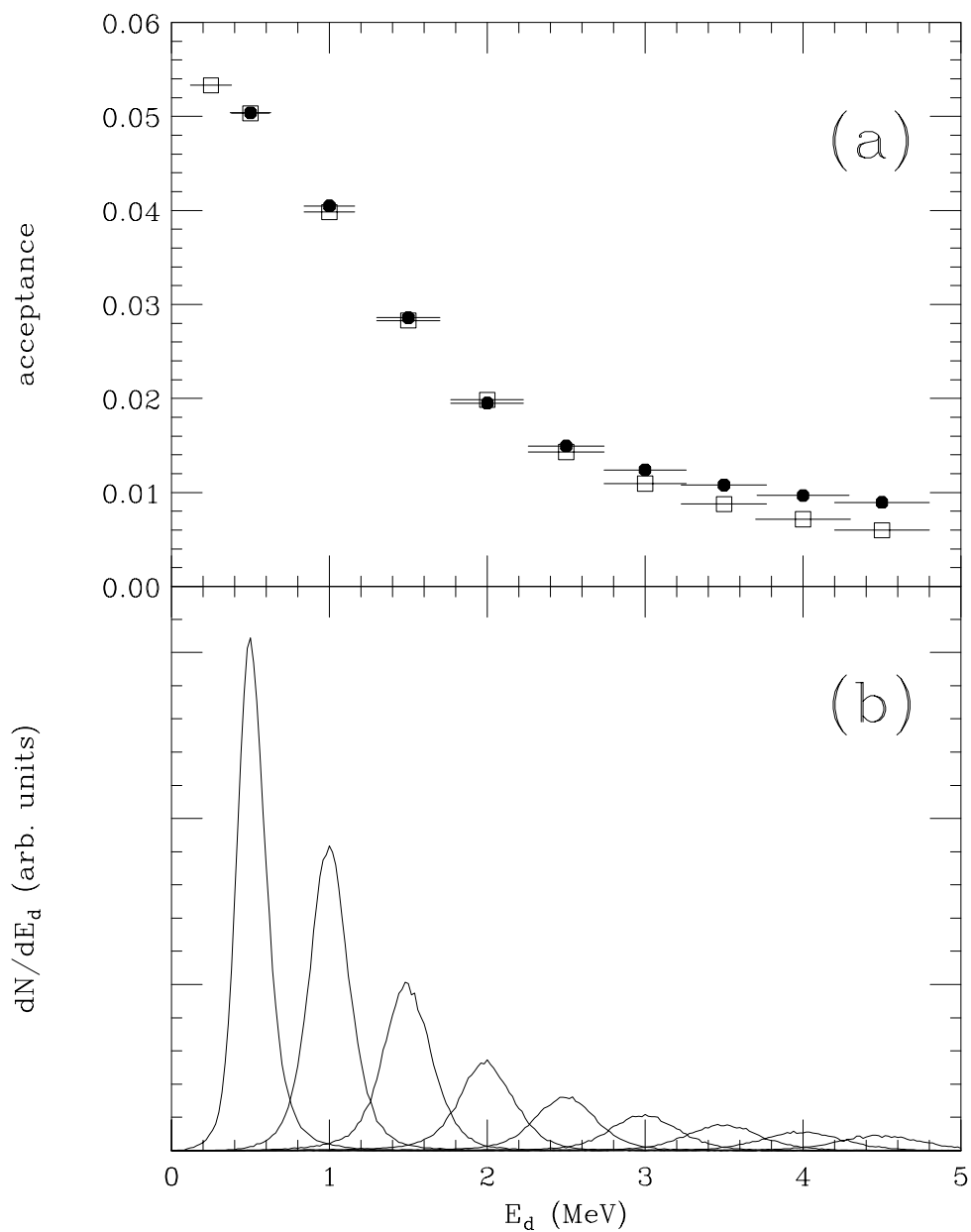
Figure 2.12: (a) Calculated acceptance of the total detector system as function of the decay energy E_d. Filled circles and open squares show results assuming the sequential and the direct model, respectively. (b) Decay energy distributions calculated for fixed decay energies. The distributions reflect the resolution of the total system for the respective decay energies.

Chapter 3

Results

This chapter describes results of the data analysis. In section 3.1, particle identification of charged fragments is described. After ^{6}He is identified, neutron removal cross sections are extracted and shown in section 3.2. Then, results from the ^{6}He+n+X coincidence data are described in section 3.3. Finally, results from the ^{6}He+2n coincidence data are described in section 3.4.

3.1 Fragment data

Charged fragments are identified with Si ΔE and plastic E signals from the fragment detectors. Fig. 3.1(a) shows a two-dimensional $\Delta E - E$ distribution for a sum of the 16 E-detectors, requiring a coincidence with more than one neutron. The abscissa shows energy per nucleon for ^{6}He particles. As the light response of the plastic scintillator depends on incident isotopes in general, the energy scale is not correct for particles other than ^{6}He.

In Fig. 3.1(a), two groups are seen. One group shows a locus of ^{8}He particles and has a horizontal tail to lower energies. Most of the events in the group have the same ΔE, but different Es. If ^{8}He dissociates in the E-detector, the Si ΔE signal is the same as that for a dissociation at the target, but an energy deposition in the E-detectors is different as neutrons carry out some energy. Hence, the tail events are attributed to ^{8}He dissociation in the E-detectors. The other group has the Si ΔE and the plastic E of about 2.8 MeV

38
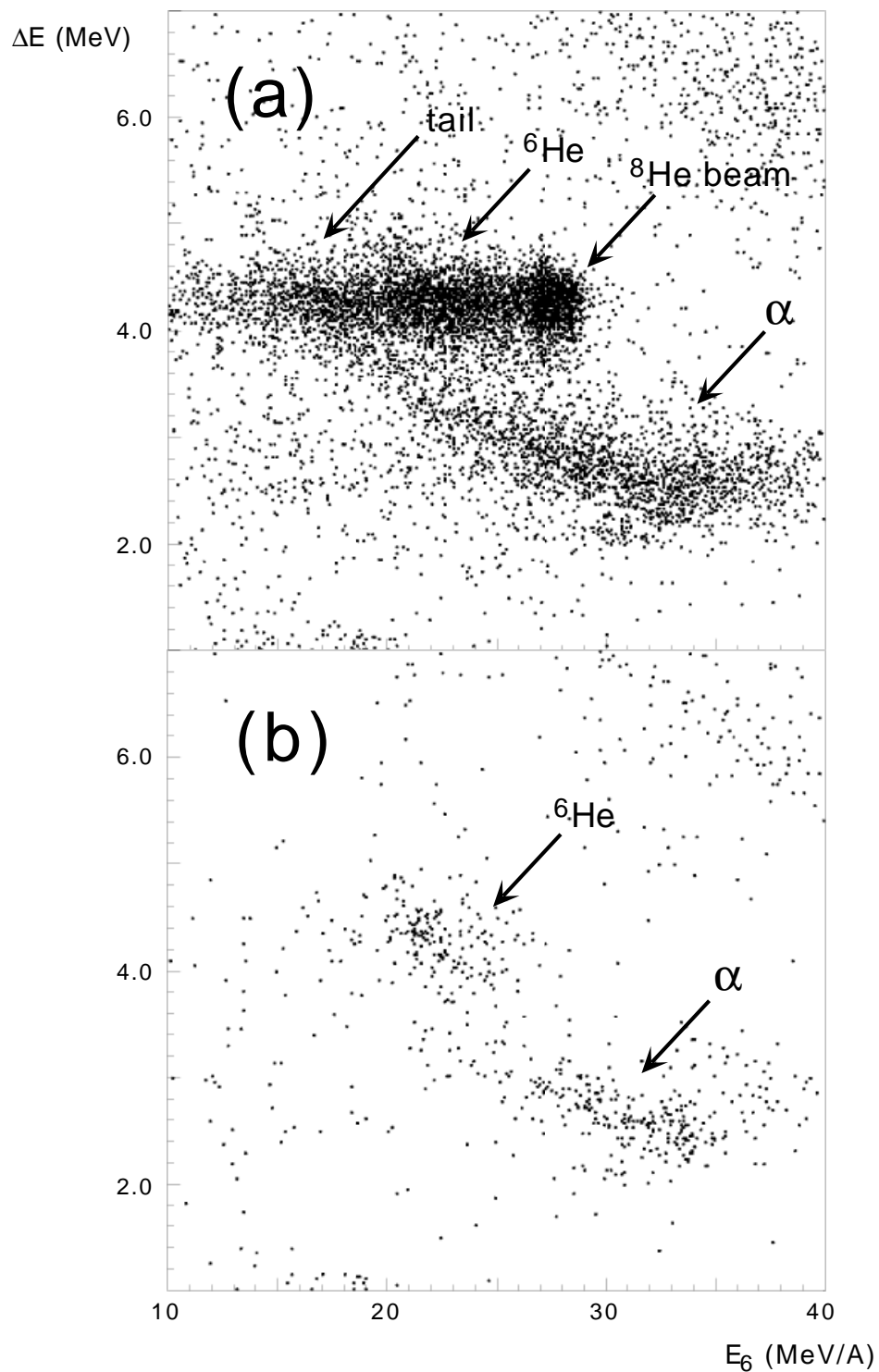
Figure 3.1: Two dimensional distributions of Si ΔE versus plastic E in which a coincidence with more than one neutron was required for (a) sum of the 16 E-detectors and (b) only E5. The abscissa is normalized for ^{6}He in units of MeV/A (see text).

and 40 MeV/A, respectively. This is found to be α particles produced in dissociation reactions of 44 MeV/A ^{12}Be particles, which are the major impurity of the incident beam.

Since the beam particles mainly inject into the E2 detector, the horizontal tail is not seen for the other E-detectors. Fig. 3.1(b) shows a similar distribution as Fig. 3.1(a), but only for E5. Instead of the horizontal tail, a locus corresponding to 22 MeV/A ^{6}He particles is seen, because the ^{6}He particles have different rigidity from the beam particles and are separated by the dipole magnet. With the $\Delta E - E$ distributions of the individual E-detectors, charged fragments can be well separated.

These particle identifications are further verified with one-dimensional distributions of particle identification (PID) number. The PID number is defined as follows. An empirical relation between the light-output of the scintillator L and the deposited energy E is[28]

$$ L \propto \frac{E^{1.12}}{Z^{0.633} A^{0.301}} \tag{3.1} $$

in the present energy region. Then, the energy loss in the Si-strip detectors ΔE can be approximated as

$$ \Delta E \propto Z^2 \left(\frac{E}{A}\right)^{-0.796} \tag{3.2} $$

for various particles. With two relations, the PID number can be defined as

$$ \mathrm{PID} \equiv L(\Delta E)^{1.41} \propto Z^{2.19} A^{0.820} \tag{3.3} $$

The PID number for ^{8}He is adjusted to be 135, so that the numbers for ^{6}He and α are calculated to be 105 and 75, respectively.

Fig. 3.2(a) shows a distribution of the PID number for He isotopes, requiring a coincidence with more than one neutron. Note that ^{6}He is not selected with the $\Delta E - E$ distributions in the figure, but a peak around PID=105 corresponding to ^{6}He is observed. In addition, two peaks corresponding to α and ^{8}He and a bump between the peaks of α and ^{6}He are also observed, even though the distribution results from subtraction of target-out runs in order to reject events from reactions in the E-detectors and the Si-strip detectors.
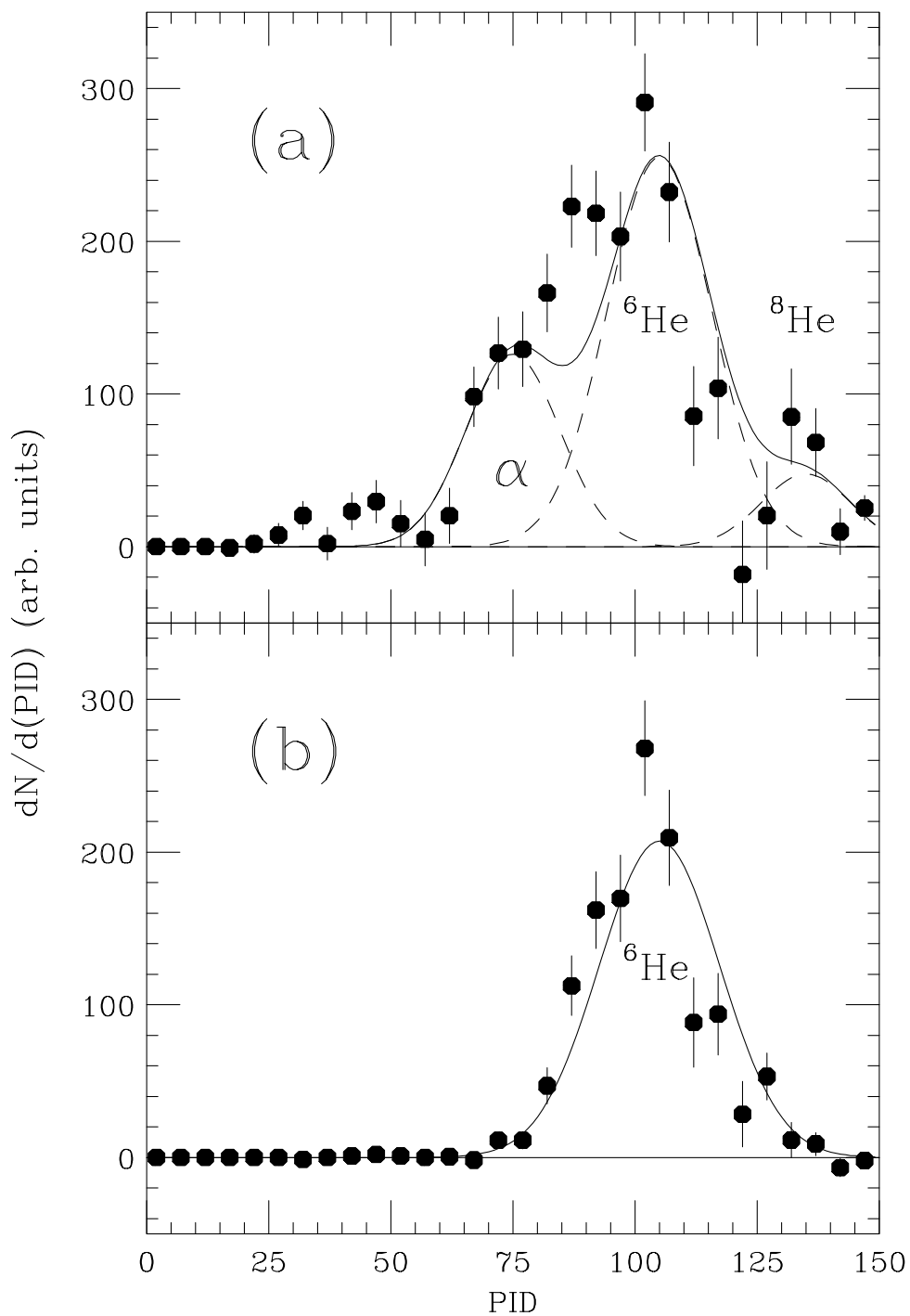
Figure 3.2: (a) A PID distribution requiring in which a coincidence with more than one neutron was required. The solid line shows a fit with a triple-gaussian distribution. (b) A similar distribution, but using one of the individual E-detectors (see text). The solid line shows a fit with a single gaussian distribution. A clear separation is seen in the distribution.

It is worthwhile to point out why the events on these peaks were not removed by subtraction of the target-out runs. There are two possible reasons for these unsubtracted events. One reason is the beam impurity of 44 MeV/A ^{12}Be. When the ^{12}Be particles dissociate in the target into charged particles such as α, these events may be detected in coincidence with neutrons and not be subtracted by the target-out runs. In fact, most of the α particles on the PID distribution have energies of 40 MeV/A similar to the energy of 44 MeV/A ^{12}Be after passing through the target and the Si-strip detectors. The other reason is the subtraction of the spectrum by the target-out runs. As mentioned previously, many reaction events at the E-detectors from the ^{8}He dissociation are observed, appearing as the 'horizontal tail' on the $\Delta E - E$ distribution. When the dissociation occurs at the E-detectors, neutrons may escape from the detectors and be detected by the Neutron Wall Array. To prevent such events, the sizable shielding materials have been placed behind the E-detectors as mentioned in section 2.3. Owing to a limited size of the shielding materials, these events have not been completely suppressed for the target-in runs. Furthermore, a contribution of beam spread caused by the multiple Coulomb scattering at the target is not negligible where there is no contribution for the target-out runs. Thus, condition of the subtraction between the target-in/out runs is not exactly the same. As a result, the subtraction may not be perfect.

In order to separate the ^{6}He particles from the other charged fragments accurately, 16 two-dimensional $\Delta E - E$ distributions were made, one for each E-detector are made. See Fig. 3.1(b), for instance, where only the ^{6}He particles are selected by the distributions for each E-detector. The separation is verified in a PID distribution as shown in Fig. 3.2(b), which is a similar distribution to that Fig. 3.2(a), but it selects only ^{6}He. Consequently, a clear separation is seen in the distribution. After ^{6}He is identified, the energy distribution of ^{6}He is obtained as shown in Fig. 3.3. In the figure, a symmetric peak around E_6=132 MeV is seen.
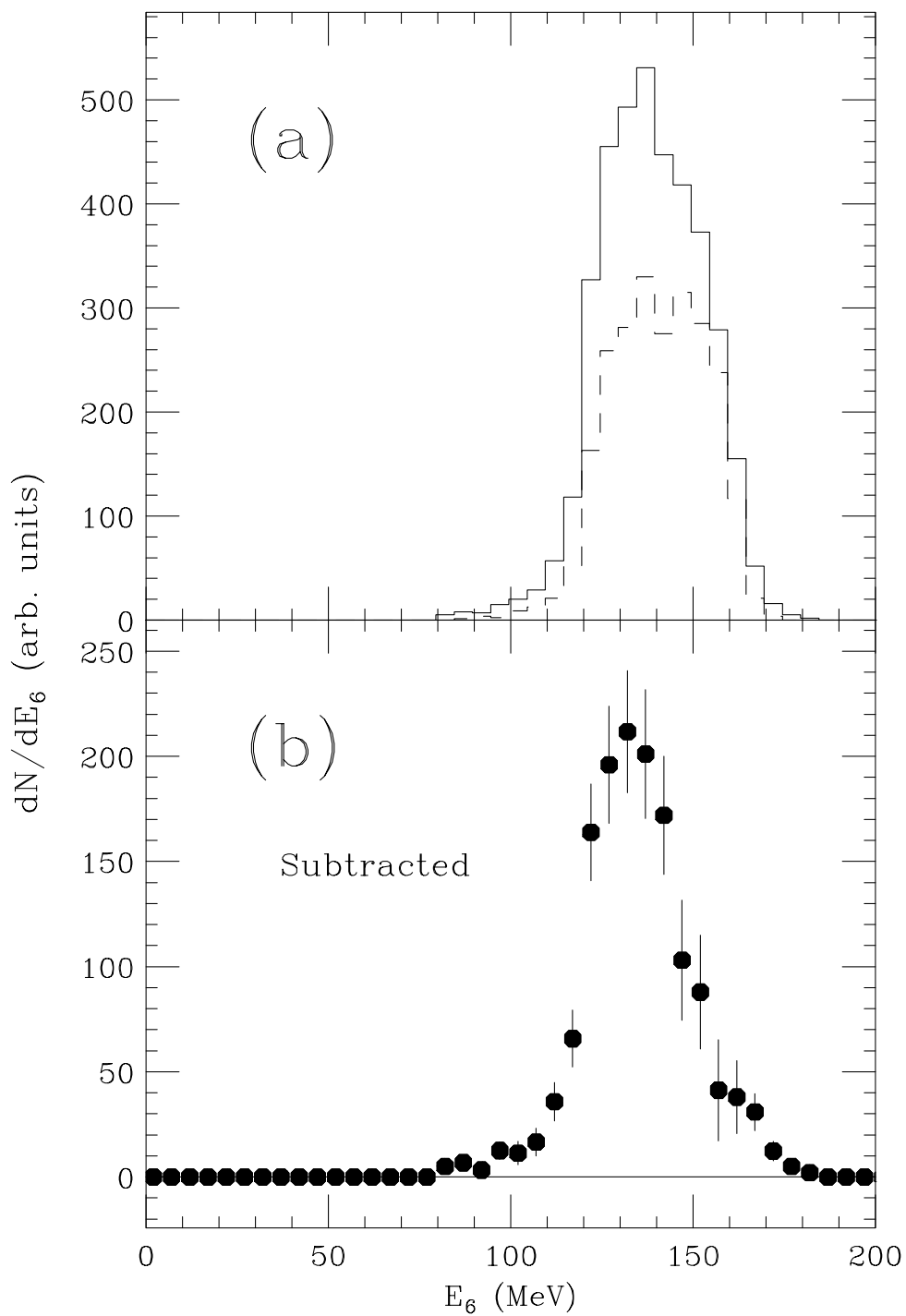
Figure 3.3: (a) Distributions of ^{6}He energy E_6 for the Pb target (solid histogram) and the target-out (dashed histogram). The distribution for the target-out was normalized to the Pb target runs for the same number of incident ^{8}He. (b) A similar distribution, but with subtraction of the normalized target-out runs.

3.2 Neutron removal cross sections

After the ^{6}He identification, 2n-removal cross sections σ_{-2n} can be extracted from three sets of data, *i.e.*, fragment singles (^{8}He→^{6}He+X), ^{6}He+n+X coincidences (^{8}He→^{6}He+n+X) and ^{6}He+2n coincidences (^{8}He→^{6}He+2n) data. Since the fragment singles data were downscaled by a factor of 500, sufficient statistics were not obtained to determine the 2n-removal cross sections. For the 4n-removal channel, ^{4}He+n+X coincidence data (^{8}He→^{4}He+n+X) were used to extract the 4n-removal cross sections σ_{-4n}.

To obtain the cross sections from the neutron coincidence data, the acceptance of the total detector system needs to be estimated. Because of the complexity of the system, the acceptance could not be calculated in a straightforward manner. To evaluate all contributions of the system, Monte Carlo simulations were performed. Details of the simulations have been described in section 2.5. As discussed there, the acceptance depends on the model. Thus, a systematic error of the acceptance was determined by two components, *viz.* , the uncertainty in the calculated neutron detection efficiency and the uncertainty depending on the model. As a result, the acceptance to detect 1n and 2n out of 2n (^{8}He→^{6}He+n+X and ^{8}He→^{6}He+2n) and 1n out of 4n (^{8}He→^{4}He+n+X) are estimated to be 25.7±4.0 %, 3.0±0.7 % and 38.7±0.1 %, respectively. With these acceptances, the cross sections for the three targets are obtained and summarized in Table 3.1, and the cross sections as functions of target charge are plotted in Fig. 3.4.

As listed in the table, the 2n-removal cross sections extracted from ^{6}He+n+X and ^{6}He+2n coincidence data differ by a factor of about two. Similar results have also been reported by the GSI experiments[22]. They have measured the nuclear breakup reactions of ^{8}He at 240MeV/A on a C target and found that an average neutron multiplicity in coincidence with a ^{6}He fragment was close to one. These results could be explained by assuming that the dominant dissociation of ^{8}He into ^{6}He+2n is connected with a 1n-removal process, *viz.*, a sequential decay via an intermediate state of ^{7}He. This assumption is further verified with relative energy distributions of the ^{6}He+n system and momentum distributions described in section 3.3. In this picture, the first neutron removed by a target

Data set	Quantity	^{208}Pb	^{120}Sn	^{27}Al
^{8}He→^{6}He+n+X data	σ_{-2n}	0.39±0.07	0.33±0.06	0.13±0.02
^{8}He→^{6}He+2n data	σ_{-2n}	0.21±0.06	0.21±0.06	0.048±0.016
	σ_{-2n}(Coulomb)	0.13±0.07	0.14±0.06	(0.00)
	σ_{-2n}(nuclear)	0.078±0.026	0.068±0.023	(0.048)
^{8}He→^{4}He+n+X data	σ_{-4n}	0.050±0.003	0.037±0.003	0.031±0.002

Table 3.1: The obtained 2n (σ_{-2n}) and 4n (σ_{-4n}) removal cross sections for three target. The values are in units of barns.

nucleus would be largely scattered out or absorbed by the target nucleus and may not be detected with neutron counters. This may decrease the multiplicity of neutrons. With the cross sections, the reaction channel of the process is estimated to occupy approximately 60 % of the total for the Al target. This result is comparable to that of the GSI experiments. For the Sn and the Pb target, approximately 40 % of the reaction channel is required to explain the cross sections. Since the process is attributed to the nuclear interaction and a ratio of the nuclear interaction to the Coulomb interaction decreases as the target charge increases, the process may be suppressed for the heavier target.

As mentioned previously, the dissociation cross section has the Coulomb component and the nuclear component as $\sigma_{-2n} = \sigma_{Coul} + \sigma_{nucl}$. To evaluate the nuclear component, the nuclear dissociation cross section σ_{nucl} is assumed to be factorized as[29]

$$\sigma_{nucl} = \gamma_P \gamma_{PT} \qquad (3.4)$$

$$\gamma_{PT} = R_I(P) + R_I(T) \qquad (3.5)$$

where γ_P is constant length and $R_I(P)$ (=2.48±0.03 fm[1]) and $R_I(T)$ are interaction radii of a projectile and a target, respectively. The constant γ_P can be obtained with an assumption of negligibly small Coulomb dissociation cross section σ_{Coul} for the Al target. With the above relations, the nuclear dissociation cross sections can be estimated from the 2n-removal cross section extracted by the ^{6}He+2n coincidence data and shown by the dashed curve in Fig. 3.4. Furthermore, the estimated Coulomb and nuclear dissociation cross sections are summarized in Table 3.1.
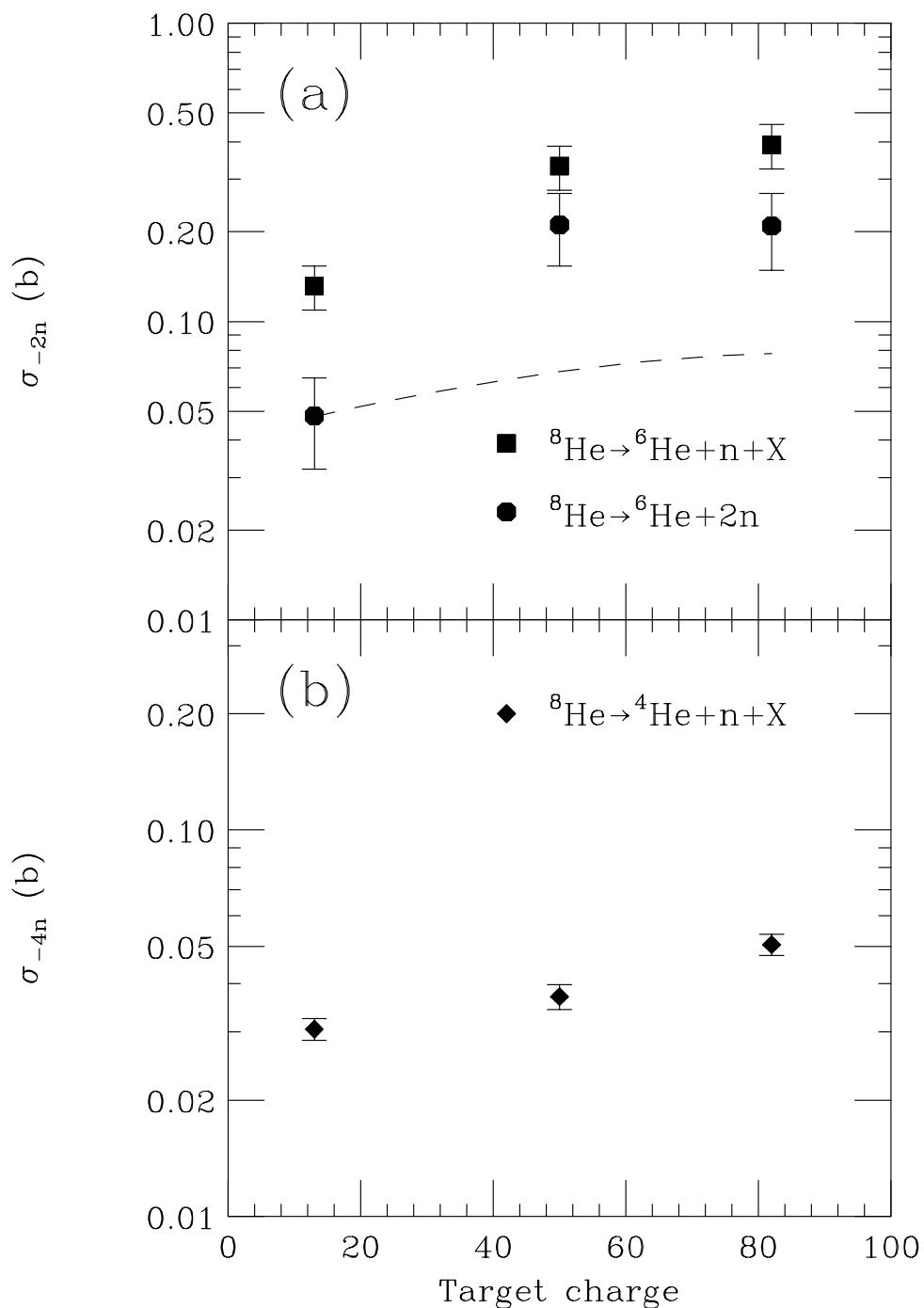
Figure 3.4: Target charge dependence of (a) 2n (σ_{-2n}) extracted from the ^{6}He+2n data (filled circle) and the ^{6}He+n+X data (filled square) and (b) 4n (σ_{-4n}) removal cross sections extracted from the ^{4}He+n+X data. The dashed curve shows an estimated nuclear dissociation cross section assuming negligibly small Coulomb dissociation cross sections for the Al target (see text).

Quantity	Energy (MeV/A)	Target	Cross section(b)
σ_{-2n}			
^{8}He→^{6}He+n+X (ref.[21, 22])	240	^{12}C	0.27±0.03
^{8}He→^{6}He+X (ref.[3])	800	^{12}C	0.202±0.017
σ_{-4n}			
^{8}He→^{4}He+X (ref.[3])	800	^{12}C	0.095±0.009
$\sigma_{-2n}+\sigma_{-4n}$			
^{8}He→^{6}He+X or ^{4}He+X (ref.[30])	0∼53.4	^{28}Si	0.55±0.03

Table 3.2: Summary of two (σ_{-2n}) and four (σ_{-4n}) neutron removal cross sections taken from references.

Previously, 2n (σ_{-2n}) and 4n (σ_{-4n}) removal cross sections of ^{8}He on light targets have been measured by projectile fragmentation reactions of 240 MeV/A[21, 22] and 800 MeV/A[3] ^{8}He on a C target and 0∼55.3 MeV/A ^{8}He on arrays of Si-detectors[30]. The cross sections taken from the references are summarized in Table 3.2. Results of refs. [3, 21, 22] are close to the present result on the Al target, even though the beam energies of the other measurements are higher. While beam energies of the measurements of the ref.[30] are close to those of our measurement, the obtained result on the Al target differs by more than a factor of two. Since the 2n and the 4n removal cross sections could not be extracted from the fragment singles data, as mentioned previously, the results obtained may not be directly compared with their results. However, the discrepancy may possibly be attributed to a contribution of a two neutron absorption process. For further analysis, this contribution needs to be taken into account.

3.3 ^{6}He+n+X coincidence data

This section describes results of the analysis of the ^{6}He+n+X coincidence data. Section 3.3.1 describes relative energy distributions of the ^{6}He+n system suggesting the sequential decay mechanism via the intermediate state of ^{7}He. This assumption is further justified by momentum distributions of neutrons described in section 3.3.2.

3.3.1 Relative energy distributions of ^{6}He+n system

As discussed previously, the discrepancy of the 2n-removal cross sections extracted from the ^{6}He+n+X and the ^{6}He+2n coincidence data can be explained with the assumption of the sequential decay mechanism via the intermediate state of ^{7}He (see Fig. 3.5). The sequential decay mechanism could be verified with the relative energy distributions of the ^{6}He+n system, because the ground state of ^{7}He would manifest itself in the relative energy distributions.

The relative energy of the ^{6}He+n system is given by

$$E_{6-\mathrm{n}} = \sqrt{(\varepsilon_6 + \varepsilon_\mathrm{n})^2 - (\mathbf{p}_6 c + \mathbf{p}_\mathrm{n} c)^2} - (M_6 + M_\mathrm{n})c^2 \qquad (3.6)$$

where ε, $\mathbf{p}$ and M denote the total energy, the momentum and the rest mass of relevant particles. The distribution for the Al target is provided in Fig. 3.6.

Having described the experimental distribution, let us now turn to discuss a model calculation via a Monte Carlo simulation. According to the analysis of the two neutron removal cross sections discussed previously, 60 % of the ^{8}He dissociation is assumed to proceed via the intermediate state of ^{7}He (path (a) in Fig. 3.5). Since ^{7}He is particle unstable with respect to neutron emission by 0.44 MeV, the ^{7}He nucleus subsequently decays into ^{6}He+n with a Breit-Wigner type function given by

$$I_{BW}(E_{6-\mathrm{n}}) \propto \frac{1}{2\pi} \frac{\Gamma(E_{6-\mathrm{n}})}{(E_{6-\mathrm{n}} - E_0)^2 + (\Gamma(E_{6-\mathrm{n}})/2)^2} \qquad (3.7)$$

$$\Gamma(E_{6-\mathrm{n}}) = \Gamma_0 \frac{T(E_{6-\mathrm{n}})}{T(E_0)}$$
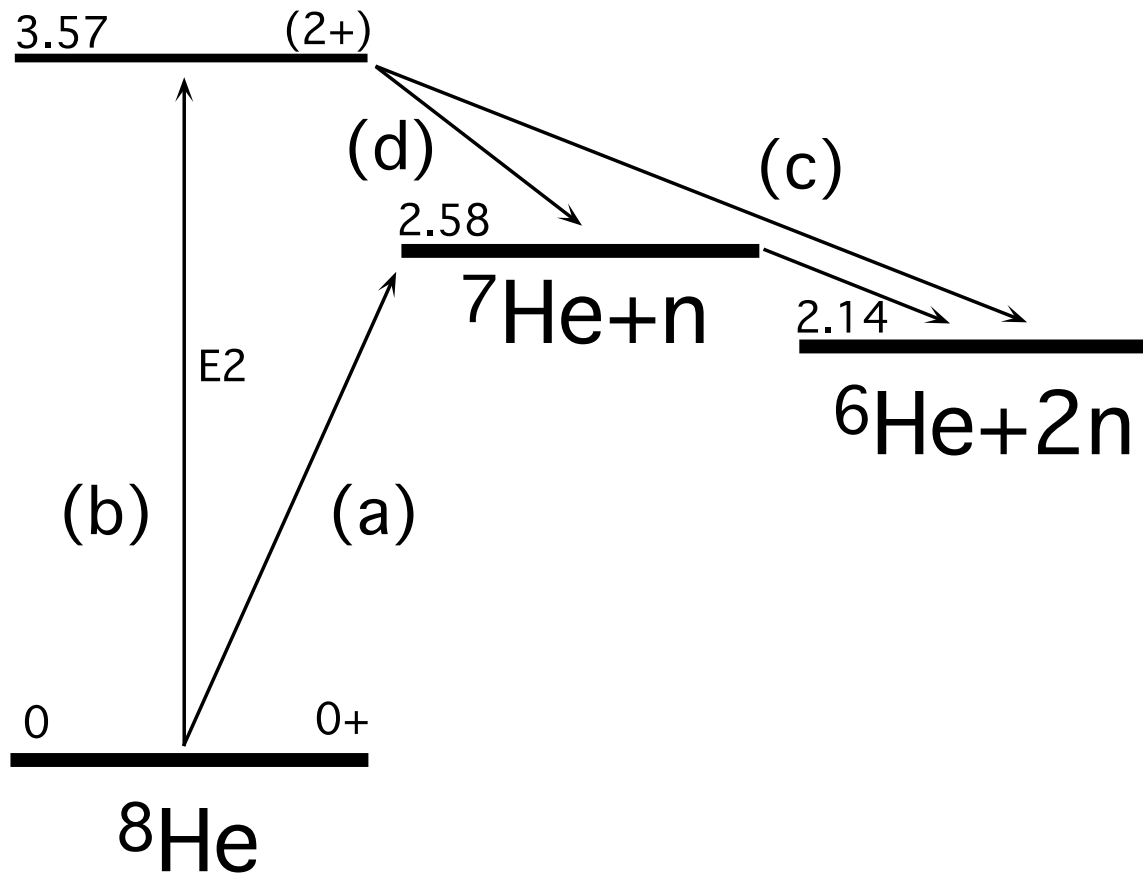
Figure 3.5: Level scheme for the sequential decay mechanism of ^{8}He.

where the resonant energy E_0 and the width Γ_0 are taken to be 0.44 and 0.16 MeV, respectively, corresponding to the ground state of ^{7}He[31]. The width $\Gamma(E)$ is energy dependent, and spin $J^\pi=3/2^-$ for ^{7}He, a transmission coefficient of p-wave neutrons $T(E)$ is included. Owing to the energy dependence of the width, the Breit-Wigner function gives an asymmetric shape and reaches zero at $E_{6-\mathrm{n}}=0$. On the other hand, the other 40 % of the dissociation is assumed to proceed via the first excited state of ^{8}He (path (b) in Fig. 3.5). A detailed description of the decay via the first excited state is found in section 3.4.2. The simulation also includes all contributions of effects from spreading of the beam, energy straggling of the fragment in the target, a detector acceptance and resolutions of the detector system. The result of the Monte Carlo simulation is shown by the histogram in Fig. 3.6. The distribution of the data points is well reproduced by the simulation. This
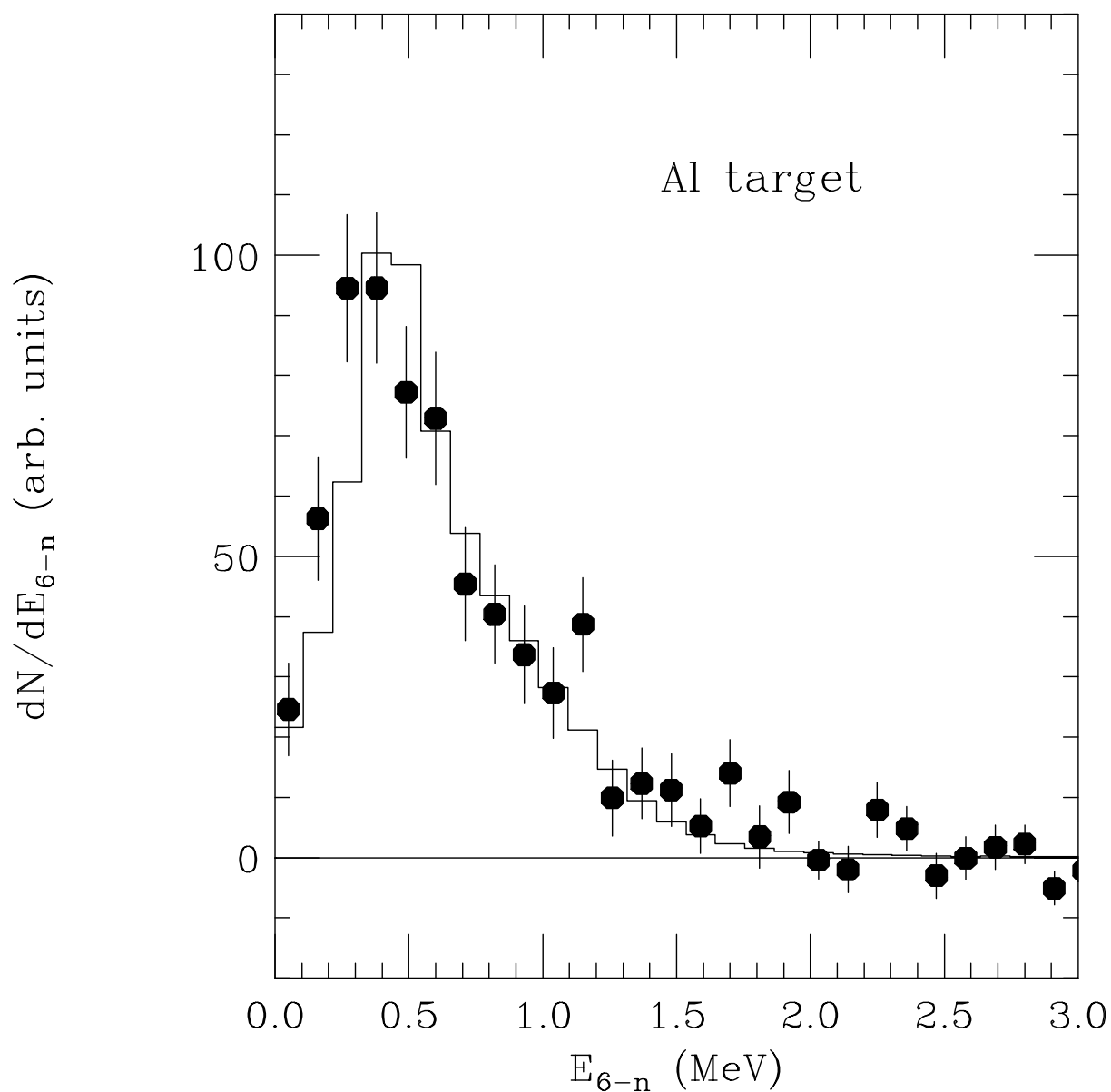
Figure 3.6: Relative energy distribution of ^{6}He+n system for the Al target. The histogram shows the result of the Monte Carlo calculation assuming the sequential decay mechanism via the intermediate state of ^{7}He with 40 % admixture of the direct decay process (see text). The points are the experimental data.
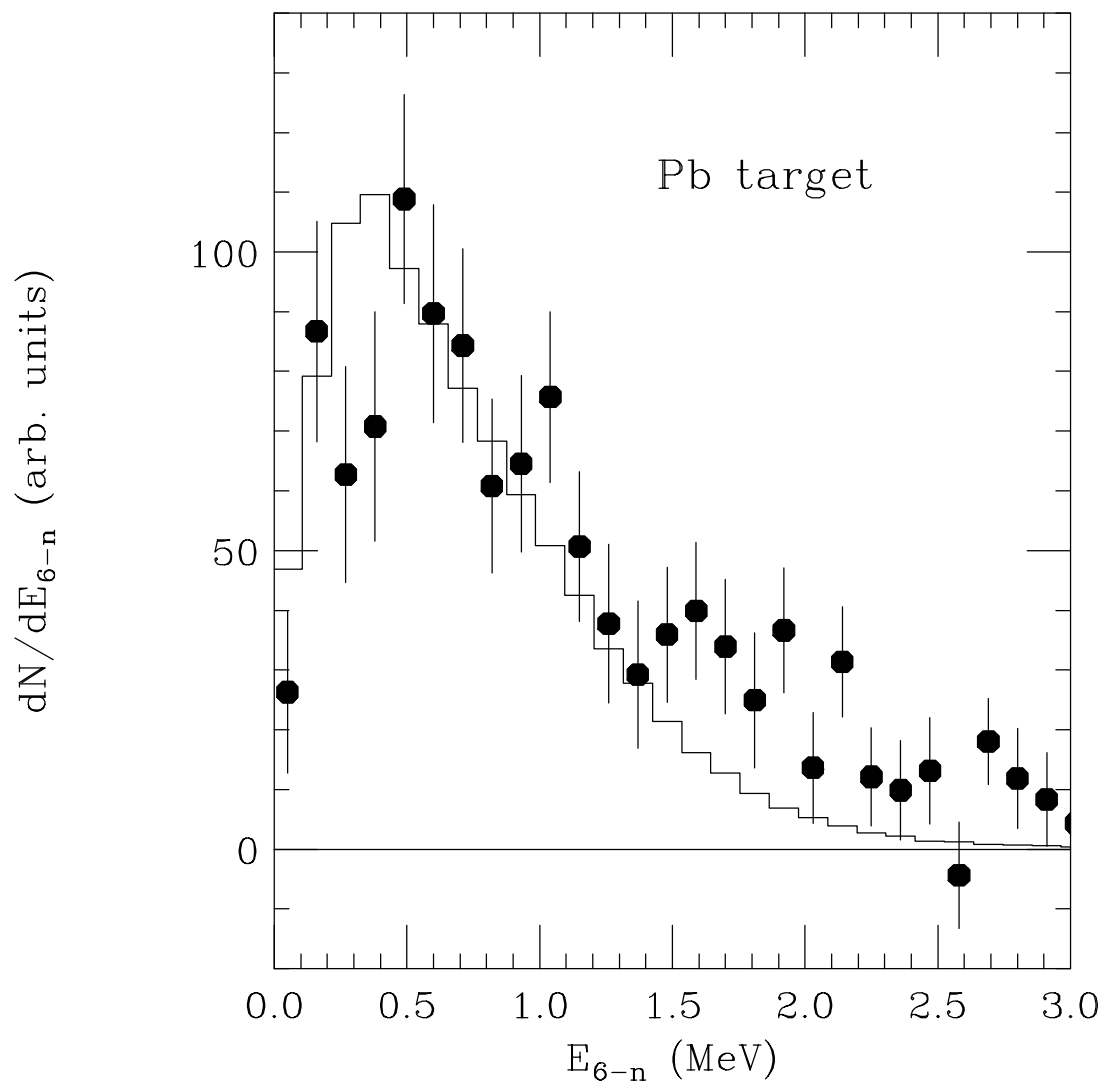
Figure 3.7: Relative energy distribution of ^{6}He+n system for the Pb target. The histogram shows the result of a Monte Carlo calculation assuming the sequential decay mechanism via the intermediate state of ^{7}He with 60 % admixture of the direct decay process (see text). The points are the experimental data.

indicates validity of sequential decay property in ^{8}He dissociation.

Furthermore, the relative energy distribution for the Pb target was reconstructed, and it is shown by the points in Fig. 3.7. In contrast to the distribution for the Al target, the Pb distribution is rather broad and has a tail at the higher energies. As discussed in section 3.2, approximately 40 % of the sequential decay process for the Pb target is required to explain the neutron removal cross section. While the other 60 % of the decay channel is attributed to a direct decay via the $E1$ Coulomb excitation discussed in section 3.4.2. To describe the measured distribution, a Monte Carlo simulation assuming the sequential decay mechanism with 60 % admixture of the direct decay process was performed. The result of the simulation is shown by the histogram in the figure. It is seen that the measured distribution roughly agrees with the simulation.

3.3.2 Neutron momentum distributions

In studies of nuclear structure of light neutron-rich nuclei, there has been much interest in momentum distributions of fragments and neutrons from projectile fragmentation reactions. For instance, measurements of the transverse momentum distributions of ^{9}Li from the projectile fragmentation of 800 MeV/A ^{11}Li were performed at the Bevalac in the LBL and they found that the momentum distributions of ^{9}Li have an extremely narrow width[3]. Assuming simple models, such as the Serber model[32] or the sudden approximation, the momentum distribution can be related with internal motion of the nuclei. Since the momentum distribution of ^{9}Li is equivalent to that of the center of mass (c.m.) of the two neutrons, the narrow width is interpreted as a large spatial extent of the two neutrons in ^{11}Li.

Transverse and longitudinal momentum distributions of neutrons in coincidence with the ^{6}He fragments were extracted from the present data. The distributions for the Al target are displayed in Fig. 3.8. Owing to the limited acceptance of the detector system, the transverse component of the momentum distribution has a narrow width compared to that of the longitudinal component. To take the contributions of these detector acceptance
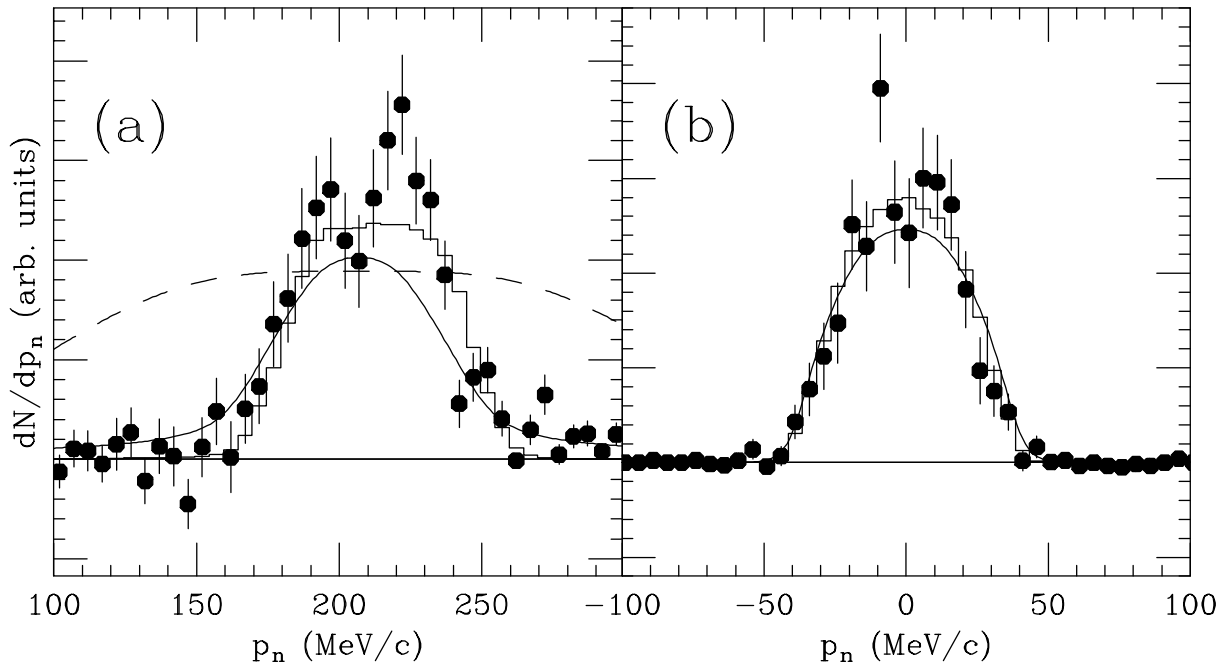
Figure 3.8: (a) Longitudinal and (b) transverse components of neutron momentum distributions in coincidence with the ^{6}He fragment for the Al target. Histograms show results of the Monte Carlo simulation described in the previous section. Dashed and solid curves show results of the model calculation (COSMA) with and without a correction of the final state interaction (FSI) of the ^{7}He resonance, respectively.

into account, a Monte Carlo simulation was performed. The Monte Carlo simulation code assuming the sequential decay mechanism is the same as used in the previous section. As mentioned previously, the simulation includes all contributions of experimental conditions. Thus, calculated distributions can be directly compared with those obtained from the experimental data. The calculated distributions are shown by the histograms in Fig. 3.8 and are in good agreement with the experimental data. As a result of the simulation, the momentum distributions can be well reproduced with the assumption of the sequential decay mechanism.

Recently, a simple five-body cluster orbital shell model approximation (COSMA) has been proposed[34, 35] and extended to the ^{8}He case in order to describe the ^{8}He ground state wave function[36, 37, 38]. The model calculations have been used for the recent experimental data[22, 36, 37, 38] and were found to reproduce the measured momentum distributions well by considering the sequential decay mechanism.

According to the COSMA, the ground state wave function of ^{8}He is obtained in a five-body (α+4n) approach and each valence neutron is assumed to occupy the $1p_{3/2}$ state relative to the α core. Thus, the ground state wave function of ^{8}He is expressed with the Slater determinant constructed with the single-particle wave functions ψ_i(k) (i=1,...,4) as

$$\psi_i(k) \equiv \psi_i(\mathbf{r}_k, \sigma_k) = \varphi(r_k) \sum_{m_i, \nu_i} C_{\frac{3}{2}\frac{3}{2}+1-i}^{1m_i\frac{1}{2}\nu_i} Y_{1m_i}(\mathbf{r}_k) \chi_{\nu_i}(k) \tag{3.8}$$

$$\varphi(r) = \sqrt{\frac{8}{3\sqrt{\pi}r_0{}^3}} \frac{r}{r_0} \exp\left(-\frac{r^2}{2r_0{}^2}\right) \tag{3.9}$$

where χ_{ν_i}, $\nu_i = \pm\frac{1}{2}$ are the spin wave function and $\varphi(r)$ is the standard 1p radial oscillator wave function with the parameter r_0. The parameter r_0=2.2 fm was calculated according to the experimental matter r.m.s. radius of ^{8}He (R=2.52 fm[33]) and was fixed in the following calculations, so that there was no free parameter, except for vertical scale factor, in fitting with the experimental distributions.

Assuming the Serber model, or the sudden approximation, the momentum distribution of neutrons corresponds to the Fourier transform of the COSMA wave function. For neutrons, the momentum distribution is calculated as

$$I_{Serber}(\mathrm{p_n}) = \frac{d\sigma}{d\mathrm{p_n}} \propto \frac{2}{3\pi^{\frac{3}{2}}\mathrm{p_0}{}^5}\mathrm{p_n}{}^2 \exp\left(-\frac{\mathrm{p_n}{}^2}{\mathrm{p_0}{}^2}\right) \tag{3.10}$$

where $\mathrm{p_n}$ is c.m. momentum of neutrons and $\mathrm{p_0}=\hbar/r_0$. Thus, the longitudinal component of the distribution is obtained by integrating over unobserved variables as

$$\frac{d\sigma}{d\mathrm{p_{nz}}} = \int I_{Serber}(\mathrm{p_n})d\mathrm{p_x}d\mathrm{p_y} \propto \frac{2}{3\pi^{\frac{1}{2}}\mathrm{p_0}}\left(1 + \frac{\mathrm{p_{nz}}{}^2}{\mathrm{p_0}{}^2}\right)\exp\left(-\frac{\mathrm{p_{nz}}{}^2}{\mathrm{p_0}{}^2}\right) \tag{3.11}$$

This distribution function is shown by the dashed curve in Fig. 3.8(a). As shown in the figure, the calculated distribution is considerably wider than the experimental distribution.

As discussed in the previous section, the relative energy distributions of the ^{6}He+n system are found to be well described with the simulation assuming the sequential decay mechanism. In this scheme, the neutron momentum distribution would be affected by a final state interaction (FSI) of the ^{7}He resonance, *i.e.*, ^{7}He decay into ^{6}He+n. Thus, the

Quantity	^{27}Al	^{120}Sn	^{208}Pb
$\sigma_\perp$	20.9 ± 1.5	17.3 ± 1.0	23.3 ± 1.9
$\sigma_\parallel$	21.5 ± 2.0	29.8 ± 2.8	28.5 ± 1.9

Table 3.3: The width parameters extracted from the transverse component($\sigma_\perp$) and the longitudinal component($\sigma_\parallel$) of neutron momentum distributions from the reaction ^{8}He+target$\rightarrow$^{6}He+n+X.

neutron momentum distribution can be expressed with a product of the ^{7}He motion and the FSI. To describe the ^{7}He motion, the COSMA wave function Eq. 3.10 is employed. A Breit-Wigner type function Eq. 3.7, used in the Monte Carlo simulation in the previous section, is employed to describe the FSI. Hence, the neutron momentum distribution considering the FSI of the ^{7}He resonance is expressed as

$$\left(\frac{d\sigma}{d\mathbf{p}_n}\right)_{FSI} \propto \int I_{Serber}(7\mathbf{p}')I_{BW}(\mathbf{p}'')\delta(\mathbf{p}' + \mathbf{p}'' - \mathbf{p}_n)d\mathbf{p}'d\mathbf{p}'' \qquad (3.12)$$

with

$$\mathbf{p}_r = -7\mathbf{p}' \qquad (3.13)$$

where $\mathbf{p}_r$ and $\mathbf{p}''$ are the momentum of the neutron removed by the target nucleus and the neutron in the ^{7}He rest frame, respectively. To compare with the experimental distribution for the transverse component, Eq. 3.12 needs to be integrated over unobserved variables and also to be corrected for the limited acceptance of the detector system. The effective acceptance of the transverse component is also estimated by the Monte Carlo simulation and is shown in Fig. 3.9. As a result of the simulation, it was found that the curve is constant up to $|\mathbf{p}_n|$ $\sim$25 MeV/c and reaches zero at $|\mathbf{p}_n|$ $\sim$60 MeV/c. On the other hand, the acceptance curve for the longitudinal component was almost constant over the measured momentum region. The calculated momentum distributions with the correction are shown by solid curves in Fig. 3.8. With the correction, the calculated curves are in good agreement with the experimental distributions.

Consequently, the distributions were well reproduced by assuming the sequential decay mechanism. This indicates that the distributions were strongly affected by the FSI of the
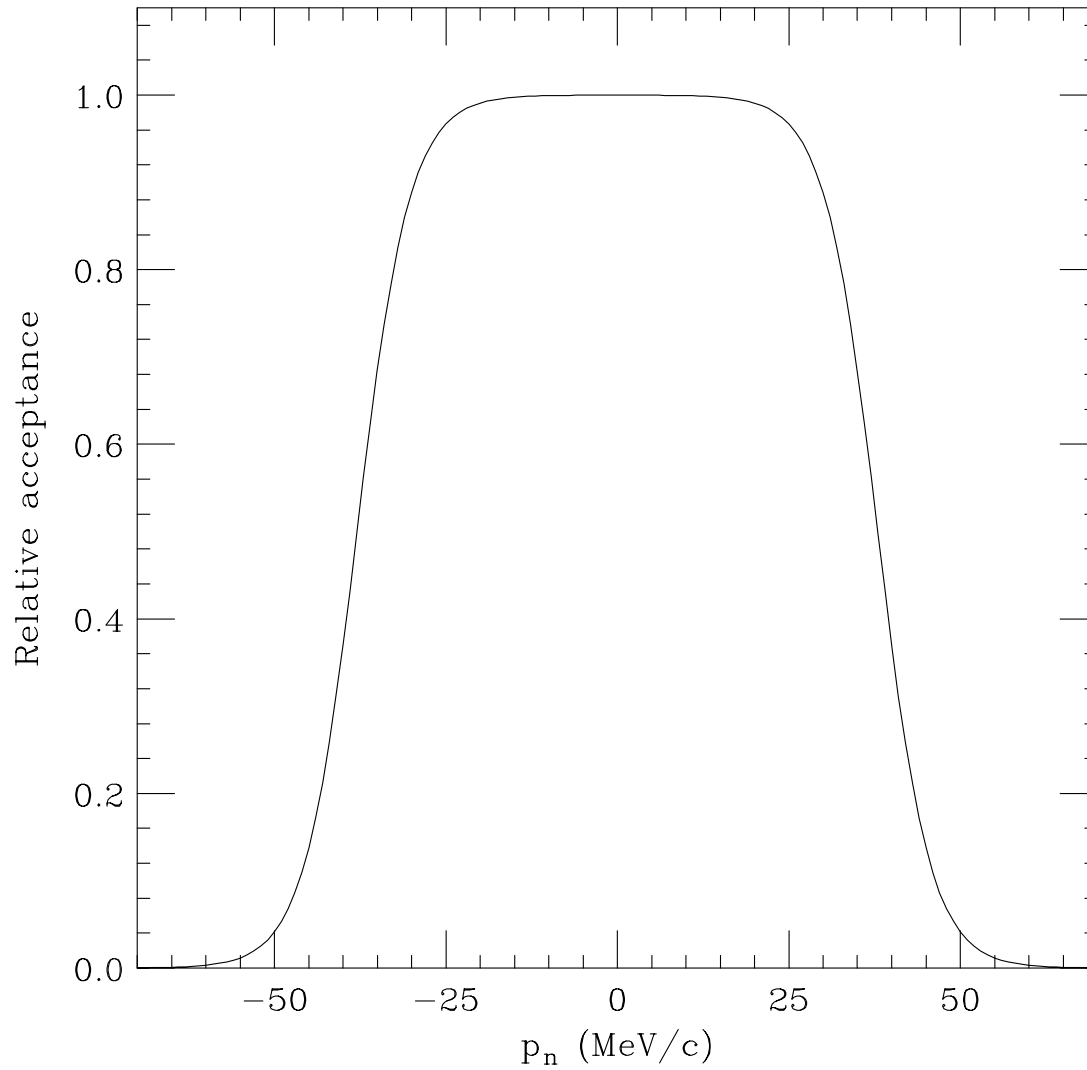
Figure 3.9: Acceptance curve for transverse component of neutron momentum distributions. The curve is obtained by the Monte Carlo simulation.
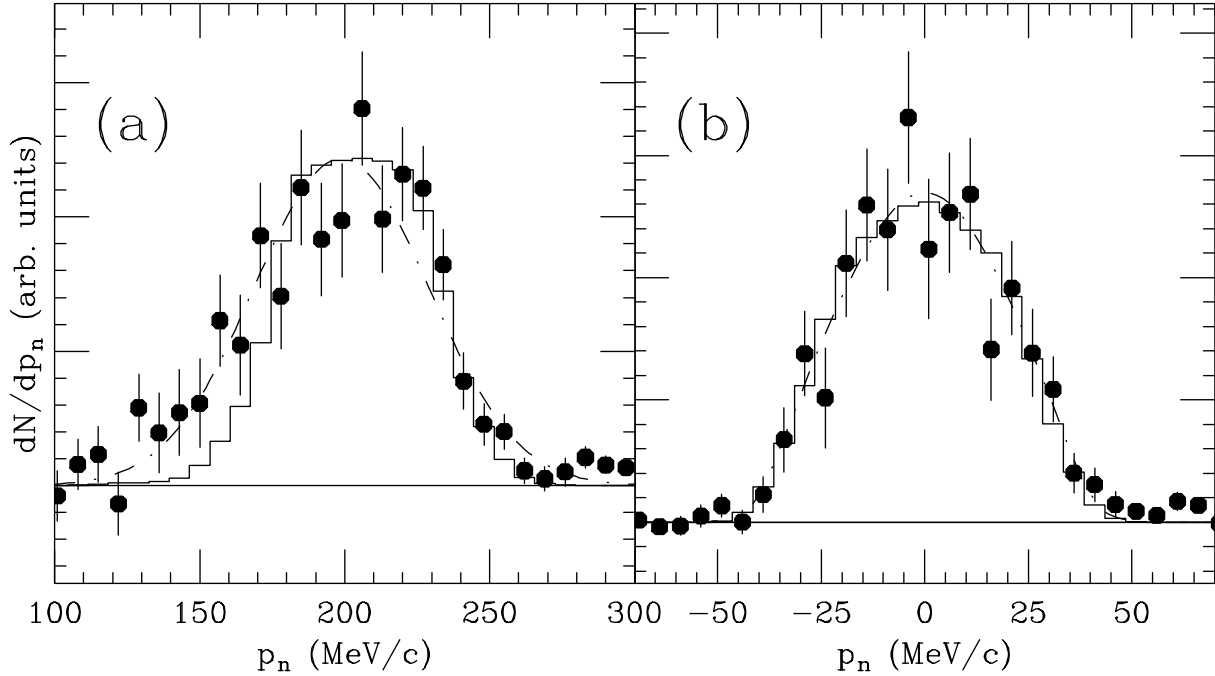
Figure 3.10: (a) Longitudinal and (b) transverse component of neutron momentum distributions for the Pb target. Histograms show results of the Monte Carlo simulation assuming the 60 % direct decay process via the $E1$ Coulomb excitation with 40 % admixture of the sequential decay process. Dot-dashed curves show a fit with gaussian distributions.

^{7}He resonance and lose information on the ground state wave function of ^{8}He. Thus, it can be concluded that a dominant reaction mechanism in the ^{8}He dissociation is attributed to the sequential process.

In contrast to the momentum distributions for the Al target, the distributions for the Pb target are rather wide, as shown in Fig. 3.10. To compare the width quantitatively, the distributions were fitted with gaussian distributions. Since the acceptance curve for the transverse component is not flat, as shown in Fig. 3.9, the gaussian distribution needs to be corrected with the acceptance curve as

$$\frac{dN}{dp_n} \propto \exp(-\frac{p_n^2}{\sigma^2})\epsilon(p_n) \tag{3.14}$$

where $\epsilon(p_n)$ represents the acceptance as a function of the transverse component of the neutron momentum p_n. On the other hand, the longitudinal components are free from

the correction. In the correction, contributions of beam spread, target thickness and detector resolution had to be taken into account to extract the intrinsic width. Since the contribution of the target thickness (Δp/p$\sim$3.8 %) is rather larger than the beam spread (Δp/p$\sim$1 %) and the detector resolution (Δp/p$\sim$1.5 %), a fit was made only with a correction for the target thickness. The width parameters σ of the gaussian distributions extracted from three targets are summarized in Table 3.3 and also plotted in Fig. 3.11. As a result, the width parameters obtained for the Al target are in good agreement with those of the recent measurement σ=20.5$\pm$1.5 MeV/c[22]. For the Sn and Pb targets, the extracted width parameters for the longitudinal component are larger than those extracted for the transverse component.

Furthermore, the momentum distributions for the Pb target are calculated with a Monte Carlo simulation. The simulation assumes a 60 % direct decay process via $E1$ Coulomb excitation with a 40 % admixture of the sequential decay process as described in the previous section. Since the simulations and the data in the Fig. 3.10 are in agreement, it may be concluded that the wider width for the Pb target is attributed to the direct decay process.
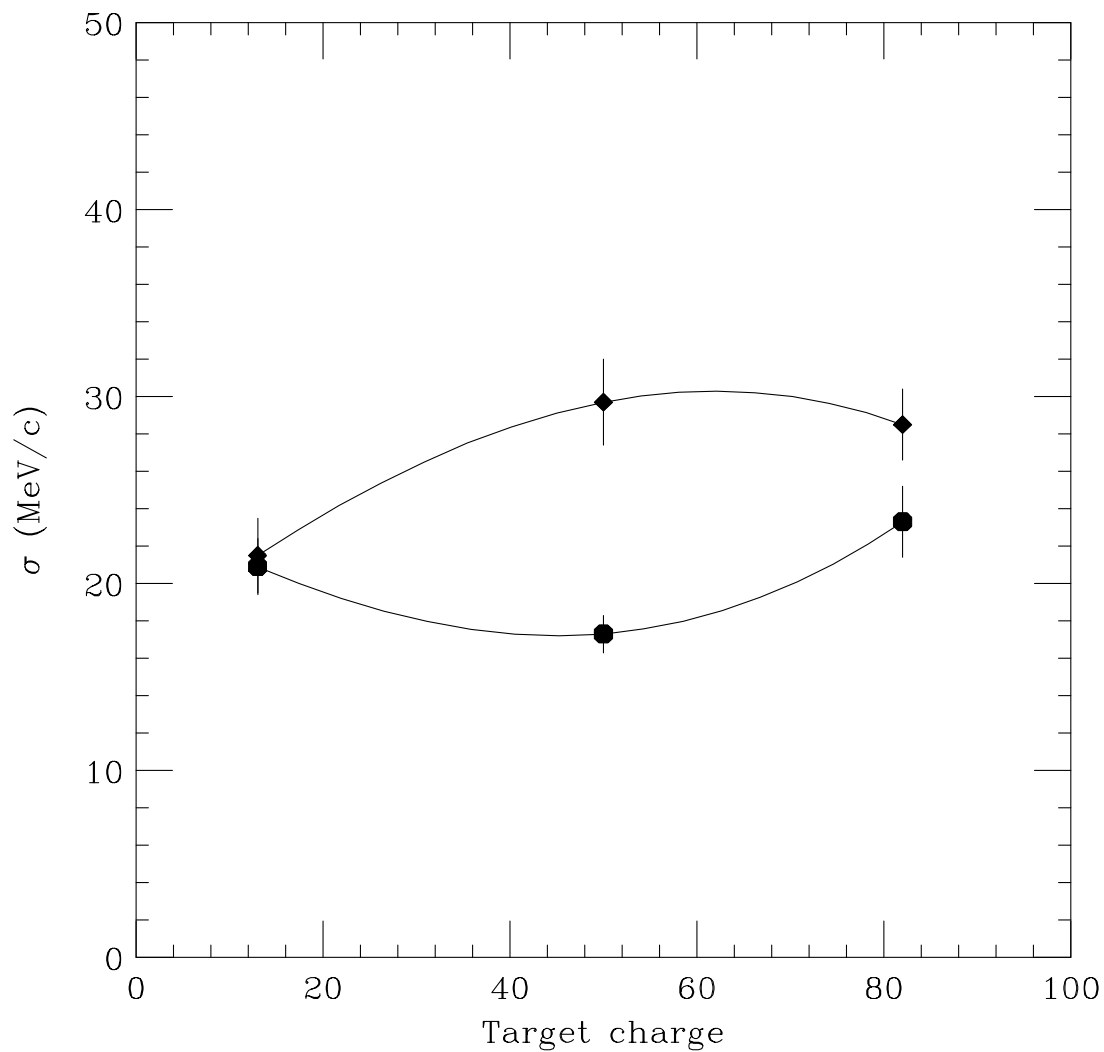
Figure 3.11: Target charge dependence of width parameter σ of the gaussian fits. Filled circles and diamonds show the width parameters extracted from transverse and longitudinal components of the neutron momentum distributions, respectively.

3.4 ^{6}He+2n coincidence data

This section describes results of the analysis of the ^{6}He+2n coincidence data. In section 3.4.1, momentum distributions of ^{6}He and neutrons are reconstructed in the ^{8}He rest frame and fitted with gaussian distributions. The obtained width parameters of the gaussian distributions are compared with those extracted from the ^{6}He+n+X data described in section 3.3.2. Finally, the decay energy distributions of the ^{8}He are reconstructed and compared with several model calculations in section 3.4.2.

One difficulty in measurements of two neutrons in coincidence is to identify neutron cross-talk events from real two-neutron events. Neutron cross-talk occurs when one neutron is detected in two different detectors, which looks like two neutrons are detected in coincidence. Thus, these events distort the coincidence measurements of two neutrons and need to be rejected.

Previously, the cross-talk in the *Neutron Wall Array* was studied using neutrons with energies of about 25 MeV from the ^{7}Li(p,n)^{7}Be reaction, and most of the cross-talk events were found to be rejectable[39]. In the following analysis, a similar scheme to reject the cross-talk events is used. A brief review of the cross-talk rejections is presented in Appendix B. Note that the cross-talk rejections are applied for all distributions in this section.

3.4.1   Momentum distributions in the ^{8}He rest frame

In section 3.3.2, the neutron momentum distributions extracted from the ^{6}He+n+X coincidence data of the Al target was found to be strongly affected by the FSI of the ^{7}He resonance. These momentum distributions have important information on the nuclear size and the decay mechanism. To clarify the detailed structure, the distributions need to be measured in the ^{8}He rest frame. However, all of the recent measurements were performed inclusively[3, 22] and no data of exclusive measurements such as in the ^{11}Li case[8, 9, 10] are available so far.

With the kinematically complete measurements, the momentum distributions can be

reconstructed in the rest frame of ^{8}He. Momentum vectors of ^{6}He and two neutrons $\mathbf{p}_i^c$ ($i = 1, 2, 3$) in the ^{8}He rest frame are determined by the Lorentz transformation expressed as

$$\mathrm{p}_{i\parallel}^c = \gamma(\mathrm{p}_{i\parallel} - \beta E_i/c)$$
$$\mathbf{p}_{i\perp}^c = \mathbf{p}_{i\perp}$$

where $\mathbf{p}_i$ is the momentum of relevant particle in the laboratory frame, and parallel and perpendicular signs refer to components relative to the velocity of the ^{8}He rest frame v=cβ. The momentum distributions of neutrons and ^{6}He for the three targets are provided in Fig. 3.12. To extract width parameters, the distributions are fitted with the gaussian distribution integrated over solid angle expressed as

$$\frac{dN}{d\mathrm{p}_i} \propto \mathrm{p}_i{}^2 \exp(-\frac{\mathrm{p}_i{}^2}{\sigma_i}) \cdot \epsilon_i(\mathrm{p}_i) \qquad (3.15)$$

where $\epsilon_i(\mathrm{p}_i)$ is a detector acceptance as a function of the momentum for ^{6}He (i=6) or neutron (i=n). The detector acceptance is estimated with a Monte Carlo simulation. In the simulation, a simple model assuming the sequential decay mechanism is used to describe the ^{8}He dissociation. A detailed description of the Monte Carlo simulation is found in section 3.4.2. The acceptance is defined as the ratio of the number of decay particles recorded in the detector system to the total number of events. The calculated acceptance curves as functions of neutron and ^{6}He momenta in the ^{8}He rest frame are shown in Fig. 3.13 by the solid and dashed curves, respectively.

With the acceptance curves, the experimental distributions are fitted with the gaussian distribution (Eq. 3.18) as shown by solid curves in Fig. 3.12. The obtained width parameters of the gaussian distributions are summarized in Table 3.4 and plotted in Fig. 3.14. The neutron width parameters are comparable to those extracted from the ^{6}He+n+X coincidence data within the error bars. Furthermore, the width of the ^{6}He momentum distribution for the Al target is in good agreement with the recent measurement σ_6=56±3
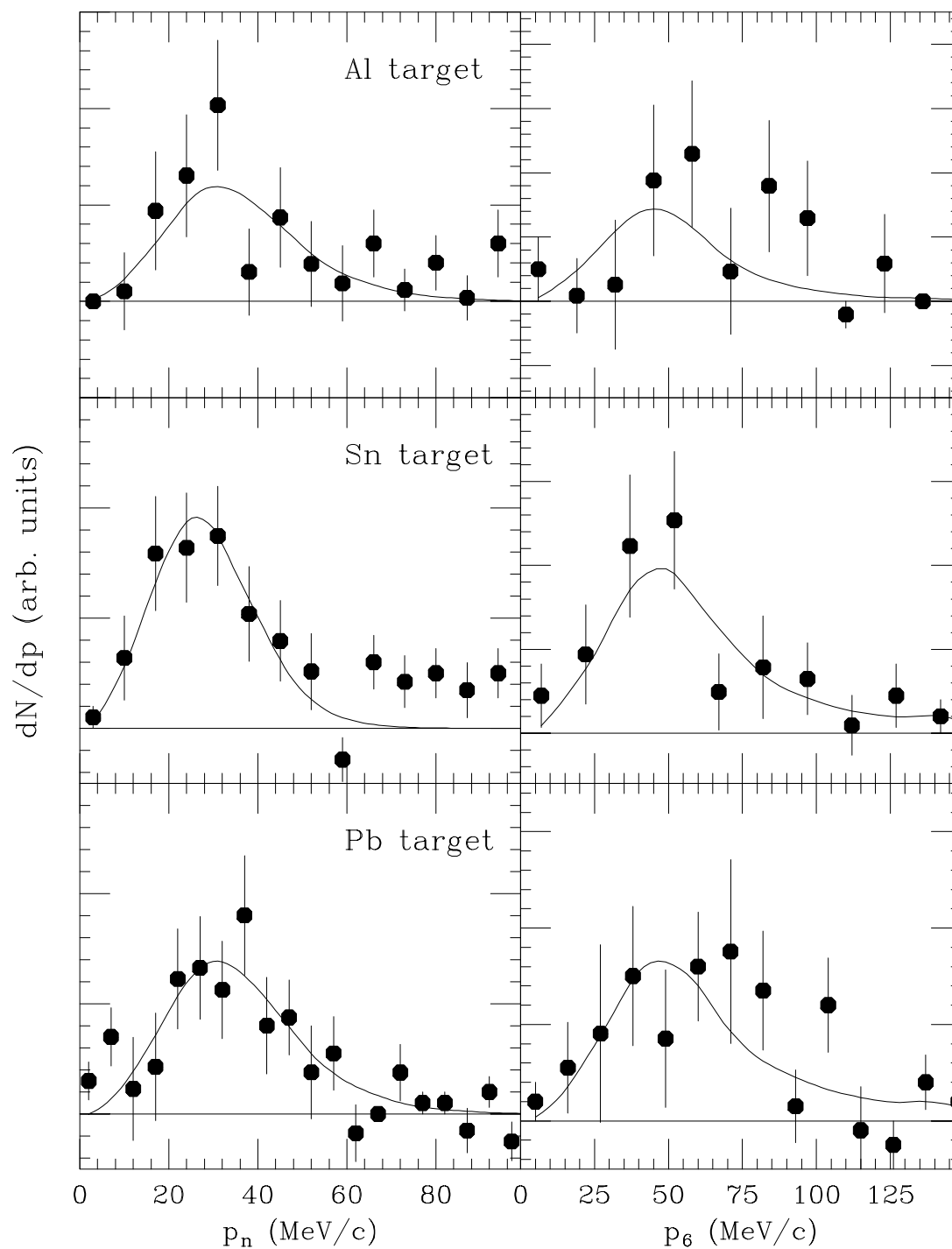
Figure 3.12: Momentum distributions of neutrons and ^{6}He in the ^{8}He rest frame. The distributions for the Al, the Sn and the Pb targets are shown in upper, middle and lowest row, respectively. Solid curves show results of gaussian fits considering the detector acceptance.
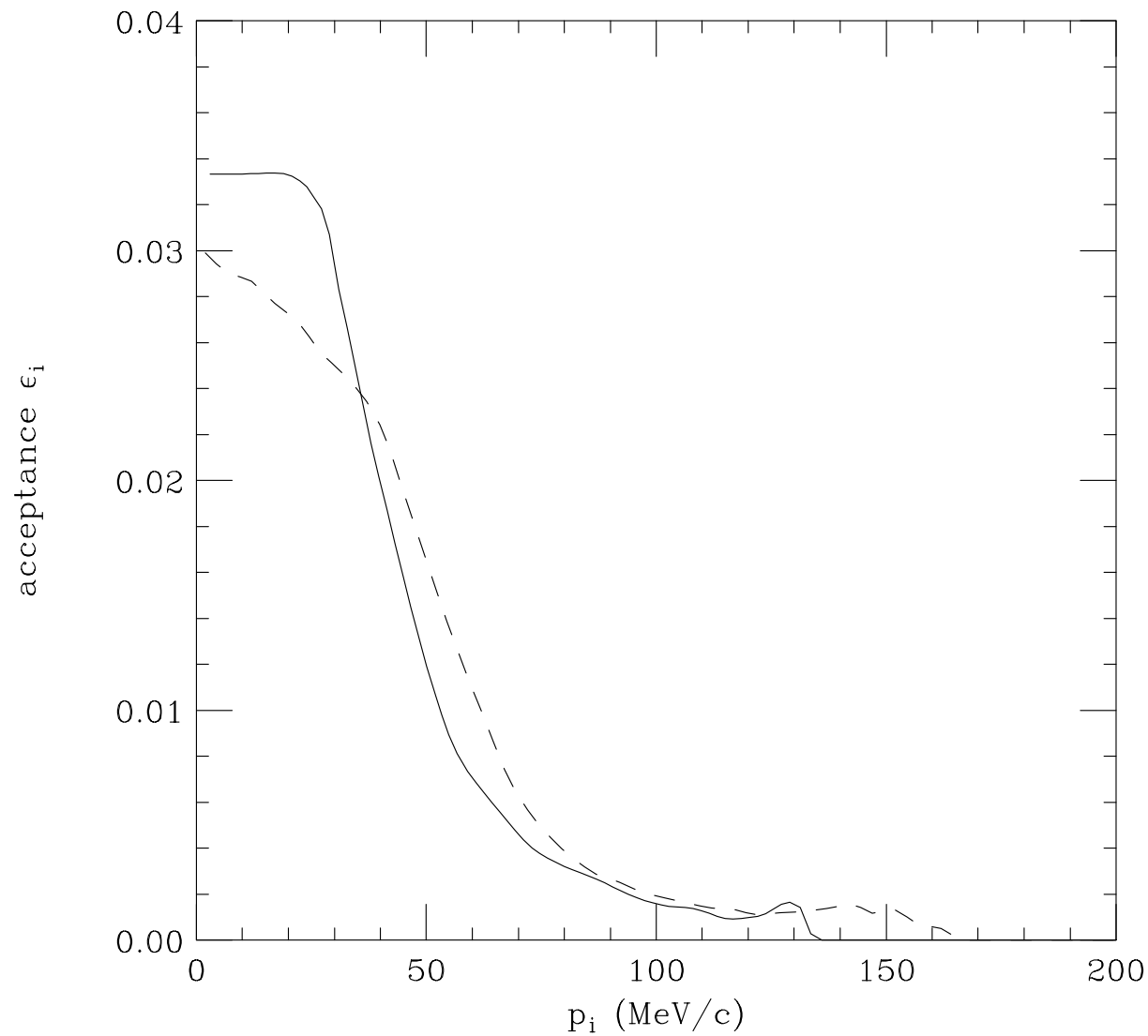
Figure 3.13: Acceptance curves of the detector system as functions of momentum of neutron (solid curve) and ^{6}He (dashed curve) in the ^{8}He rest frame. The curves are calculated with the Monte Carlo simulation.

Quantity	^{27}Al	^{120}Sn	^{208}Pb
σ_{n}	30.5±9.9 MeV/c	21.1±2.8 MeV/c	29.8±4.3 MeV/c
σ_6	53.2±14.0 MeV/c	66.6±17.4 MeV/c	70.8±15.1 MeV/c

Table 3.4: Width parameters of the gaussian fit for neutron (σ_{n}) and ^{6}He (σ_{n}) from the reaction ^{8}He+target→^{6}He+2n+target.

MeV/c[22]. They have measured the transverse momentum distribution of ^{6}He from the projectile fragmentation of ^{8}He at 240 MeV/A. On the other hand, a similar measurement of the projectile fragmentation at 800 MeV/A shows even wider width σ_6=77±5 MeV/c[3]. A similar beam energy dependence of the momentum width has also been observed in measurements of ^{11}Li fragmentation[40].
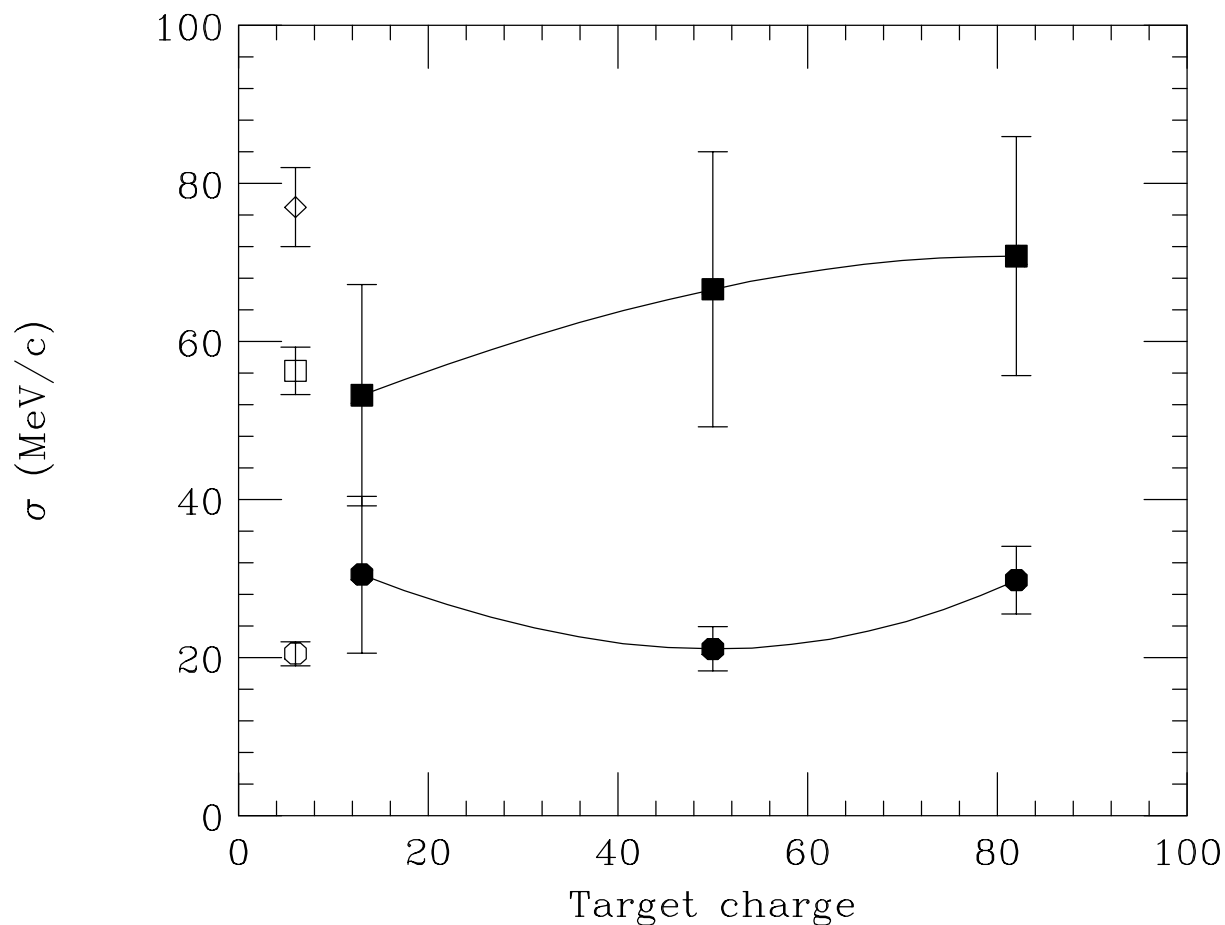
Figure 3.14: The target charge dependence of width parameter σ of the gaussian fits for neutron (filled circles) and ^{6}He (filled squares) momentum distributions. An open circle and an open square show the parameters for neutron and ^{6}He taken from Ref.[24]. A diamond shows the parameter for ^{6}He taken from Ref.[3].

3.4.2 Decay energy distributions

By measuring all decay products from the dissociation of ^{8}He, an excitation energy can be reconstructed. The excitation energy E_x is related to the decay energy E_d given by

$$E_x \;=\; E_d + S_{-2\mathrm{n}} \tag{3.16}$$

$$E_d \;=\; \sqrt{\sum_i \varepsilon_i^2 - \sum_i \mathbf{p}_i^2} - \sum_i M_i c^2 \tag{3.17}$$

where ε_i, $\mathbf{p}_i$ and M_i $(i = 1, 2, 3)$ are the total energy, the momentum and the rest mass of two neutrons and ^{6}He and $S_{-2\mathrm{n}}$ is a separation energy of two neutrons. The measured decay energy distributions dN/dE_d for the Al and the Sn targets are reconstructed and provided in Fig. 3.15. As shown in the figures, a prominent peak corresponding to the first excited state of ^{8}He (E_x=3.57 MeV, Γ=0.50 MeV and J^π=2$^+$[13]) is observed for the distributions. As discussed in section 3.2, the dominant reaction channel in the ^{8}He dissociation was found to be the one-neutron-removal process (path (a) in Fig. 3.5) in particular for lighter target. On the other hand, the reaction channel of path (b) can be confirmed by the observed peak in the distributions.

The decay energy distribution for the Pb target was also reconstructed and is shown in Fig. 3.16. In contrast to those of the Al and the Sn targets, the distribution has a rather broad structure. To describe the decay energy distribution, simple model calculations were performed as follows. To take all restrictions of the experimental conditions into account, the model calculations were made with Monte Carlo simulations. As discussed in section 3.2, it was found that the ^{8}He dissociation for the Pb target is dominated by the Coulomb component from the target charge dependence of the neutron removal cross section. Therefore, the simulation assumes that the dissociation of ^{8}He proceeds via its first excited state by $E2$ Coulomb excitation and decays into ^{7}He+n (path (b) and (d) in Fig. 3.5).

The Coulomb dissociation cross section $d\sigma_c/dE_x$ is related to the photonuclear cross section σ_{E2} by

$$\frac{d\sigma_c}{dE_x} = n_{E2}(E_x)\frac{\sigma_{E2}}{E_x} \tag{3.18}$$
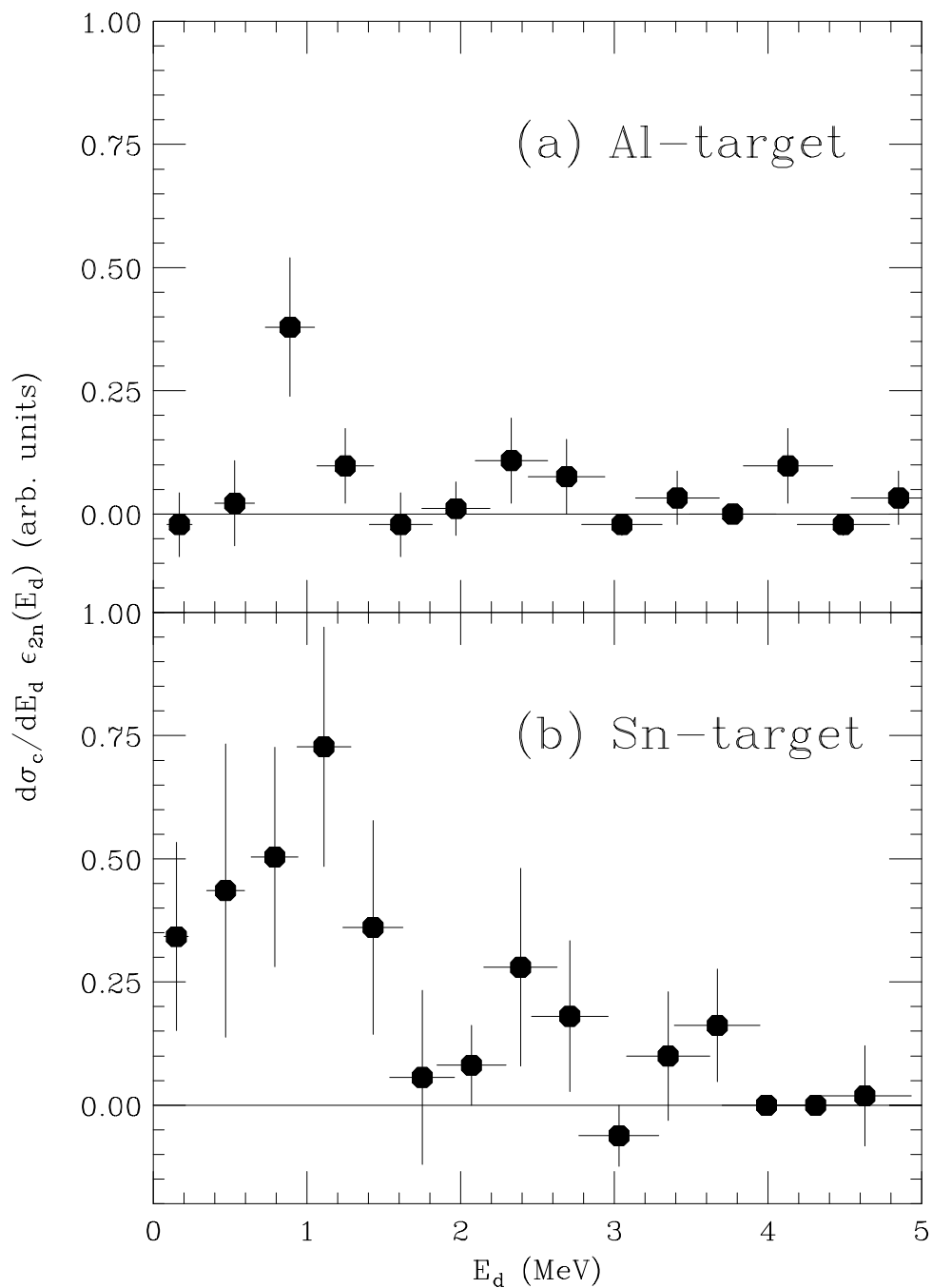
Figure 3.15: Measured decay energy distributions for (a) the Al target and (b) the Sn target. The function $\epsilon_{2n}(E_d)$ refers to an acceptance to detect two neutrons in coincidence as a function of the decay energy E_d. A prominent peak $E_d \sim 1$ MeV corresponding to the first excited state of ^{8}He is observed in both distributions.
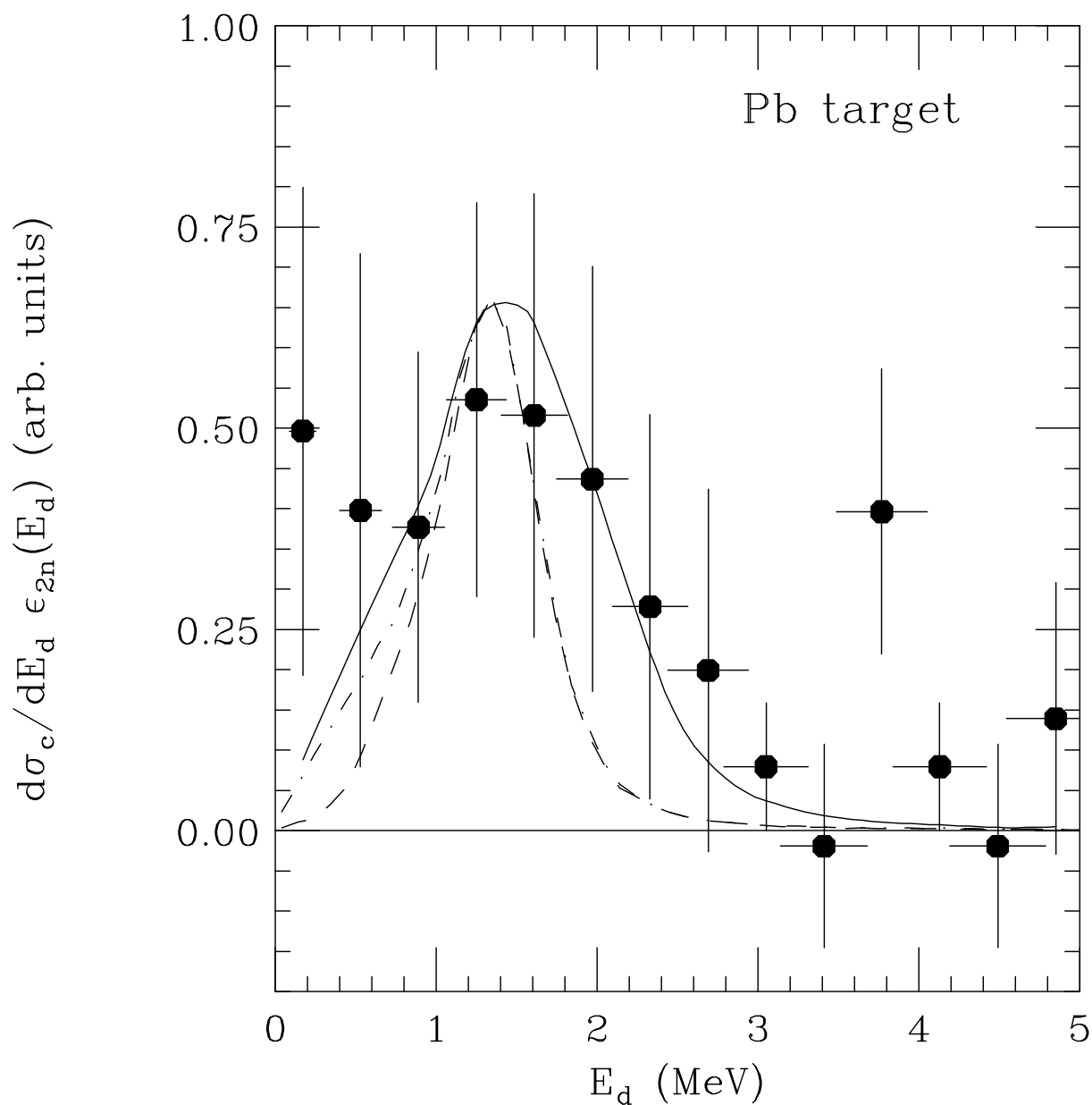
Figure 3.16: Measured decay energy distribution for the Pb target. The function $\epsilon_{2n}(E_d)$ refers to an acceptance to detect two neutrons in coincidence as a function of the decay energy E_d. The solid curve shows a good fit of the calculated distribution to the experimental data obtained by varying parameters of the Breit-Wigner function. The dashed and the dot-dashed curves show results assuming the sequential and the phase-space decay models via the first excited state of ^{8}He.

Here, the function $n_{E2}(E_x)$ is the virtual photon numbers for an electric multipole $\lambda=2$. An analytical form of the function at relativistic projectile energies is given in an approximate expression[41]. Since the difference from the exact calculation is almost negligible for the present beam energy, the function is calculated with the relativistic expression written as

$$n_{E2}(E_x) = \int \frac{Z_T^2 \alpha}{4\pi^2} \left(\frac{c}{v}\right)^4 \varepsilon^2 e^{-\pi\eta} \left\{ \frac{4}{\gamma^2} [K_1^2 + xK_0K_1 + x^2 K_0^2] + x^2 \left(2 - \frac{v^2}{c^2}\right)^2 K_1^2 \right\} d\Omega \quad (3.19)$$

where Z_T is the target charge, α is the fine structure constant, v is the relative velocity and ε $(=1/\sin(\theta/2))$ is the eccentricity parameter. The K's are the Bessel functions of the argument $x = \varepsilon\eta = \varepsilon E_x a/\hbar\gamma v$. The calculated virtual photon numbers for the three targets are shown in Fig. 3.17. Note that the shapes of the curves are identical for the three targets. The photonuclear cross section σ_{E2} can be parameterized with a Breit-Wigner-type function with parameters of the resonant energy $E_0=1.46$ MeV and the width $\Gamma_0=0.50$ MeV to describe the first excited state. As the state has a configuration of $(1p_{3/2})^{-1}(1p_{1/2})^1$, the width parameter of the function has the energy dependence of the p-wave neutron owing to the centrifugal barrier as described in section 3.3.1. Since ^{7}He is particle unstable with respect to neutron emission at 0.44 MeV, ^{7}He subsequently decays into ^{6}He+n. To describe the ^{7}He decay, the Breit-Wigner type function used in section 3.3.1 is also employed. The calculated distribution for the Pb target is shown by a dashed curve in Fig. 3.16.

As an alternative model, direct decay of the excited ^{8}He into ^{6}He+2n is considered (path (c) in Fig. 3.5). In the rest frame of the excited ^{8}He, the decay energy can be expressed as

$$E_d = E_{6-nn} + E_{n-n} \quad (3.20)$$

where E_{6-nn} is the relative energy between ^{6}He and the c.m. of two neutrons, and E_{n-n} is the relative energy between the two neutrons. To describe such a decay mechanism, the decay energy is assumed to be partitioned between E_{6-nn} and E_{n-n} according to the three-body phase space distribution. Furthermore, a Monte Carlo simulation assuming
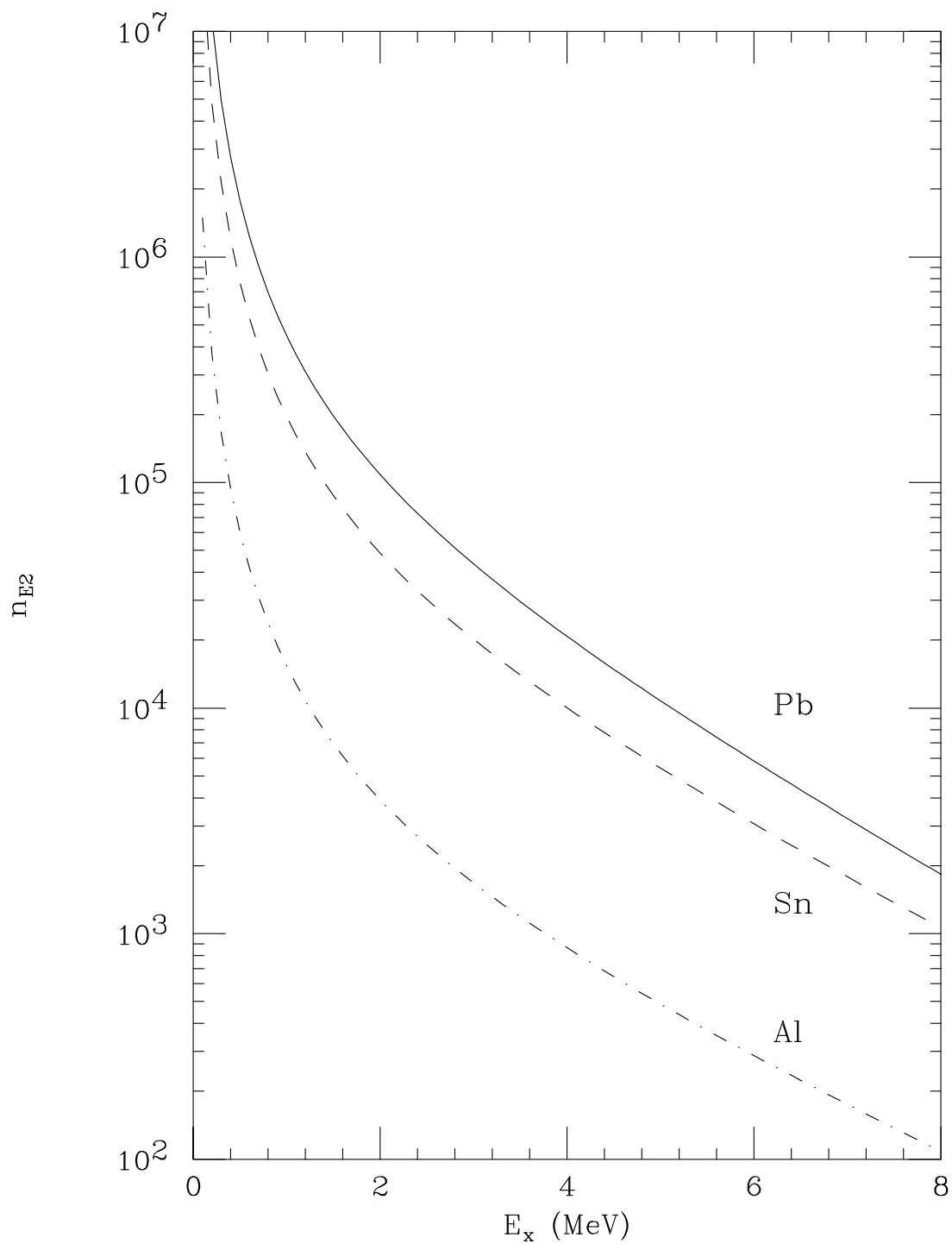
Figure 3.17: Calculated virtual photon numbers for $E2$ absorption. Solid, dashed and dot-dashed curves show results of the calculation for the Pb, the Sn and the Al targets, respectively.

the direct model was performed, and the calculated decay energy distribution is shown by the dot-dashed curve in Fig. 3.16. Regarding the decay energy distribution, the calculated distribution should be identical to that of the sequential model owing to the energy conservation law. However, the two calculated distributions are slightly different as shown in the figure owing to the different response functions of the detector system depending on the models as described in section 2.5. As seen in the figure, the broad experimental distribution are not quite reproduced with those two calculated distributions.

In several measurements of the dissociation of the halo nuclei such as ^{11}Li[8, 9, 10] or ^{11}Be[19], it is known that the $E1$ strength is much larger than the $E2$ strength. Furthermore, the $E1$ continuum state was observed in recent measurements of the breakup reactions of 240 MeV/A ^{6}He into ^{4}He+2n on a Pb target[20]. In the present analysis, it is not feasible to separate out a contribution of the $E2$ strength. Therefore, in the following analysis, to make an estimate of the $E1$ strength, we assumed that ^{8}He is excited to the $E1$ continuum state and then decays into ^{6}He and two neutrons (Fig. 3.18).

To describe the experimental distribution, the $E1$ photonuclear cross section σ_{E1} was assumed to be parameterized with the Breit-Wigner function, and Monte Carlo simulations with variation of the parameters of the function were performed. For the electric dipole, the Coulomb dissociation cross section $d\sigma_c/dE_x$ is related to the photonuclear cross section σ_{E1} by

$$\frac{d\sigma_c}{dE_x} = n_{E1}(E_x)\frac{\sigma_{E1}}{E_x} \tag{3.21}$$

The function $n_{E1}(E_x)$ represents the virtual photon numbers for the electric dipole given by[41]

$$n_{E1}(E_x) = \frac{2}{\pi}Z_T^2\alpha\eta^2 e^{-\pi\eta}\left(\frac{c}{v}\right)^2\int_{\varepsilon_0}^{\infty}\varepsilon d\varepsilon\Big\{\frac{1}{\gamma^2}\frac{\varepsilon^2-1}{\varepsilon^2}[K_{i\eta}(\varepsilon\eta)]^2 + [K'_{i\eta}(\varepsilon\eta)]^2\Big\} \tag{3.22}$$

where ε_0 is the minimum eccentricity parameter. The function $K_{i\eta}(\varepsilon\eta)$ is a modified Bessel function of imaginary order and the function $K'_{i\eta}(\varepsilon\eta)$ is the derivative of $K_{i\eta}(\varepsilon\eta)$ with respect to the argument $\varepsilon\eta$. The virtual photon numbers for three targets as functions of the excitation energy of ^{8}He are calculated and provided in Fig. 3.19.
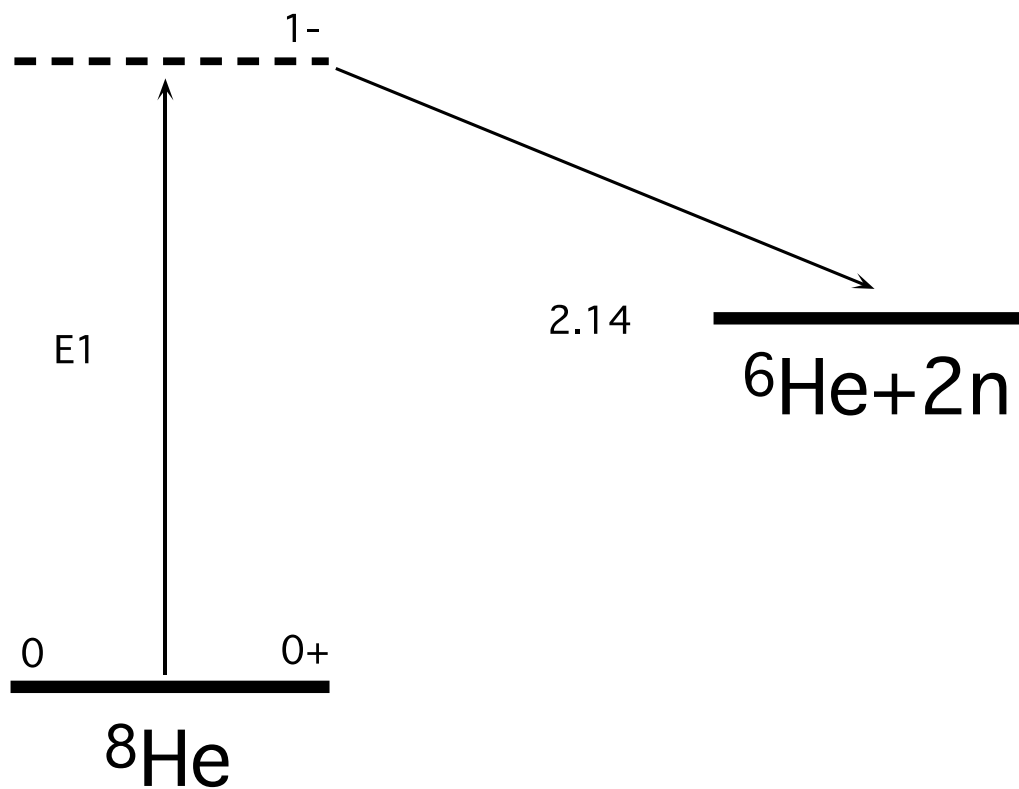
Figure 3.18: Level scheme for $E1$ excitation followed by the direct decay process. The dashed line represents a continuum state of ^{8}He via $E1$ Coulomb excitation.
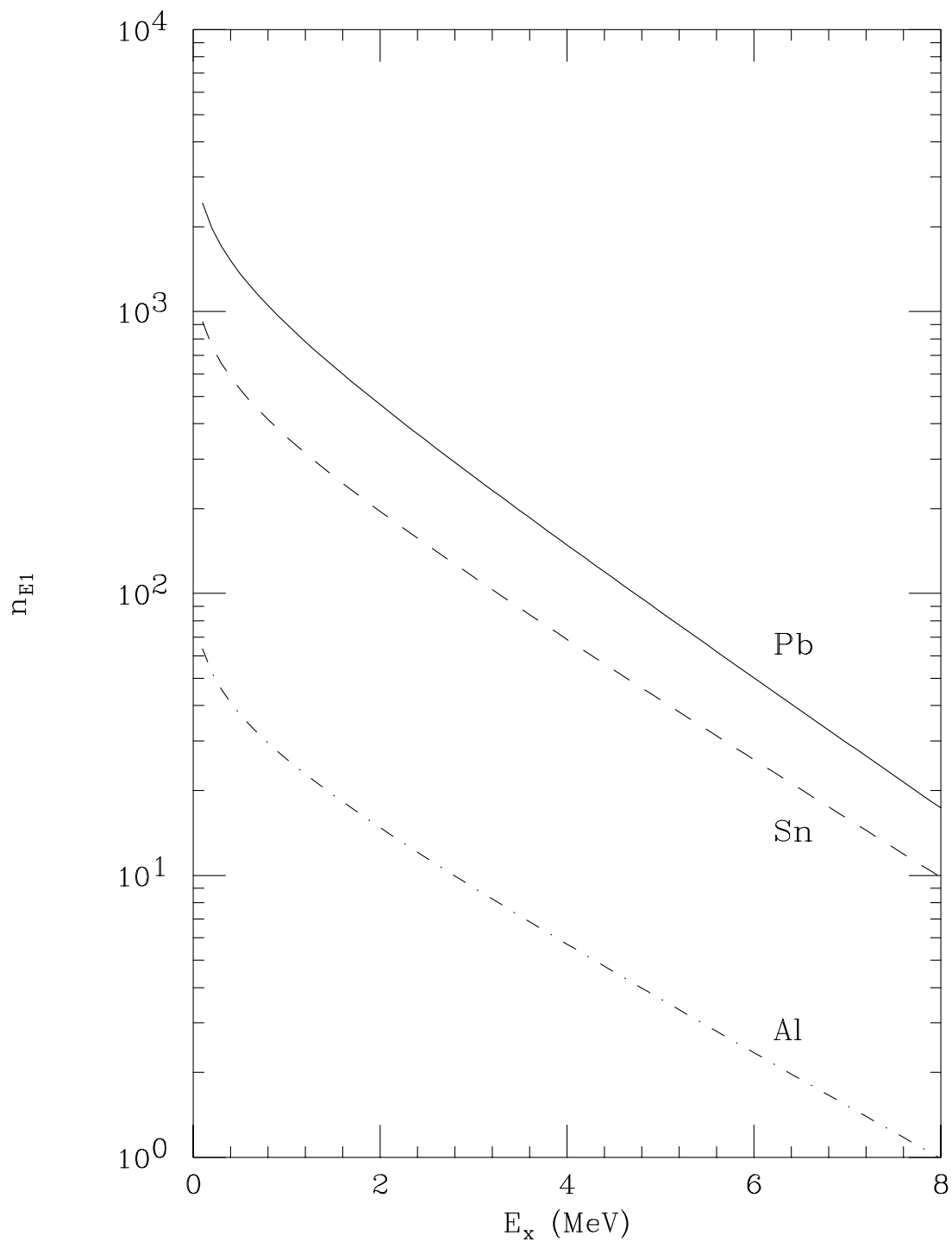
Figure 3.19: Calculated virtual photon numbers for $E1$ absorption. Solid, dashed and dot-dashed curves show results of the calculation for the Pb, the Sn and the Al targets, respectively.

As discussed in section 3.2, the dissociation cross section has the Coulomb component and the nuclear component. For the Al target, most of the ^{8}He dissociation was attributed to the nuclear component. Furthermore, with the observed peak in the decay energy distribution, it was found that the dissociation for the Al target proceeds via the first excited state of ^{8}He. Therefore, it can be concluded that the nuclear dissociation proceeds via the first excited state. To describe the first excited state, the Breit-Wigner-type function, as used previously, was employed. The strength of the nuclear component for Pb target was evaluated by the factorization of the 2n-removal cross sections as also discussed in section 3.2. This component was taken into account in the Monte Carlo simulation; the experimental distribution was fitted with those calculated assuming the Coulomb component and the nuclear component.

A good fit to the experimental distribution was obtained with the resonant parameter E_0=2.1 MeV and the width parameter Γ_0=1.0 MeV, the fit is shown by the solid curve in Fig. 3.16. Owing to the complicated response function of the detector system, it is not feasible to unfold a true decay energy distribution $d\sigma_c/dE_d$ from the measured distribution. Instead, the true distribution $d\sigma_c/dE_d$, deduced by the good fit of the calculated distribution to that observed (solid curve in Fig. 3.16), is shown in Fig. 3.20(a). Since the Coulomb dissociation cross section is related to the photonuclear cross section σ_{E1} by Eq. 3.21, the photonuclear cross section can be calculated as shown in Fig. 3.20(b). Then, the dipole strength function can be calculated with the relation

$$\frac{d\sigma_c}{dE_x} = \frac{16\pi^3}{9\hbar c}n_{E1}(E_x)\frac{dB(E1)}{dE_x} \tag{3.23}$$

and is shown in Fig. 3.20(c).

In addition to the decay energy distributions, momentum distributions of ^{6}He (p_6) and neutrons (p_n) in the ^{8}He rest frame and between two neutrons (p_{n-n}) were reconstructed and are provided in Fig. 3.21. Furthermore, the momentum distributions were calculated by the Monte Carlo simulations assuming the Breit-Wigner-type photonuclear cross section function with E_0=2.1 MeV and Γ_0=1.0 MeV described previously. The fit are shown by solid curves in the figure. In the simulation, the decay energy was assumed to be par-

Figure 3.20: (a) A true decay energy distributions $d\sigma_c/dE_d$, (b) a photonuclear cross section σ_{E1} and (c) a dipole strength function $dB(E1)/dE_d$ determined to produce a good fit to the measured decay energy distribution for the Pb target.
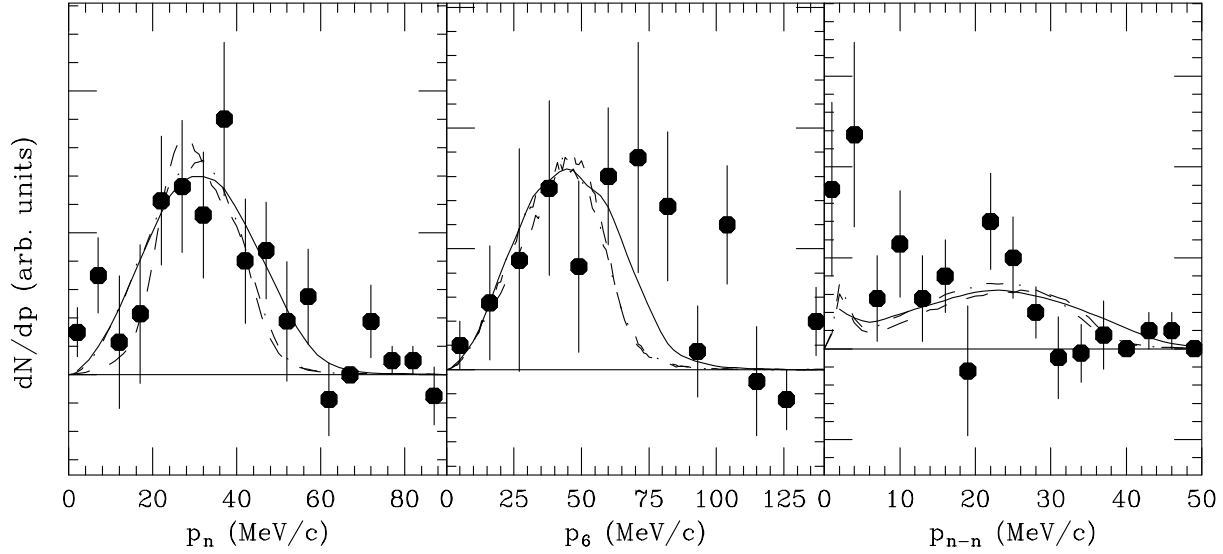
Figure 3.21: Momentum distributions of neutrons(p_n) and ^{6}He(p_6) and between two neutrons(p_{n-n}) in the rest frame of ^{8}He for the Pb target. A solid curve shows a result of the Monte Carlo simulation by parameterizing the photonuclear cross section with the Breit-Wigner function(E_0=2.1 MeV and Γ=1.0 MeV). A dashed and a dot-dashed curves show results of the Monte Carlo simulation assuming the sequential decay and the direct models via the first excited state, respectively.

titioned between ^{6}He and neutrons according to the three-body phase space distribution as described previously. We see that the overall distributions are well reproduced by the calculated curves. Moreover, simulations assuming the sequential decay model and the direct models via the first excited state were also performed. The results of these calculations are shown by dashed and dot-dashed curves in the figures, respectively. These two results are almost identical and predict somewhat narrower distributions than the measured distributions.

In summary of this section, the nuclear structure and the reaction mechanism of ^{8}He dissociation were discussed with the ^{6}He+2n coincidence data. The kinematically complete measurements allowed us to reconstruct the decay energy distributions and the momentum distributions in the ^{8}He rest frame. The observed peak in the decay energy distributions for the Al and Sn targets is roughly consistent with the energy of the first excited state of ^{8}He. On the other hand, the decay energy distribution for the Pb target

has a broader distribution than those of the Sn and the Al targets.

To describe the measured decay energy distribution for the Pb target, Monte Carlo simulations assuming simple models were performed. According to the target charge dependence of the neutron removal cross section, it was found that the dissociation of ^{8}He may be attributed to the Coulomb excitation. First, Monte Carlo simulations assuming the sequential and direct decay via the first excited state were performed. The measured broad decay energy distribution was not well reproduced by these simulations.

In several measurements of the dissociation of the halo nuclei such as ^{6}He, ^{11}Li or ^{11}Be, it is known that the $E1$ strength is much larger than the $E2$ strength. Since it is not feasible to separate the contribution of the $E2$ strength in the present analysis, we have estimated the $E1$ strength by assuming that all of the strength is attributed to that of the $E1$ excitation as a first order approximation. By assuming that the $E1$ photonuclear cross section σ_{E1} is parameterized with the Breit-Wigner function, the measured decay energy distribution dN/dE_d can be reproduced. The good fit to the measured distribution yields the parameters of the function E_0=2.1 MeV and Γ_0=1.0 MeV. With these parameters, the true decay energy distribution $d\sigma_c/dE_d$, the photonuclear cross section σ_{E1} and the dipole strength function $dB(E1)/dE_d$ were deduced for the first time.

Chapter 4

Discussions

4.1 Cluster model

The di-neutron cluster model was proposed for ^{11}Li[42], and the calculated total $E1$ strength was found to agree with the measurement[9]. The model calculation is applied to present data in the following. The model assumes the halo nucleus has a cluster-like structure, *i.e.*, a bound di-neutron system coupled to a core. According to the model, the electric dipole strength function is given as

$$\frac{dB(E1)}{dE_x} = \frac{3\hbar^2}{\pi^2\mu_{6-2\mathrm{n}}}\left(\frac{Z_6 M_{2\mathrm{n}} - Z_{2\mathrm{n}} M_6}{M_8}\right)^2 \frac{\sqrt{S_{-2\mathrm{n}}}(E_x - S_{-2\mathrm{n}})^{3/2}}{E_x^4}e^2 \qquad (4.1)$$

where Z and M are the charge and mass of the relevant particles, and $\mu_{6-2\mathrm{n}}$ is the reduced mass of the cluster system. The calculated dipole strength function is shown by a dotted curve in Fig. 4.1(c). Furthermore, the photonuclear cross section σ_{E1} and the Coulomb dissociation cross section $d\sigma_c/dE_d$ can be calculated, and the calculated results are also shown in the figure. As shown in the figure, absolute values of the dipole strength are roughly comparable to the model calculation.

In addition, the model calculation is compared with the measured decay energy distribution dN/dE_d. To take all experimental restrictions into account, the calculation is made with a Monte Carlo simulation. A result of the simulation is shown by a dotted curve in Fig. 4.2. The model predicts a peak around $E_d \sim 0.6$ MeV, which is appreciably lower than observed peak. A similar tendency has been reported for the cases of ^{11}Li [8, 9].
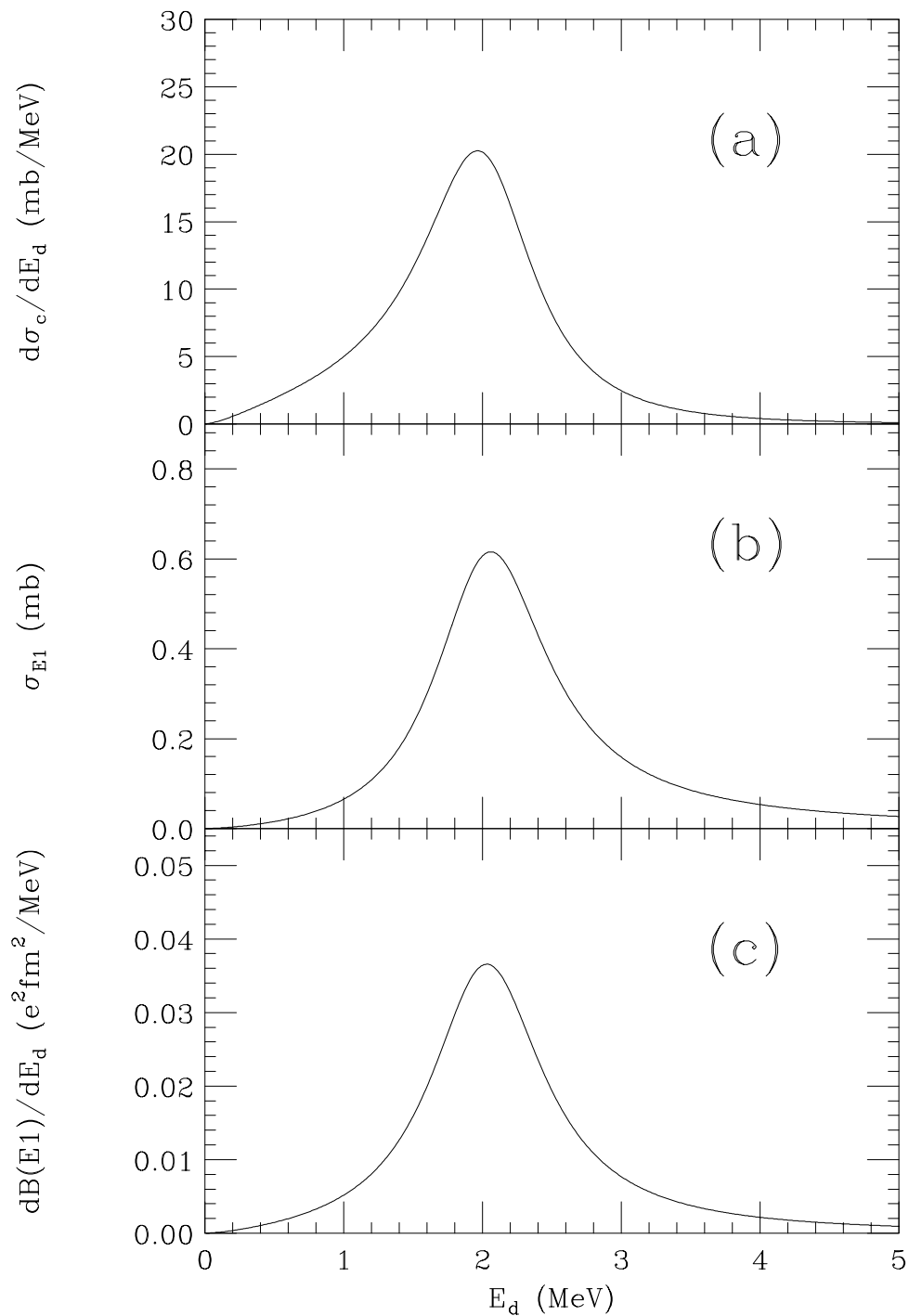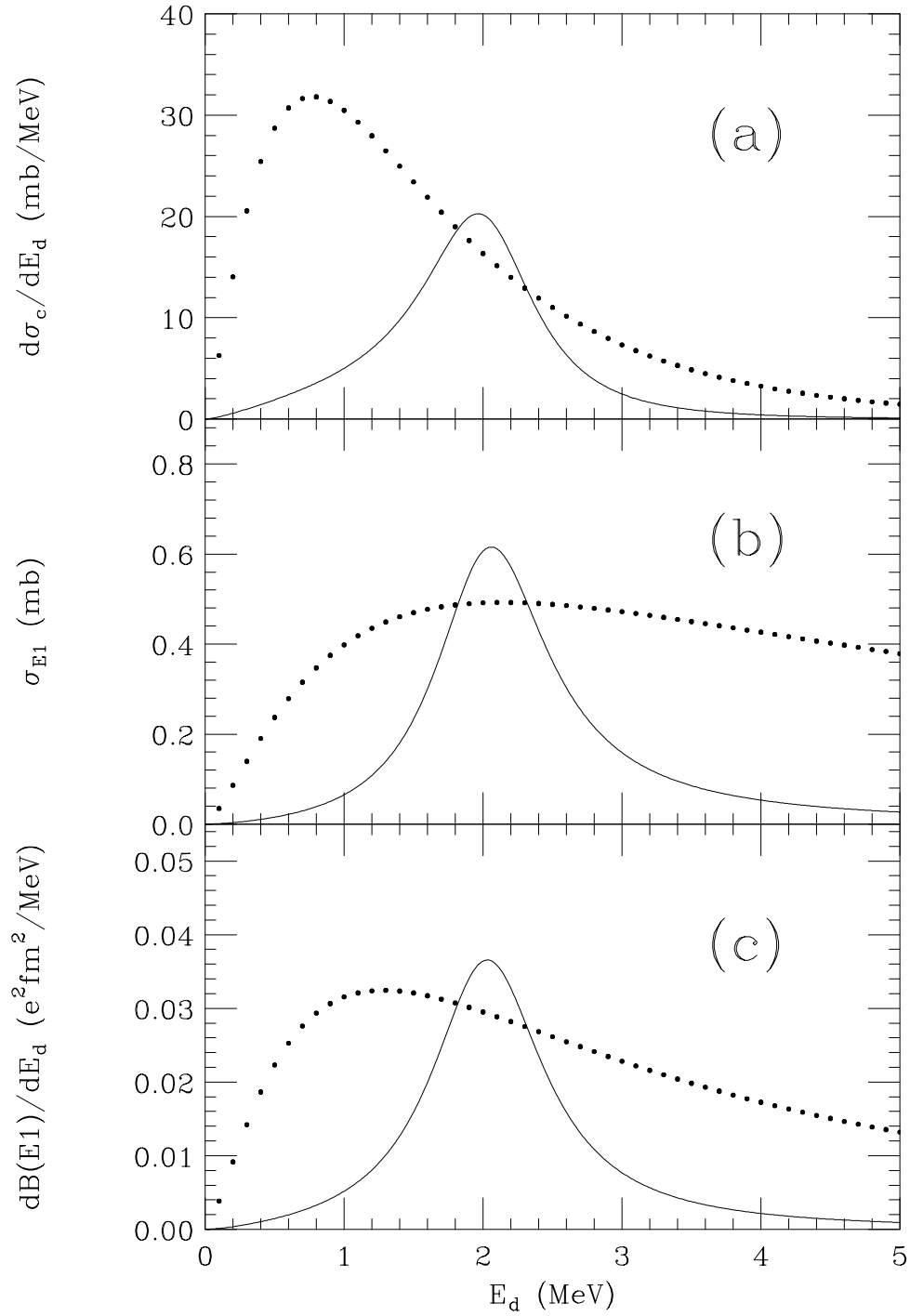
Figure 4.1: (a) A true decay energy distributions $d\sigma_c/dE_d$, (b) a photonuclear cross section σ_{E1} and (c) a dipole strength function $dB(E1)/dE_d$ determined from a fit to the measured decay energy distribution (see section.3.4.2). Dotted curves are calculated according to the cluster model.
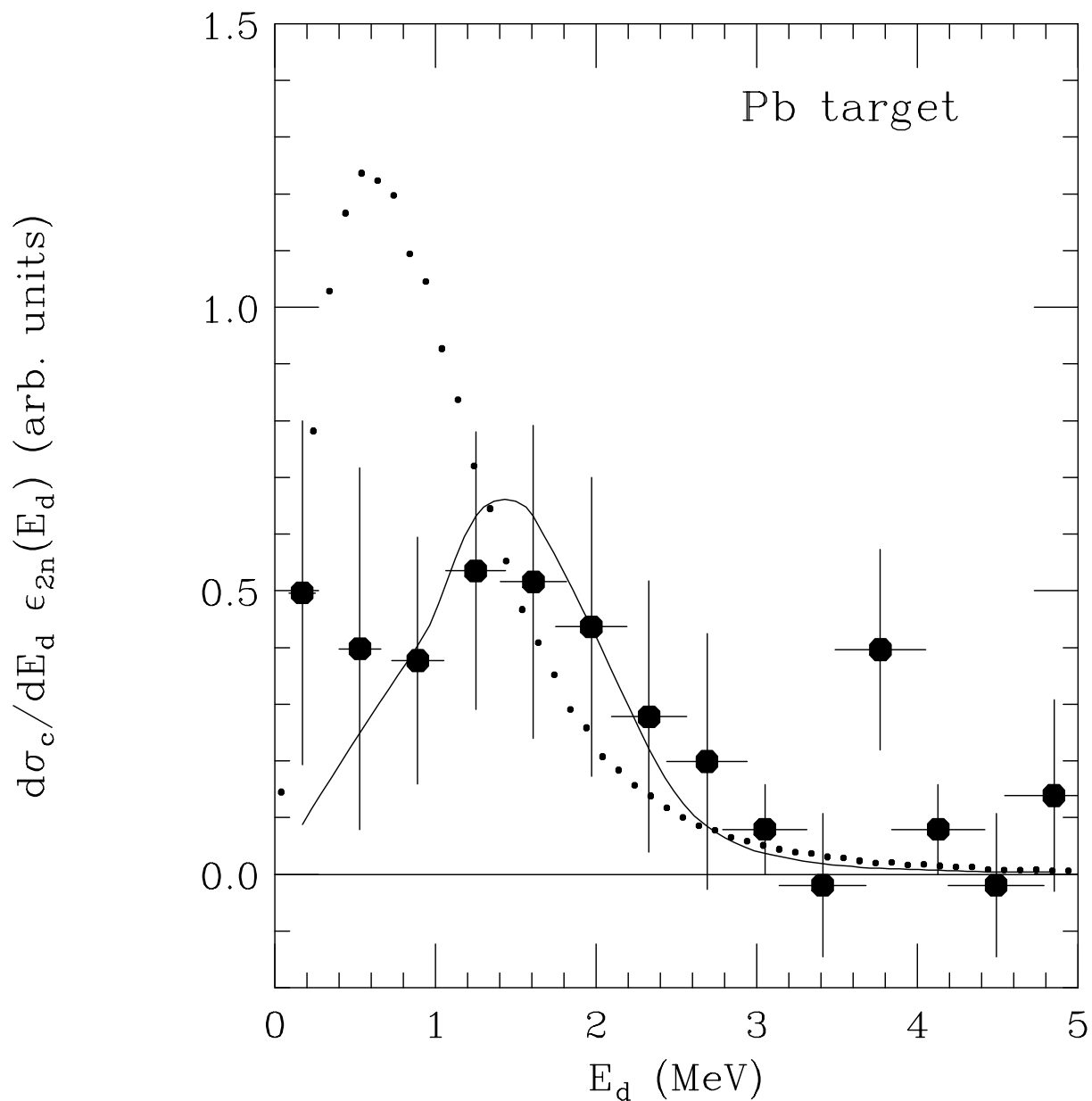
Figure 4.2: Measured decay energy distribution for the Pb target. The function $\epsilon_{2n}(E_d)$ refers to an acceptance to detect two neutrons in coincidence as a function of the decay energy E_d. The solid curve shows a good fit of the calculated distribution to the experimental data obtained by varying the parameters of the Breit-Wigner-function (see section.3.4.2). The dotted curve shows the result of a Monte Carlo simulation assuming the cluster model.

4.2   Sum rules

With the measured decay energy distribution, the dipole strength function can be derived from the relation Eq. 3.23. By integrating the function, one can obtain the integrated energy-weighted dipole strength. The function extracted from the Pb target was thus integrated, and the obtained energy-weighted dipole strength S_{exp}^{E1} is listed in Table 4.1. Owing to the limited acceptance of the detector system as described in section 2.5, the integrations were made up to E_d=3 MeV. Furthermore, the energy-weighted dipole strength can be extracted by integrating the dipole strength function deduced by the Monte Carlo simulation assuming the $E1$ direct decay as described in section 3.4.2. These integrations were also made up to E_d=3 MeV and $E_d=\infty$ MeV, and the obtained strengths S_{sim}^{E1} are listed in Table 4.1.

It is known that the total strength for a given multipolarity is limited by the sum rule. For isovector dipole transitions, the total strength can be evaluated with the Thomas-Reiche-Kuhn (TRK) sum rule as

$$S_{\mathrm{TRK}}^{E1} \quad \equiv \quad \sum_f (E_f - E_i) B(E1; i \to f) \tag{4.2}$$

$$= \quad \frac{9}{4\pi} \frac{\hbar^2}{2M} \frac{ZN}{A} e^2 \tag{4.3}$$

where i and f refer to the initial and the final states, respectively and M is the nucleon mass. The calculated sum is also listed in the table. As a result, the experimental sums S_{exp}^{E1} for $E_d \leq 3$ MeV was found to be 0.35±0.28 % of those calculated by the TRK sum rule.

With the assumption that the ^{8}He has a cluster-like structure, $i.e.$, a bound di-neutron system coupled to a ^{6}He core, one may decompose the total energy-weighted sum S_{tot}^{E1} for the electric dipole as[43, 44]

$$S_{tot}^{E1} = S_{^6\mathrm{He}}^{E1} + S_{2\mathrm{n}}^{E1} + S_{^6\mathrm{He}-2\mathrm{n}}^{E1} \tag{4.4}$$

where the $S_{^6\mathrm{He}}^{E1}$, $S_{2\mathrm{n}}^{E1}$ and $S_{^6\mathrm{He}-2\mathrm{n}}^{E1}$ refer to the sum rule for the core, the di-neutron and the relative motion between the two clusters. Assuming the individual clusters are not

Quantities	$\sum_f (E_f - E_i) B(E1; i \to f)$ $(e^2 fm^2 MeV)$
S_{exp}^{E1} ($E_d \leq 3$ MeV)	0.078 ± 0.062
S_{sim}^{E1} ($E_d \leq 3$ MeV)	0.082
S_{sim}^{E1}	0.11
S_{TRK}^{E1}	22
$S_{^6He-2n}^{E1}$	2.5

Table 4.1: A summary of the energy-weighted sum. The experimental value S_{exp} was extracted from the Pb target. The value S_{sim}^{E1} was obtained by integrating the dipole strength function deduced by the Monte Carlo simulation. The S_{TRK}^{E1} and the $S_{^6He-2n}^{E1}$ are calculated with the Thomas-Reiche-Kuhn(TRK) sum rule and the cluster sum rule, respectively.

excited, the total sum for the electric dipole is attributed to that of the relative motion of the two clusters. Using Eq. 4.3, the sum rule for the relative motion $S_{^6He-2n}^{E1}$ can be evaluated as

$$S_{^6He-2n}^{E1} = \frac{9}{4\pi} \frac{N_{2n} Z_{^6He}^2}{A A_{^6He}} \frac{\hbar^2}{2M} e^2 \qquad (4.5)$$

The calculated sum is also listed in the table and is 3.1 ± 2.5 % of the experimental sum S_{exp}^{E1} for $E_d \leq 3$ MeV. Since the calculated sum rule gives an upper limit of the $E1$ transition, the measured $E1$ strength is found to have a significant percentage of the total that is possible.

4.3 $E1$ continuum state

For some halo nuclei, it is not always true that the level structure is described with the standard shell model calculation. For instance, the spin-parity of the ^{11}Be ground state is found to be J^{π}=1/2$^+$, whereas the standard shell model suggests a J^{π}=1/2$^-$ assignment. This parity inversion problem was first suggested by I.Talmi *et al.*[45]. Furthermore, several theoretical calculations predict the parity inversion of the halo nuclei in the p-shell[14, 15, 46, 47, 48]. For He-isotopes, the ground state and the first excited state of ^{9}He are considered to be J^{π}=1/2$^-$ and 1/2$^+$, respectively. In addition, the models predict the excitation energy E_x ~1.5 MeV, indicating a weak sp-splitting in ^{9}He[15, 47, 48].

As discussed previously, we have found that the broad decay energy distribution for the Pb target is attributed to the $E1$ continuum excitation. Since the spin-parity of the ^{8}He ground state is J^{π}=0$^+$, a possible spin-parity of the excited state via $E1$ excitation is J^{π}=1$^-$. Thus, the excited state needs to contain one halo-neutron in s or d orbit to get the negative parity state. In this case, the excitation energy of the continuum state is higher than that of the first excited state with configuration of $(1p_{3/2})^{-1}(1p_{1/2})^1$, as observed in the decay energy distributions for the Al and Sn targets. This is consistent with the obtained parameters E_0=2.1 MeV and Γ_0=1.0 MeV in contrast to those of the first excited state E_0=1.4 MeV and Γ_0=0.5. Moreover, recent calculations predict that the spin-parity of the second excited state in ^{8}He is J^{π}=1$^-$[14, 15]. This indicates the weak sp-splitting in ^{8}He. Thus, an enhancement of the $E1$ continuum excitation may be attributed to this effect. However, theoretical calculations need to be incorporated into any further analysis.

4.4   Contribution of the $E2$ excitation

In order to evaluate contribution of the $E2$ strength to the first excited state of ^{8}He, the strength was estimated in terms of the Weisskopf unit B_W. For the electromagnetic transition for a multipole λ, $B_W(E\lambda)$ is expressed as

$$B_W(E\lambda) = \frac{(1.2)^{2\lambda}}{4\pi}\left(\frac{3}{\lambda+3}\right)^2 A^{2\lambda/3} e^2 (\text{fm})^{2\lambda} \tag{4.6}$$

The calculated value of the unit for $\lambda=2$ is listed in Table 4.2.

On the other hand, an experimental value of the $E2$ strength can be deduced from the decay energy distribution for the Pb target. As all the strength is assumed to come from the $E2$ excitation, this value gives an upper limit for the experimental $E2$ strength. The $E2$ strength function $dB(E2)/dE_x$ is related to the Coulomb dissociation cross section $d\sigma_c/dE_x$ by

$$\frac{dB(E2)}{dE_x} = \frac{75}{4}\left(\frac{\hbar c}{\pi}\right)^3 \frac{1}{n_{E2}(E_x)}\frac{1}{E_x^2}\frac{d\sigma_c}{dE_x} \tag{4.7}$$

With this relation, the upper limit of the $E2$ strength $B_{upper}(E2)$ is obtained and results are listed in Table.4.2. Since most of the $E2$ strength is exhausted up to $E_d \leq 2$ as shown by the dashed or the dot-dashed curves in Fig. 3.16, $B_{upper}(E2)$ was obtained by integrating up to $E_d \leq 2$. As shown in the table, only a small amount of the experimental strength found to be attributed to the Weisskopf units. Therefore, it may be concluded that most of the strength is attributed to the $E1$ strength as discussed in section 3.4.2.

According to the cluster model, a maximum of the $B(E1)/dE$ strength function is located at $E_d = (3/5)S$ from Eq. 4.1, where S is the neutron separation energy. Thus,

	values ($e^2\text{fm}^4$)
$B_W(E2;0{\to}2)$	6.0
$B_{upper}(E2)(E_d \leq 2)$	18 ± 10

Table 4.2: Calculated Weisskopf unit $B_W(E2;0{\to}2)$ and an upper limit of the $E2$ strength $B_{upper}(E2)$ determined by the experimental decay energy distribution for the Pb target assuming all the strength at $E_d \leq 2$ is attributed to the $E2$ excitation.

the decay energy distribution broadens as the neutron separation energy increases. If ^{8}He rather has the ^{4}He+4n structure, the strength at high decay energy may be attributed to this structure. For further analysis, theoretical calculations need to be incorporated.

Chapter 5

Summary and conclusion

We have performed kinematically complete measurements of the dissociation of 24 MeV/A ^{8}He into ^{6}He and two neutrons at the NSCL in the Michigan State University. The kinematically complete measurements allow us to provide crucial information on the reaction mechanism and on the presence of the $E1$ continuum excitation in the ^{8}He dissociation.

First of all, we have confirmed the sequential decay property in the ^{8}He dissociation. A clue to the property was found in the analysis of the 2n-removal cross sections of ^{8}He. The obtained cross sections from the inclusive (^{6}He+n+X) and the exclusive (^{6}He+2n) data sets were found to differ by a factor of about two. This discrepancy can be understood with the assumption that the dominant dissociation of ^{8}He into ^{6}He and two neutrons is a one-neutron removal process, $i.e.$, the sequential decay via the intermediate state of ^{7}He. With the cross sections, the reaction channel of the process is estimated to be approximately 60 % of the total for the Al target. For the Sn and the Pb targets, approximately 40 % of the reaction channel is required to explain the cross sections.

To verify the assumption of the sequential decay mechanism, relative energy distributions between ^{6}He and neutron are reconstructed. An observed peak at $E_{6-n}\sim$0.4 MeV in the distribution for the Al target is consistent with the ground state of ^{7}He. To take account of the acceptance and the resolution of the detector system, a Monte Carlo simulation assuming the sequential decay mechanism was performed. The relative energy distributions were well reproduced by the simulation.

Subsequent evidence of the sequential decay is found in neutron momentum distribu-

tions extracted from the ^{6}He+n+X coincidence data. The distributions were compared with those calculated with the Monte Carlo simulation used previously and were found to be reproduced well. Moreover, the distributions were calculated according to the COSMA wave function. By considering the FSI of the ^{7}He resonant state, the measured distributions were also described well with the calculation. Consequently, two independent model calculations assuming the sequential decay mechanism are found to reproduce the momentum distribution well. We therefore conclude that the dominant reaction mechanism, in particular for lighter targets, is attributed to the sequential decay process via the ^{7}He resonance.

The momentum distributions of ^{6}He and neutrons were reconstructed in the rest frame of ^{8}He. Furthermore, the distributions were fitted with the gaussian distributions and the width parameters of the function were determined. As a result, it was found that the parameters extracted from the ^{6}He+n+X and the ^{6}He+2n data agree with each other. In addition, the parameters are consistent with those of recent inclusive measurements.

By measuring momenta of all decay products from the dissociation of ^{8}He in coincidence, the decay energy of the ^{8}He can be determined. An observed peak on the decay energy distributions for the Al and the Sn targets are consistent with the known first excited state of ^{8}He with $J^\pi=2^+$. On the other hand, the distribution for the Pb target has a rather broad structure. To describe the broad structure, Monte Carlo simulations assuming the sequential and the direct decay via the first excited state were performed. The broad distribution was not reproduced with these simulations. In several measurements of Coulomb dissociation of halo nuclei, it is known that the $E1$ strength is much larger than the $E2$ strength. Since it is not feasible to separate the contribution of the $E2$ strength in present analysis, we have estimated the $E1$ strength by assuming that all of the strength is attributed to that of the $E1$ excitation as a first order approximation. By assuming that the $E1$ photonuclear cross section σ_{E1} is parameterized with the Breit-Wigner function, the measured decay energy distribution can be well reproduced. The good fit to the measured distribution yields the parameters of the function E_0=2.1

MeV and Γ_0=1.0 MeV. With these parameters, we have deduced, for the first time, the true decay energy distribution $d\sigma_c/dE_d$, the photonuclear cross section σ_{E1} and the dipole strength function $dB(E1)/dE_d$. Furthermore, absolute values of the calculated quantities are roughly comparable with those calculated with the di-neutron cluster model. This tendency has also been reported for ^{11}Li.

In the present analysis, the nuclear structure and the reaction mechanism of ^{8}He are discussed by Coulomb dissociation of ^{8}He into ^{6}He+2n. To further clarify ^{4}He+4n structure in ^{8}He, a novel experimental method will be needed.

Appendix A

Calibrations of the detectors

This section describes calibrations of the detector system consisting of the Si-strip detector, the E-detectors and the *Neutron Wall Array*. First, energy calibrations for the Si-strip detectors using beam particles at several energies are described in Appendix A.1. Second, energy calibrations for the E-detectors are described in Appendix A.2. Since the light-output response of the plastic scintillator is non-linear in general, the energy calibrations have been made using various isotopes with several energies. Finally, time and position calibrations of the *Neutron Wall Array* are described in Appendix A.3.

A.1   The Si-strip detectors

Energy calibrations for the Si-strip detectors were made with ^{4}He and ^{9}Li beams at two different energies. In order to minimize energy spread of the beams, the momentum slits of the A1200 Fragment Separator were set to $\Delta p/p$=1/4 %, so the energy spread is $\Delta E/E$=1/2 %. Since the Si-strip detectors consist of 32 (horizontal) $\times$ 16 (vertical) strips, the beams were defocused to irradiate whole strips by shutting off two quadrupole magnets located at the entrance of the experimental vault. In addition to the ^{4}He and the ^{9}Li beams, other He, Li and Be isotopes were also used for the calibrations. The beam particles used in the energy calibrations are summarized in Table A.1. A representative plot of the energy deposition in the detectors versus the measured channel for a strip in the Si-strip detectors is provided in Fig. A.1(a).

Beam kind	Energies of beam (MeV/A)	Energy loss in the strip detector
α (Defocused)	20.2	4.79
α (Defocused)	25.0	4.02
^{9}Li (Defocused)	20.3	10.7
^{9}Li (Defocused)	25.0	9.04
^{6}He	25.2	3.98
^{6}He	22.6	4.34
^{8}He	23.3	4.22
^{9}Be	44.7	10.1
^{9}Be	40.1	11.5
^{6}He (Pb target)	25.2	4.31
^{8}He (Pb target)	25.2	4.21
^{9}Be (Pb target)	44.7	11.0

Table A.1: Summary of beam particles used for the calibrations of the Si-strip detectors.
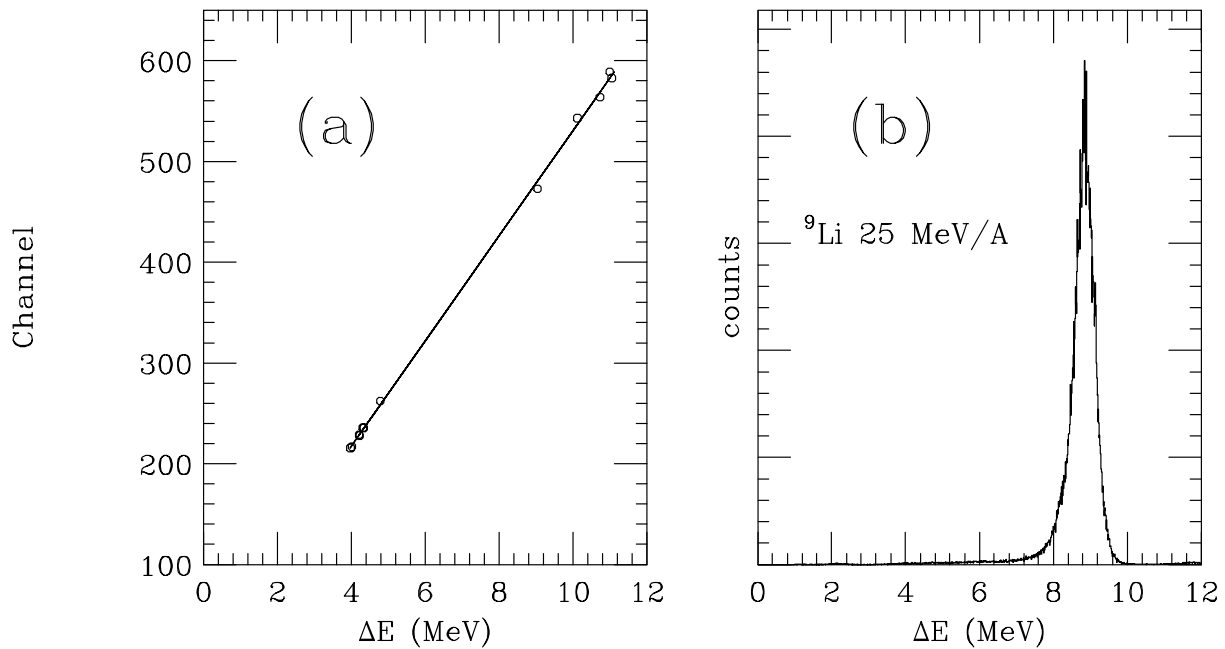
Figure A.1: (a) An example of the calibration results for one strip of the Si-strip detectors. (b) Calibrated energy loss spectrum in the Si-strip detectors for 25.0 MeV/A ^{9}Li beam.

With the calibrations, the energy resolution was found to be about 7 % FWHM. A sample energy distribution of the detector for 25 MeV/A ^{9}Li beam is provided in Fig. A.1(b).

A.2   E-detectors

As described in section 2.3.2, energies of fragments are obtained from light-output of the E-detectors consisting of the 16 plastic scintillators. Since the light-output response of the plastic scintillator is nonlinear in energy and depends on mass and charge of incident particles, considerable work has been done to understand the nonlinear response. The first successful semi-empirical model to understand the response was put forward by Birks[49]. Assuming the response to be ideally linear, Birks explained the deviations as being due to quenching of light-output. According to the model, the light-output per unit length dL/dE is expressed as

$$\frac{dL}{dE} = S\frac{\frac{dE}{dx}}{1 + k_B\frac{dE}{dx}} \tag{A.1}$$

where S is a scintillation constant and k_B is a quenching factor. Although the model reproduced experimental data rather well, a higher-order correction is required to obtain a better fit.

Recently, D. Fox *et al.* proposed an expression taking into account high energy electrons or delta rays which may escape from the primary ionization column[50]. According to this model, dL/dE may be expressed as

$$\frac{dL}{dE} = S\frac{(1 - F_s)\frac{dE}{dx}}{1 + k_B(1 - F_s)\frac{dE}{dx}} + SF_s\frac{dE}{dx} \tag{A.2}$$

F_s, the fraction of the energy carried by delta rays, is given by

$$F_s = \frac{1}{2}\left(1 - \frac{\ln(T_0/I)}{\ln((a/I)E/A)}\right) \tag{A.3}$$

where $a = 4m_e/m_0$, m_e is the electron rest mass, m_0 is the nucleon rest mass, I is the ionization potential of the scintillator ($I \simeq 0.048$ keV for plastic scintillator) and T_0 is kinetic cutoff energy of electrons. Hence, the light-output L can be obtained by integrating Eq. A.2 with respect to E as

$$L = SI \tag{A.4}$$

	$1{\leq}Z{\leq}3$		$Z{>}3$	
	T_0 (keV)	k_B	T_0 (keV)	k_B
This work	3.800	7.368	2.169	10.44
D. Fox et al.	2.85	8.31	1.13	7.18

Table A.2: Parameters T_0 and k_B for light ion ($1{\leq}Z{\leq}3$) and heavy ion ($Z{>}3$). The parameters are determined by fitting to the data.

$$I = E - k_B \int_0^{\frac{T_0 A}{a}} \frac{\frac{dE}{dx}}{1 + k_B \frac{dE}{dx}} dE - \frac{k_B}{2} \int_{\frac{T_0 A}{a}}^E \frac{(1+R)^2 \frac{dE}{dx}}{2 + k_B(1+R)\frac{dE}{dx}} dE \qquad (A.5)$$

where $R = \ln(T_0/I)/\ln((a/I)E/A)$. The free parameters S, T_0 and k_B are obtained by fitting to data. In order to obtain calibration points, the E-detectors were exposed to a series of secondary beams from the A1200 Fragment Separator. A representative $\Delta E - E$ plot is shown in Fig. A.2. After the isotopes were identified, the light-output was calculated and compared with obtained data. Fig. A.3 shows a relation between the calculated and the measured light-output, where the free parameters deduced by D. Fox et al. are used in the calculation. As shown in the figure, nonlinearity is still seen at rather large light-output. Therefore, a satisfactory fit to the data is not achieved with the parameters.

This nonlinearity was found to be attributed to the photomultiplier. Suppose the nonlinear response of the photomultiplier is expressed as a function F_{PMT}, then the light-output $L_{calculated}$ can be expressed as

$$L_{calculated} = F_{PMT}(I) \qquad (A.6)$$

and F_{PMT} can be expanded in a series in I as

$$L_{calculated} = S_1 I + S_2 I^2 + S_3 I^3 + \cdots \qquad (A.7)$$

Then, a fit was made with Eq. A.7 up to the 4th-order term for each E-detector. Separate fitting parameters were used for light ions ($1{\leq}Z{\leq}3$) and heavy ions ($Z{>}3$), respectively. The parameters k_B and T_0 were fixed as listed in Table A.2, and only the gain factors S_1, S_2, S_3 and S_4 were varied. The fitted gain factors are summarized in Table A.3. A plot

The E-detectors	S_1	S_2	S_3	S_4
E1 (1≤Z≤3)	4.3980	-9.4606×10^{-3}	4.5903×10^{-5}	-1.9382×10^{-7}
(Z>3)	4.6763	-8.6804×10^{-3}	2.7172×10^{-6}	1.6535×10^{-8}
E2 (1≤Z≤3)	4.0962	-7.8860×10^{-3}	-2.3094×10^{-5}	1.4906×10^{-7}
(Z>3)	4.1141	-5.9052×10^{-3}	-2.6795×10^{-5}	1.1333×10^{-7}
E3 (1≤Z≤3)	4.4310	-2.7150×10^{-2}	1.8797×10^{-4}	-5.7624×10^{-7}
(Z>3)	3.7329	-4.8455×10^{-3}	-2.3041×10^{-5}	7.0706×10^{-8}
E4 (1≤Z≤3)	4.5102	-2.3991×10^{-2}	1.0770×10^{-4}	-2.3877×10^{-7}
(Z>3)	4.3500	-1.7226×10^{-2}	4.5120×10^{-5}	-4.9089×10^{-8}
E5 (1≤Z≤3)	5.0324	-2.4450×10^{-2}	1.0408×10^{-4}	-2.6943×10^{-7}
(Z>3)	4.5382	-9.0560×10^{-3}	-3.9175×10^{-5}	1.6854×10^{-7}
E6 (1≤Z≤3)	6.1894	-3.7164×10^{-2}	3.3640×10^{-4}	-1.2224×10^{-6}
(Z>3)	6.3159	-1.0968×10^{-2}	-7.6307×10^{-5}	3.5692×10^{-7}
E7 (1≤Z≤3)	4.4609	-1.0865×10^{-2}		
E8 (1≤Z≤3)	4.0986	-3.5215×10^{-3}		
E9 (1≤Z≤3)	4.0379	-1.7054×10^{-2}		
E10 (1≤Z≤3)	3.4699	7.6686×10^{-3}		
E11 (1≤Z≤3)	4.6629	-1.4691×10^{-2}		

Table A.3: Gain factors S obtained by fitting with the fixed parameters T_0 and k_B listed in Table A.2. Since enough data were not available for E7 to E11 of the E-detectors, the fitting is limited for light ions (1≤Z≤3) only with the 2nd order term.

for the calculated versus the measured light-output using the factors is shown in Fig. A.4. As shown in the figure, a good agreement between the calculated and the measured light-output is seen. As a result of the calibration, the systematic error for the He-isotopes is found to be less than 1 %.

Figure A.2: A representative $\Delta E - E$ plot for secondary beams. Various isotopes with various energies resulting from interactions of the primary beam of ^{18}O on the ^{9}Be production target are seen.
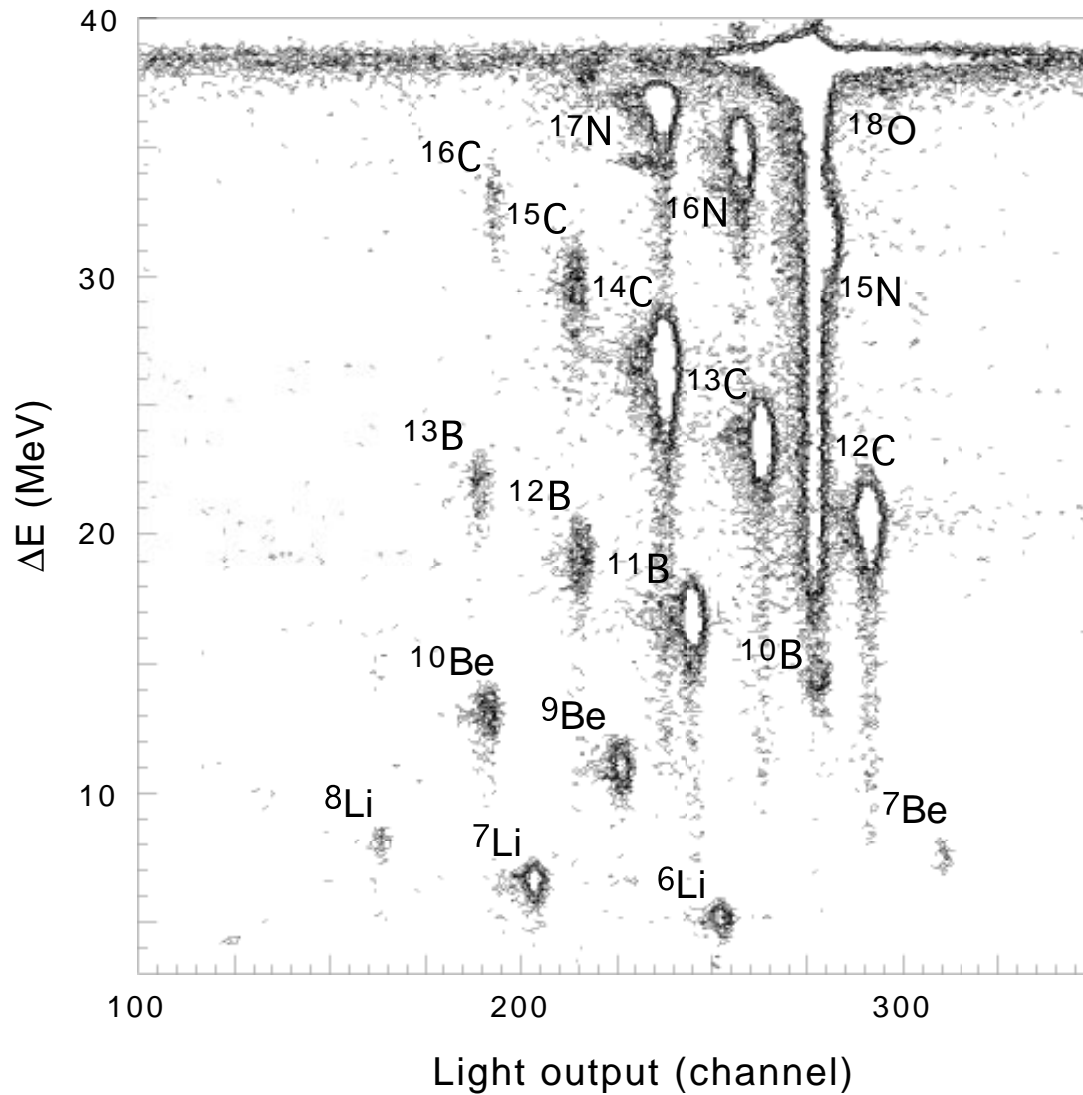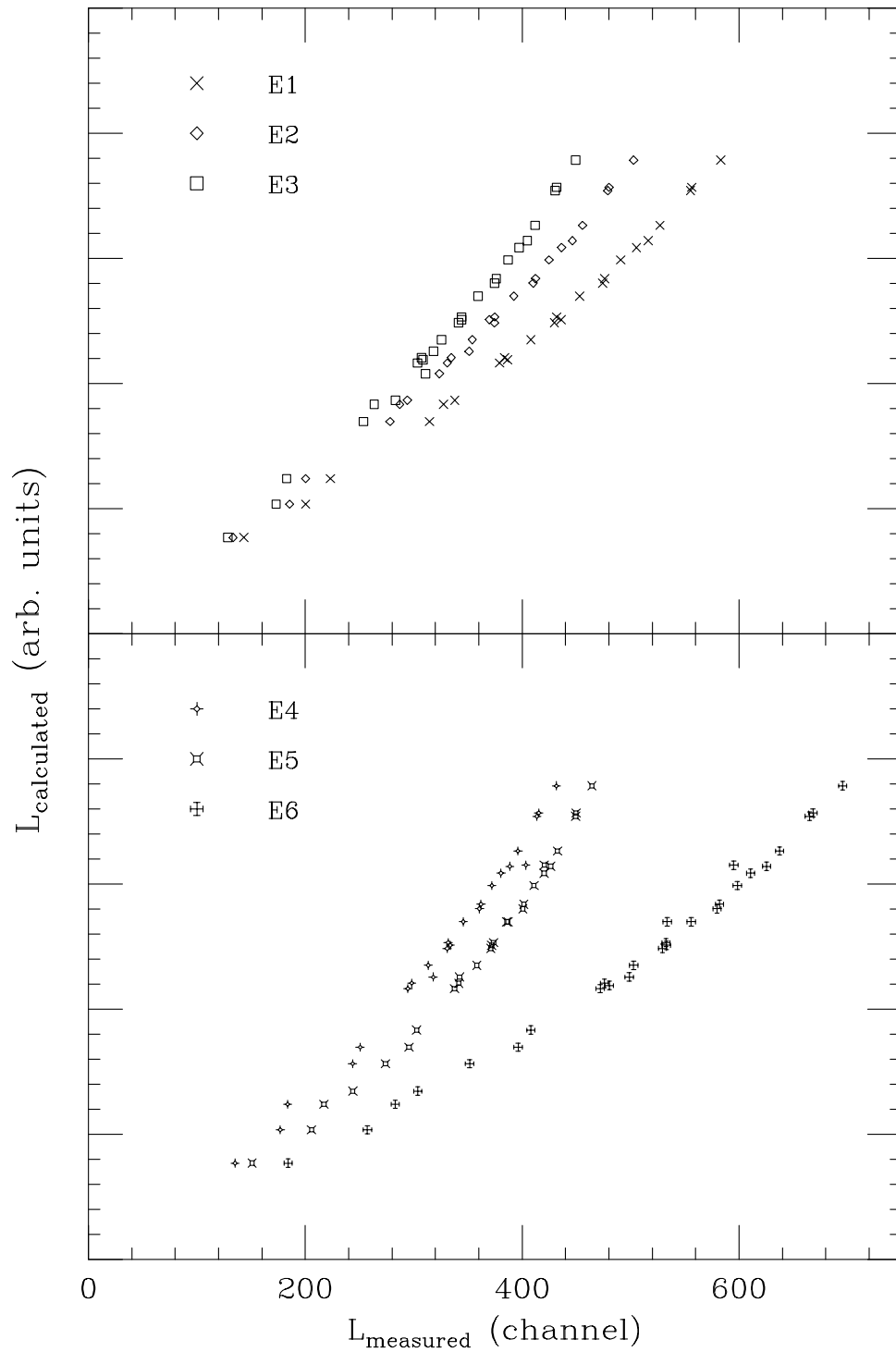
Figure A.3: Plots for calculated versus measured light-output for E1 to E6 of the E-detectors. The free parameters obtained by D. Fox *et al.* were used in the calculation.

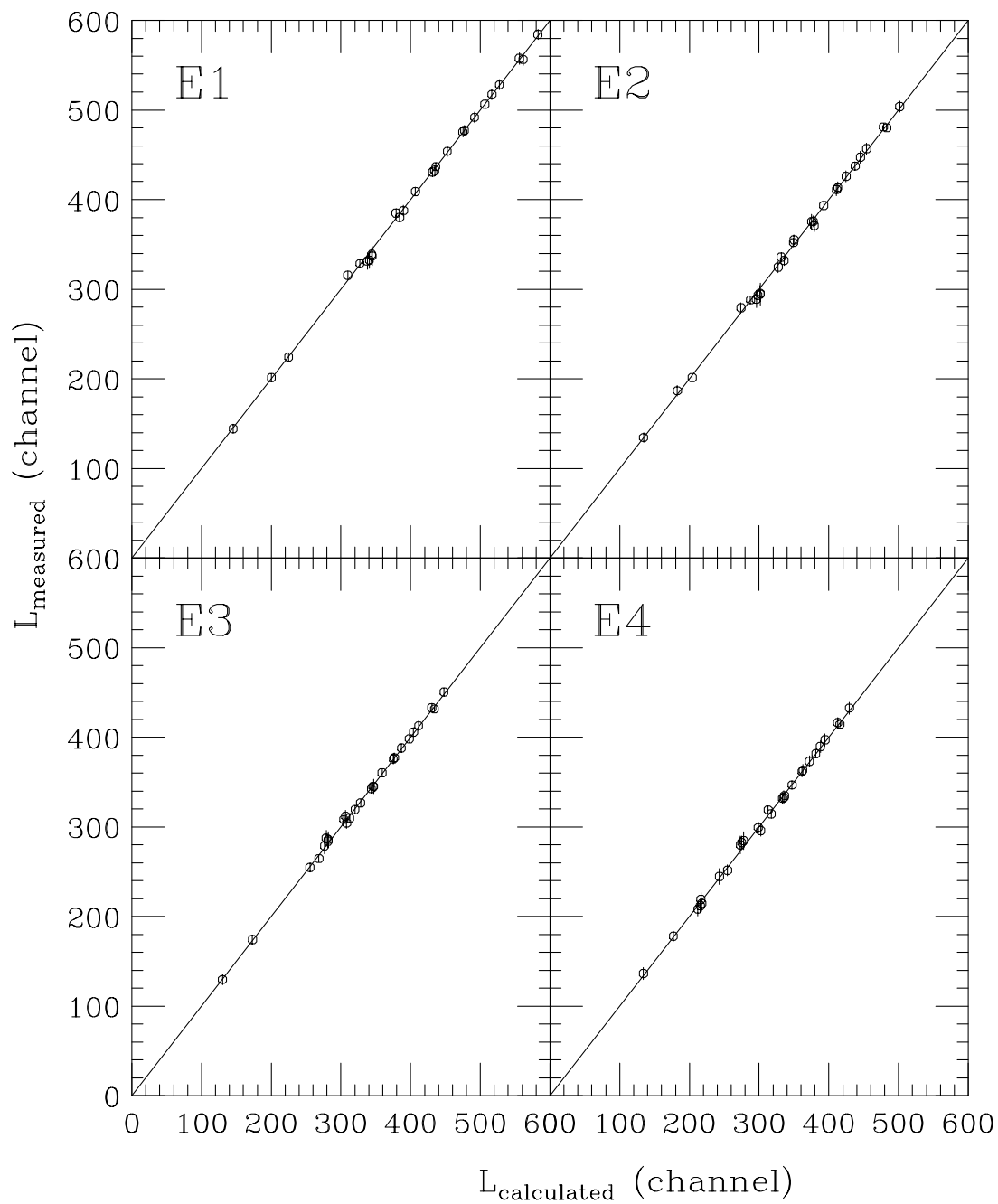Figure A.4: Plots for a calculated versus a measured light-output for E1 to E4 of the E-detectors. Data are fitted by varying only the gain factors S_1, S_2, S_3 and S_4.
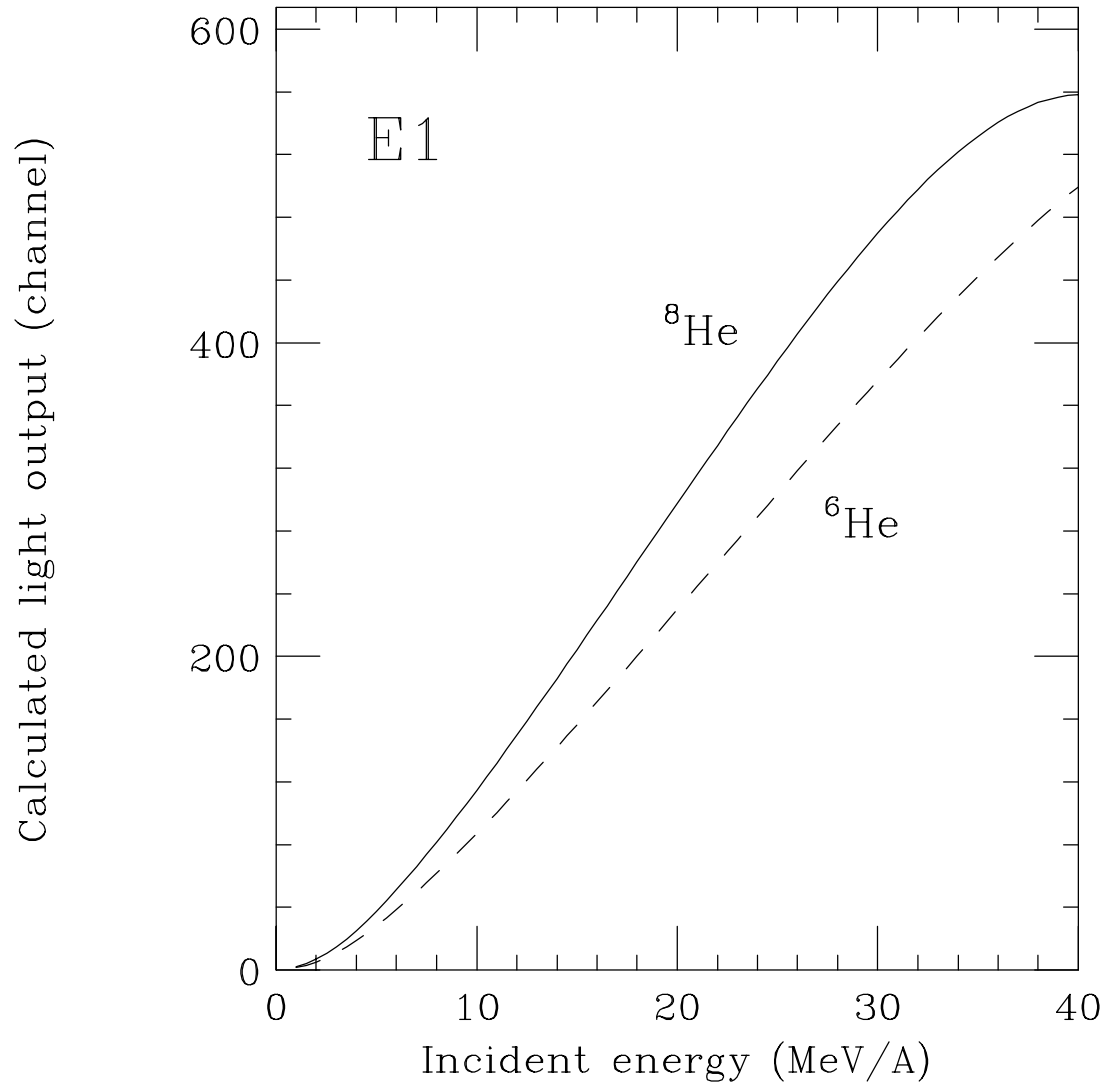
Figure A.5: Curves of calculated light-output L as a function of incident energy for ^{8}He (solid curve) and ^{6}He (dashed curve) ions. The curves are calculated for E1 of the E-detectors.

A.3 Neutron Wall Array

The calibrations of the *Neutron Wall Array* consist of two parts, *viz.*, the position and the time calibrations. As mentioned in section 2.4, the position information is obtained by the time difference of photomultipliers attached to the left and right ends of a cell. Since the time difference has an arbitrary offset, it is required to determine the offset to obtain the actual position. To determine the offset, Laser light was used. The light from the Laser source is divided into 50 thin optical fibers. One fiber is attached to exact center of each cell, so that the Laser light illuminates a small central region of the cell. Then, the light was read out by two photomultiplier attached to the two ends. The time difference of signals created by the Laser light gave the position information on the exact center of the cell. The observed position distribution has a sharp peak and a broad distribution corresponding to the Laser light and the cosmic rays, respectively. With the measured peak position for each cell, the offset can be determined. The width of the peak is better than 0.5ns (FWHM) corresponding to about 5 cm in position. The size of the broad distribution is consistent with the length of the cell.

The energy of neutrons is determined by TOF measurement. The TOF of neutrons is obtained by

$$\text{TOF} = t_{target-fragment} + t_{fragment-NW} \tag{A.8}$$

where $t_{target-fragment}$ is the TOF measured between the target position and the fragment detector and $t_{fragment-NW}$ is the TOF measured between the fragment detector and the *Neutron Wall Array*. Since the $t_{fragment-NW}$ is determined by the mean time of signals from two photomultipliers, an arbitrary time offset needs to be determined as the position calibration. To determine the time offset, coincidence measurements of γ-rays emitted from a ^{60}Co γ-ray source were made. The source was placed at the position of the target. The time offset was determined by coincidence events when γ-rays with energies of 1.33 and 1.17 MeV were detected by the E-detector and the *Neutron Wall Array*. On the other hand, the $t_{target-NW}$ is calculated from the energy and mean flight path of the

fragments. Since the trajectory of the fragment may vary only lightly, this does not affect $t_{target-fragment}$, which was confirmed with a Monte Carlo simulation.

Appendix B

Cross Talk

A detailed description of the cross talk rejection in the *Neutron Wall Array* is found in the reference[39]. Here, a brief review of the cross talk rejection is presented.

The cross talk in the *Neutron Wall Array* is categorized as two types, *viz.*, cross talk between the walls and within one wall. A schematic drawing of the two types is shown in Fig. B.1. Cross talk between the walls happens when one neutron makes a signal in one wall and another neutron in the other wall. On the other hand, cross talk within one wall happens when a neutron makes one signal in a certain cell and another signal in a neighbouring cell within one wall.

Among several processes which may produce scintillation light in the scintillator, n-p scattering is dominant in the present energy region. Hence, a simple two-body kinematics can be used to reject both types of the cross talk. By assuming the masses of a proton and a neutron are the same, $M_{\mathrm{p}} = M_{\mathrm{n}}$, the energies of the incident neutron E_{n}, the scattered neutron $E_{\mathrm{n}'}$ and the recoil proton E_{p} are related as

$$E_{\mathrm{n}'} = E_{\mathrm{n}} - E_{\mathrm{p}} \tag{B.1}$$

$$E_{\mathrm{n}'} = E_{\mathrm{n}} \cos^2 \theta \tag{B.2}$$

where θ is the scattering angle of the incident neutron. For cross talk between the walls, the measured $\cos \theta$ can be determined by a relation

$$\cos \theta_m = \frac{\mathbf{r}_{\mathrm{n}} \cdot (\mathbf{r}_{\mathrm{n}'} - \mathbf{r}_{\mathrm{n}})}{|\mathbf{r}_{\mathrm{n}}||\mathbf{r}_{\mathrm{n}'} - \mathbf{r}_{\mathrm{n}}|} \tag{B.3}$$
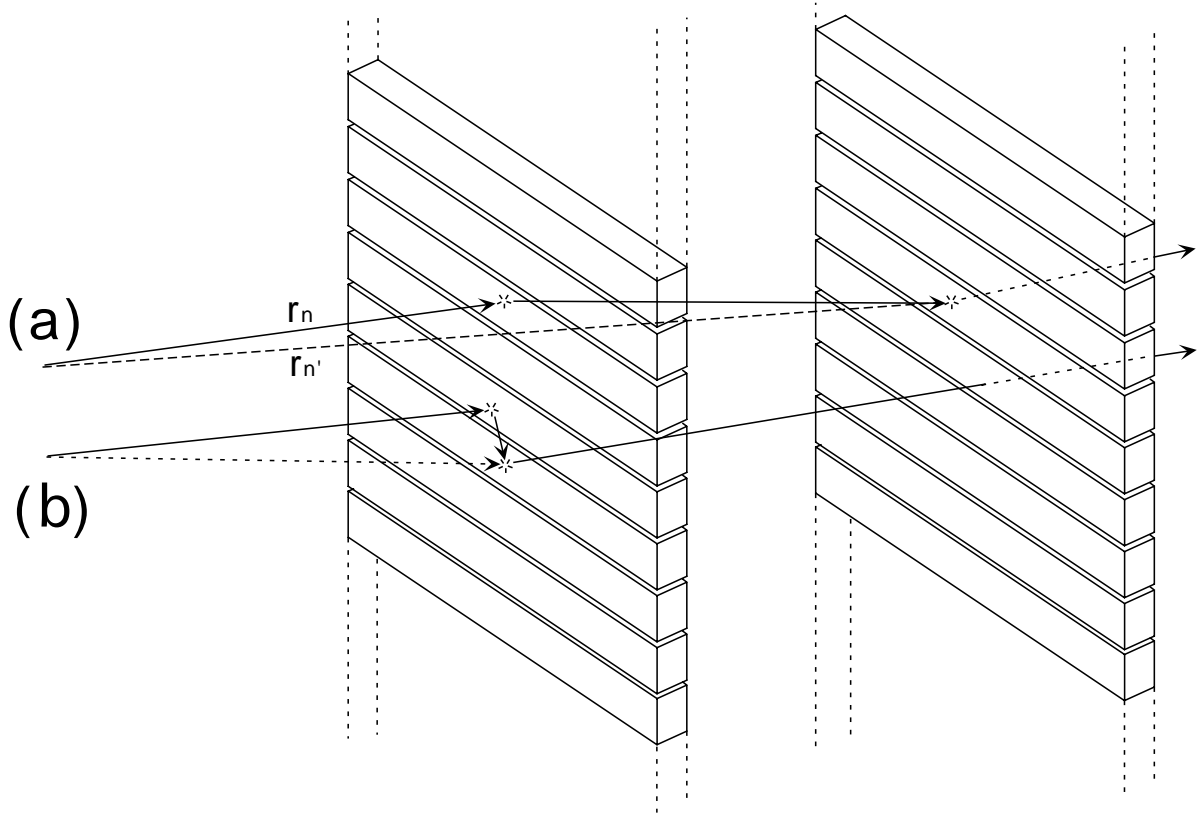
Figure B.1: A schematic drawing of the cross talk (a) between the walls and (b) within one wall.

where $\mathbf{r}$ is the position vector between the neutron source and the position where a neutron was detected in the wall. In the meantime, $E_{n'}$ can be determined by the measured TOF of the scattered neutron ΔT_m and the positions of the two n-p scatterings. With Eq. B.2, $\cos\theta$ can be calculated. For a cross talk event, the difference between the measured $\cos\theta_m$ and the calculated $\cos\theta_c$ is equal to zero. By plotting a $\cos\theta_m$-$\cos\theta_c$ distribution, the cross talk events are peaked around zero and can be rejected.

For cross talk events within one wall, it is not feasible to determine the $\cos\theta_m$ by Eq. B.3, because the position of a neutron is determined by the number of the cell fired as described in section 2.4. Instead of information on the position, the measured light-output can be used to determine the $\cos\theta_m$. By using an empirical relation between the light-output and the energy of the recoil proton E_p[51], E_p can be obtained. Then, $E_{n'}$ is

Event kind	Rejected cross talk events	Loss of true coincidence events
$\|\cos\theta_m - \cos\theta_c\| \geq 0.1$		
between the walls	72.1 %	6.7 %
within one wall	40.3 %	9.3 %
total	55.7 %	7.9 %
$\|\cos\theta_m - \cos\theta_c\| \geq 0.2$		
between the walls	86.4 %	13.1 %
within one wall	55.2 %	17.6 %
total	70.3 %	17.6 %

Table B.1: Summary of rejected cross talk events and loss of true coincidence events with selecting the events on $\|\cos\theta_m - \cos\theta_c\| \geq 0.1$ and $\|\cos\theta_m - \cos\theta_c\| \geq 0.2$.

calculated by E_{p} and Eq. B.1. Consequently, the $\cos\theta_m$ is determined with the relation Eq. B.1.

To estimate the cross talk contribution, a Monte Carlo simulation was performed. The simulation is identical to that described in section 3.4.2. Calculated $\cos\theta_m$-$\cos\theta_c$ distributions are shown in Fig. B.2. Solid histograms show all events, *i.e.*, the true 2n-coincidence events and the cross talk events, and dashed histograms show only cross talk events. Upper, middle and lower figure show events between the walls, events within one wall and total events. As seen in the figure, the cross talk events make a prominent peak at $(\cos\theta_m - \cos\theta_c) \sim 0$, where the true coincidence events make a broad distribution.

As mentioned in section 3.4, the cross talk rejections are applied for all distributions in the section. To reject the cross talk event, only events on $\|\cos\theta_m - \cos\theta_c\| \geq 0.1$ are selected. According to the simulation, it was found that 55.7 % of the cross talk events can be rejected, while 7.9 % of the true coincidence events are lost with the selection as summarized in Table B.1. By selecting events on $\|\cos\theta_m - \cos\theta_c\| \geq 0.2$, 70.3 % of the cross talk events can be rejected.
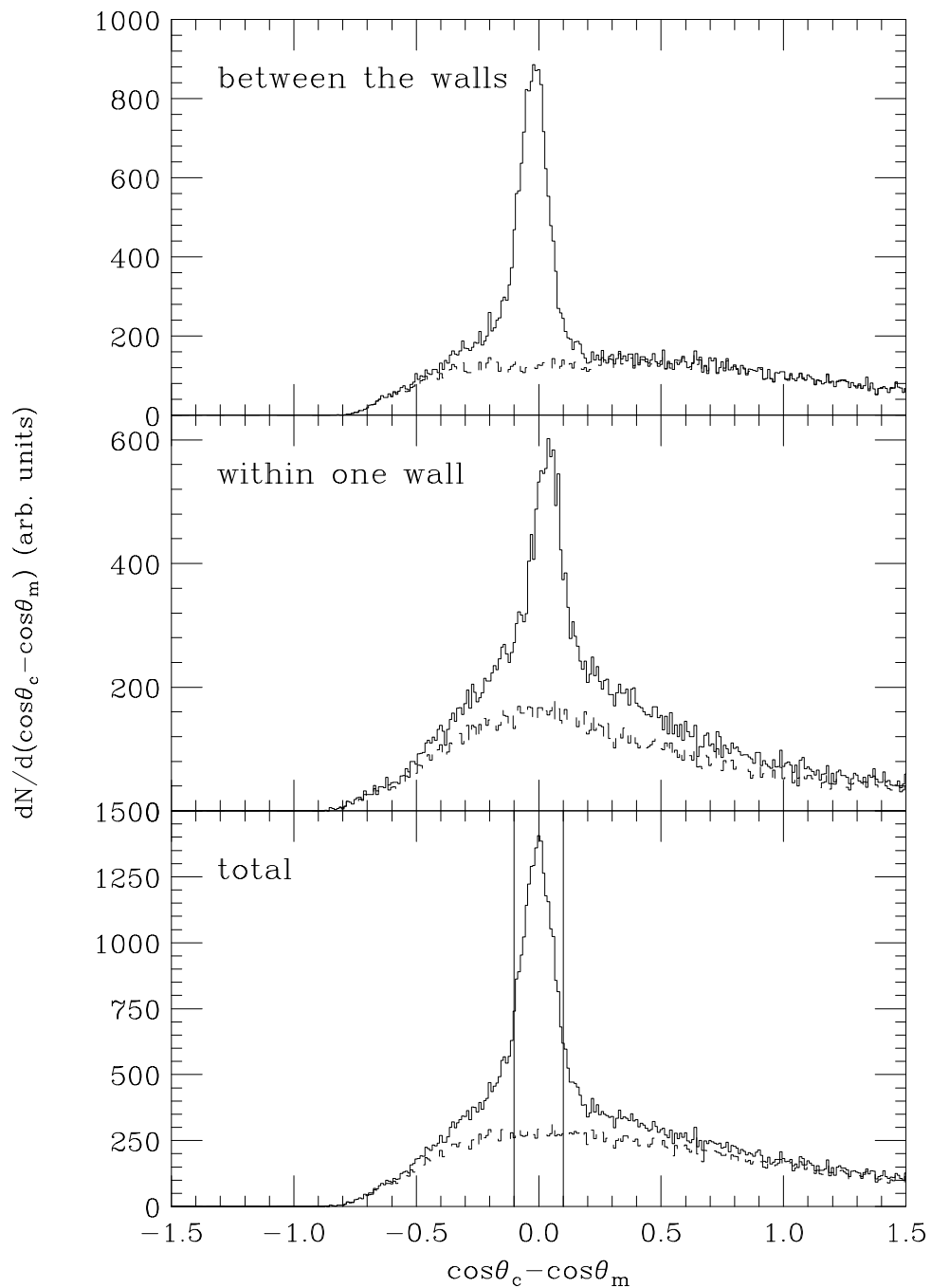
Figure B.2: Results of a Monte Carlo simulation. Solid histograms show $(\cos\theta_m - \cos\theta_c)$ distributions for all events, *i.e.*, the true 2n-coincidence events and the cross talk events. Dashed histograms show only the true coincidence events. Upper, middle and lower figures show events between the walls, events within one wall and total events.

Acknowledgements

First of all, I would like to express my sincere gratitude to my advisor, Professor Kazuo Ieki for his support, patience, suggestions and encouragement throughout my entire period as a undergraduate and a graduate student. Without his help, I might not have been able to complete my thesis. I also would like to thank him for giving me great opportunities to work at the NSCL at MSU since the summer of 1994 and also for teaching me how physicists are.

I am particularly grateful to Professor Aaron Galonsky all of his support, advice, patience and kindness throughout my work. I also would like to thank him for his advice on the nuclear physics.

I would like to thank the entire staff of the NSCL. I am grateful to Jing Wang for his help, discussion and friendship. I would like to thank Jon Kruse for valuable discussions and suggestions. Many thanks are due to Philip Zecher, Eric Tryggestad and Ryan Stevens for their help. I also would like to thank Jon Yurkon, Denis Swan and Jim Vincent for their technical assistance. I would like to thank Ron Fox for his help on the data acquisition. Thanks are due to Raman Anantaraman for his help.

I would like to express my gratitude to Ákos Horváth for his help, kindness and friendship. I would like to thank Dr. Zoltan Seres for the electronics setup of the *Neutron Wall Array*. Thanks are due to Professor Ádam Kiss for his help during the experiment. I would like to thank Professor Ferenc Deák for online/offline analysis.

I would like to thank Professor Hugo Schelin for his help and support during the experiment. Thanks are due to Professor Robert Warner for his estimation of the Coulomb/nuclear dissociation and help during the experiment. Many thanks are due to Professor Jim Ko-

lata and Dr. J.von. Schwarzenberg for their advice on the experiment and support.

I also would like to thank the entire staff of the Nuclear and Radiation Laboratory in the Rikkyo University. Particularly, I wish to acknowledge valuable discussion and suggestion with Professor Tohru Motobayashi and Professor Susumu Shimoura. I would like to thank Yoshiaki Ando for his help during the preparations of the experiment. Thanks are due to Hiroyuki Murakami for his support and help on electronics. Many thanks are due to Teiji Nishio, Yoshiyuki Yanagisawa, Toshiyuki Minemura, Satoshi Takeuchi, Goichi Motoyoshi, Yoshihide Higurashi and Hiroshi Kobayashi for their support and friendship.

I would like to thank Professor Yasuyuki Suzuki for his advice on a theoretical calculation. Also, support of the Research Fellowships of the Japan Society for the Promotion of Science for Young Scientists is gratefully acknowledged. Finally, I am grateful to my parents for their support of all kinds.

Bibliography

[1] I. Tanihata, H. Hamagaki, O. Hashimoto, Y. Shida, K. Sugimoto, O. Yamakawa, T. Kobayashi and N. Takahashi, Phys. Rev. Lett. **55**, 2676 (1985)

[2] I. Tanihata, D. Hirata, T. Kobayashi, S. Shimoura, K. Sugimoto and H. Toki, Phys. Lett. B **289**, 261 (1992)

[3] T. Kobayashi, O. Yamakawa, K. Omata, K. Sugimoto, T. Shimoda, N. Takahashi and I. Tanihata, Phys. Rev. Lett. **60**, 2599 (1988)

[4] A.S. Goldhaber, Phys. Lett. B **53**, 306 (1974)

[5] E. Arnold, J. Bonn, A. Klein, R. Neugart, M. Neuroth, E.W. Otten, P. Lievens, H. Reich, W. Widdra and ISOLDE Collaboration, Phys. Lett. B **281**, 16 (1992)

[6] R. Anne, S.E. Arnell, R. Bimbot, H. Emling, D. Guillemaud-Müller, P.G. Hansen, L. Johannsen, B. Jonson, M. Lewitowicz, S. Mattsson, A.C. Müeller, R. Neugart, G. Nyman, F. Pougheon, A. Richter, K. Riisager, M.G. Saint-Laurent, G. Schrieder, O. Sorlin and K. Wilhelmesen, Phys. Lett. B **250**, 19 (1990)

[7] I. Mukha, M.J.G. Borge, D. Guillemaud-Müeller, P. Hornshoj, F. Humbert, B. Jonson, T.E. Leth, G. Martinez Pinedo, T. Nilsson, G. Nyman, K. Riisager, G. Schrieder, M.H. Smedberg, O. Tengblad, K. Wilhelmsen, Rolander, and the ISOLDE Collaboration, Phys. Lett. B **367**, 65 (1996)

[8] K. Ieki, D. Sackett, A. Galonsky, C.A. Bertulani, J.J. Kruse, W.G. Lynch, D.J. Morrissey, N.A. Orr, H. Schulz, B.M. Sherril, A. Sustich, A. Winger, F. Deák, Á. Horváth,

Á. Kiss, Z. Seres, J.J. Kolata, R.E. Warner and D.L. Humphrey, Phys. Rev. Lett. **70**, 730 (1993)

[9] D. Sackett, K. Ieki, A. Galonsky, C.A. Bertulani, H. Esbensen, J.J. Kruse, W.G. Lynch, D.J. Morrissey, N.A. Orr, B.M. Sherril, H. Schulz, A. Sustich, A. Winger, F. Deák, Á. Horváth, Á. Kiss, Z. Seres, J.J. Kolata, R.E. Warner and D.L. Humphrey, Phys. Rev. C **48**, 118 (1993)

[10] S. Shimoura, T. Nakamura, M. Ishihara, N. Inabe, T. Kobayashi, T. Kubo, R.H. Siemssen, I. Tanihata and Y. Watanabe, Phys. Lett. B **348**, 29 (1995)

[11] M.J.G. Borge, P.G. Hansen, L. Johannsen, B. Jonson, T. Nilsson, G. Nyman, A. Richter, K. Rissager, O. Tengblad, K. Wilhelmesen and the ISOLDE Collaboration, Z. Phys. A **340**, 255 (1991)

[12] Y. Ogawa, K. Yabana and Y. Suzuki, Nucl.Phys. A **543**, 722 (1992)

[13] A.A. Korsheninnikov, K. Yoshida, D.V. Aleksandrov, N. Aoi, Y. Doki, N. Inabe, M. Fujimaki, T. Kobayashi, H. Kumagai, C.B. Moon, E.Yu. Nikolsky, M.M. Obuti, A.A. Ogloblin, A. Ozawa, S. Shimoura, T. Suzuki, I. Tanihata, Y. Watanabe and M. Yanokura, Phys. Lett. B **316**, 38 (1993)

[14] N.A.F.M. Poppelier, A.A. Wolters and P.W.M. Glaudemans, Z. Phys. A **346**, 11 (1993)

[15] N.A.F.M. Poppelier, L.D. Wood and P.W.M. Glaudemans, Phys. Lett. B **157**, 120 (1985)

[16] P. Navrátil and B.R. Barrett, Phys. Rev. C **57**, 3119 (1998)

[17] W.von Oertzen, H.G. Bohlen, B. Gebauer, M.von Lucke-Petsh, A.N. Ostrowski, Ch. Seyfert, Th. Stolla, M. Wilpert, Th. Wilpert, D.V. Alexandrov, A.A. Koresheninnikov, I. Mukha, A.A. Ogloblin, R. Kalpakchieva, Y.E. Penionzhkevich, S. Piskor, S.M. Grimes and T.N. Massey, Nucl. Phys. A **588**, 129c (1995)

[18] Th. Stolla, H.G. Bohlen, B. Gebauer, S.M. Grimes, R. Kalpakchieva, T.N. Massey, W.von Oertzen, A.N. Ostrowski, M. Wilpert and Th. Wilpert, Z. Phys. A **356**, 233 (1996)

[19] T. Nakamura, S. Shimoura, T. Kobayashi, T. Teranishi, K. Abe, N. Aoi, Y. Doki, M. Fujimaki, N. Inabe, N. Iwasa, K. Katori, T. Kubo, H. Okuno, T. Suzuki, I. Tanihata, Y. Watanabe, A. Yoshida and M.I shihara, Phys. Lett. B **331**, 296 (1994)

[20] T. Aumann, D. Aleksandrov, L. Axelsson, T. Baumann, M.J.G. Borge, L.V. Chulkov, J. Cub, W. Dostal, B. Eberlein, Th.W. Elze, H. Emling, H. Geissel, V.Z. Goldberg, M. Golovkov, A. Grünshloß, M. Hellström, K. Henchen, J. Holeczek, R. Holzmann, B. Jonson, A.A. Korshenninikov, J.V. Kratz, G. Kraus, R. Kulessa, Y. Leifels, A. Leistenschneider, T. Leth, I. Mukha, G. Münzenberg, F. Nickel, T. Nilsson, G. Nyman, B. Petersen, M. Pfützner, A. Richter, K. Riisager, C. Scheidenberger, G. Schrieder, W. Schwab, H. Simon, M. H. Smedberg, M. Steiner, J. Stroth, A. Surowiec, T. Suzuki, O. Tengblad and M.V. Zhukov, Phys. Rev. C **59**, 1252 (1999)

[21] T. Nilsson, F. Humbert, W. Schwab, M. Zinser, Th. Blaich, M.J.G. Borge, L.V. Chulkov, H. Eickhoff, Th.W. Elze, H. Emling, B. Franzke, H. Freiesleben, H. Geissel, K. Grimm, D. Guillemaud-Mueller, P.G. Hansen, R. Holzmann, H. Irnich, L. Johannsen, B. Jonson, J.G. Keller, O. Klepper, H. Klingler, J.V. Kratz, R. Kulessa, D. Lambrecht, Y. Leifels, A. Magel, M. Mohar, E.F. Moore, A.C. Muller, G. Münzenberg, P. Møller, F. Nickel, G. Nyman, A. Richter, K. Riisager, C. Scheidenberger, G. Schrieder, B.M. Sherrill, H. Simon, K. Stelzer, J. Stroth, O. Tengblad, W. Trautmann, E. Wajda and E. Zude, Nucl. Phys. A **593**, 795 (1995)

[22] T. Nilsson, F. Humbert, W. Schwab, H. Simon, M.H. Smedberg, M. Zinser, Th. Blaich, M.J.G. Borge, L.V. Chulkov, Th.W. Elze, H. Emiling, H. Geissel, K. Grimm, D. Guillemaud-Mueller, P.G. Hansen, R. Holtzmann, H. Irnich, B. Jonson, J.G. Keller, H. Klingler, A.A. Korsheninnikov, J.V. Kratz, R. Kulessa, D. Lambrecht,

Y. Leifels, A. Magel, M. Mohar, A.C. Mueller, G. Münzenberg, F. Nickel, G. Nyman, A. Richter, K. Riisager, C. Scheidenberger, G. Schrieder, B.M. Sherrill, K. Stelzer, J. Stroth, O. Tengblad, W. Trautmann, E. Wajda, M.V. Zhukov and E. Zude, Nucl. Phys. A **598**, 418 (1996)

[23] K. Ikeda, Nucl. Phys. A **538**, 355c (1992)

[24] K. Alder and A. Winther, Electromagnetic Excitation (North-Holland, Amsterdam, 1975); Coulomb excitation (Academic Press, New York 1966)

[25] B.M. Sherrill, D.J. Morrissey, J.A. Nolen and J.A. Winger, Nucl. Instr. and Meth. B **56,57**, 1106 (1991)

[26] D. Swan, J. Yukon and D.J. Morrissey, Nucl. Instr. and Meth. A **348**, 314 (1994)

[27] P.D. Zecher, A. Galonsky, J.J. Kruse, S.J. Gaff, J. Ottarson, J. Wang, F. Deák, Á. Horváth, Á. Kiss, Z. Seres, K. Ieki, Y. Iwata and H. Schelin, Nucl. Instr. and Meth. A **401**, 329 (1997)

[28] D.A. Cebra, W.K. Wilson, A. Vander Molen and G.D. Westfall, Nucl. Instr. and Meth. A **313**, 367 (1992)

[29] D.L. Olson, B.L. Berman, D.E. Greiner, H.H. Heckman, P.J. Lindstrom and H.J. Crawford, Phys. Rev. C **28**, 1602 (1983)

[30] R.E. Warner, R.A. Patty, P.M. Voyles, A. Nadasen, F.D. Becchetti, J.A. Brown, H. Esbensen, A. Galonsky, J.J. Kolata, J. Kruse, M.Y. Lee, R.M. Ronningen, P. Schwandt, J.von Schwarzenberg, B.M. Sherrill, K. Subotic, J. Wang and P.D. Zecher, Phys. Rev. C **54**, 1700 (1996)

[31] F. Ajzenberg-Selove, Nucl. Phys. A **598**, 418 (1996)

[32] R. Serber, Phys. Rev. **72**, 1008 (1947)

[33] I. Tanihata, T. Kobayashi, O. Yamakawa, S. Shimoura, K. Ekuni, K. Sugimoto, N. Takahashi, T. Shimoda and H. Sato, Phys. Lett. B **206**, 592 (1988)

[34] M.V. Zhukov and D.V. Fedorov, Sov. Jour. Nucl. Phys. **53**, 351 (1991)

[35] M.V. Zhukov, D.V. Danilin, D.V. Fedorov, J.M. Band, I.J. Tompson and J.S. Vaagen, Phys. Rep. **231**, 151 (1993)

[36] M.V. Zhukov, A.A. Korsheninnikov and M.H. Smedberg, Phys. Rev. C **50**, R1 (1994)

[37] M.V. Zhukov, A.A. Korsheninnikov, M.H. Smedberg and T. Kobayashi, Nucl. Phys. A **583**, 803 (1995)

[38] A.A. Korsheninnikov, M.V. Zhukov, M.H. Smedberg and T. Kobayashi, Eurohys. Lett. **29**, 359 (1995)

[39] J. Wang, A. Galonsky, J.J. Kruse, P.D. Zecher, F. Deák, Á. Horváth, Á. Kiss, Z. Seres, K. Ieki and Y. Iwata, Nucl. Instr. and Meth. A **397**, 380 (1997)

[40] M.V. Zhukov and B. Jonson, Nucl. Phys. A **589**, 1 (1995)

[41] C.A. Bertulani and G. Baur, Phys. Rep. **163**, 299 (1988)

[42] C.A. Bertulani, G. Baur and M.S. Hussein Nucl. Phys. A **526**, 751 (1991)

[43] Y. Alhassid, M. Gai and G.F. Bertsch, Phys. Rev. Lett. **49**, 1482 (1982)

[44] H. Sagawa and M. Honma, Phys. Lett. B **251**, 17 (1990)

[45] I. Talmi and I. Unna, Phys. Rev. Lett. **4**, 469 (1960)

[46] H. Sagawa, B.A. Brown and H. Esbensen, Phys. Lett. B **309**, 1 (1993)

[47] A.G.M. van Hees and P.W.M. Glaudemans, Z. Phys. A **314**, 323 (1983)

[48] A.G.M. van Hees and P.W.M. Glaudemans, Z. Phys. A **315**, 223 (1984)

[49] J.B. Birks, "The Theory and Practice of Scintillation Counting" (Pergamon Press, London 1964)

[50] D. Fox, D.R. Bowman, G.C. Ball, A. Galindo-Uribarri, E. Hagberg, D. Horn, L. Beaulieu and Y. Larochelle, Nucl. Instr. and Meth. A **374**, 63 (1996)

[51] V.V. Verbinsky, W.R. Burrus, T.A. Love, W. Zobel, N.W. Hill and R. Textor, Nucl. Instr. and Meth. **65**, 8 (1968)